

Forecasting of Auroral Pc5 Pulsations from Solar Wind Parameters Using Machine Learning Approach.

stephen Owino Omondi¹, Justice Allotey Pappoe¹, Sebwato Nasurudin¹, and Ayman Mohamed Mahrous²

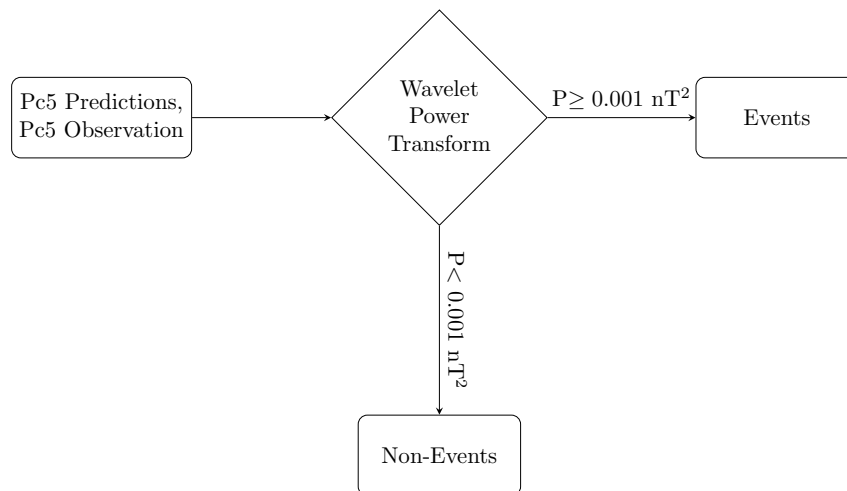
¹Egypt Japan University of Science and Technology

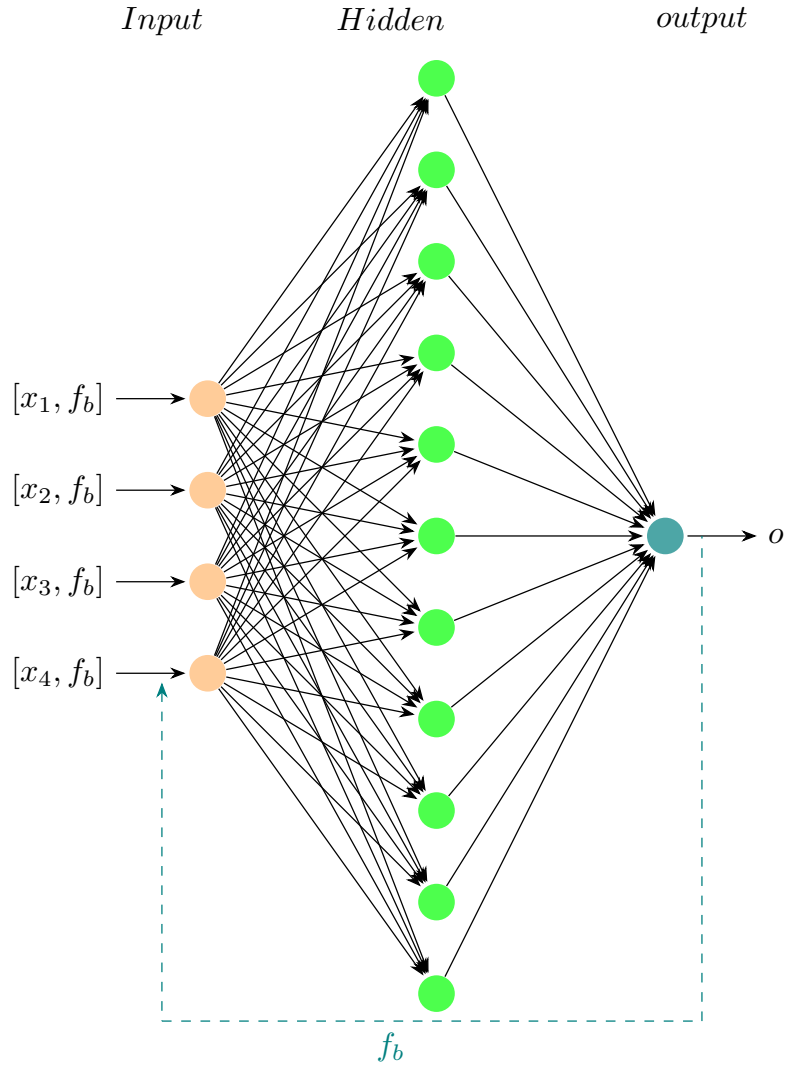
²Space Weather Monitoring Center, Helwan University, Faculty of Science

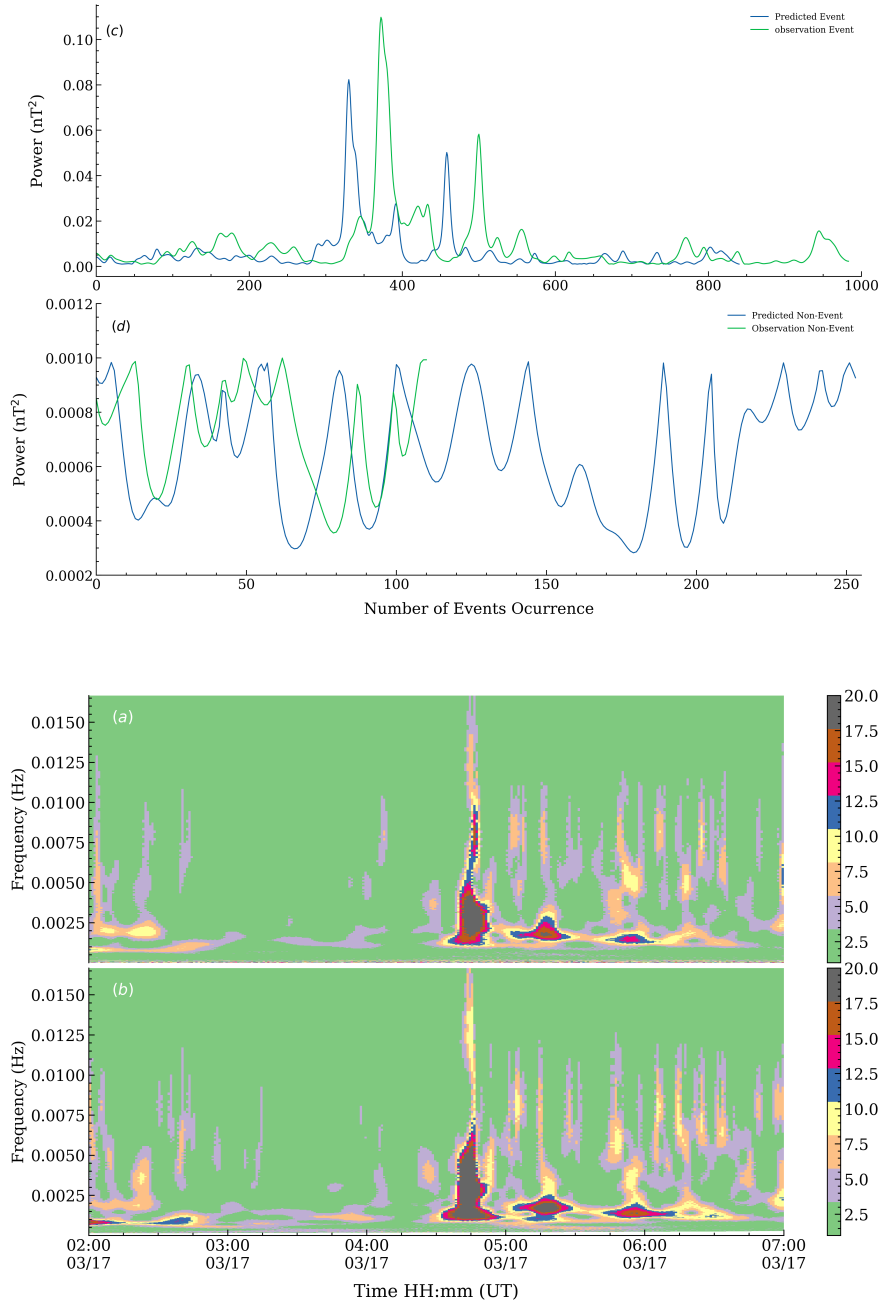
April 26, 2024

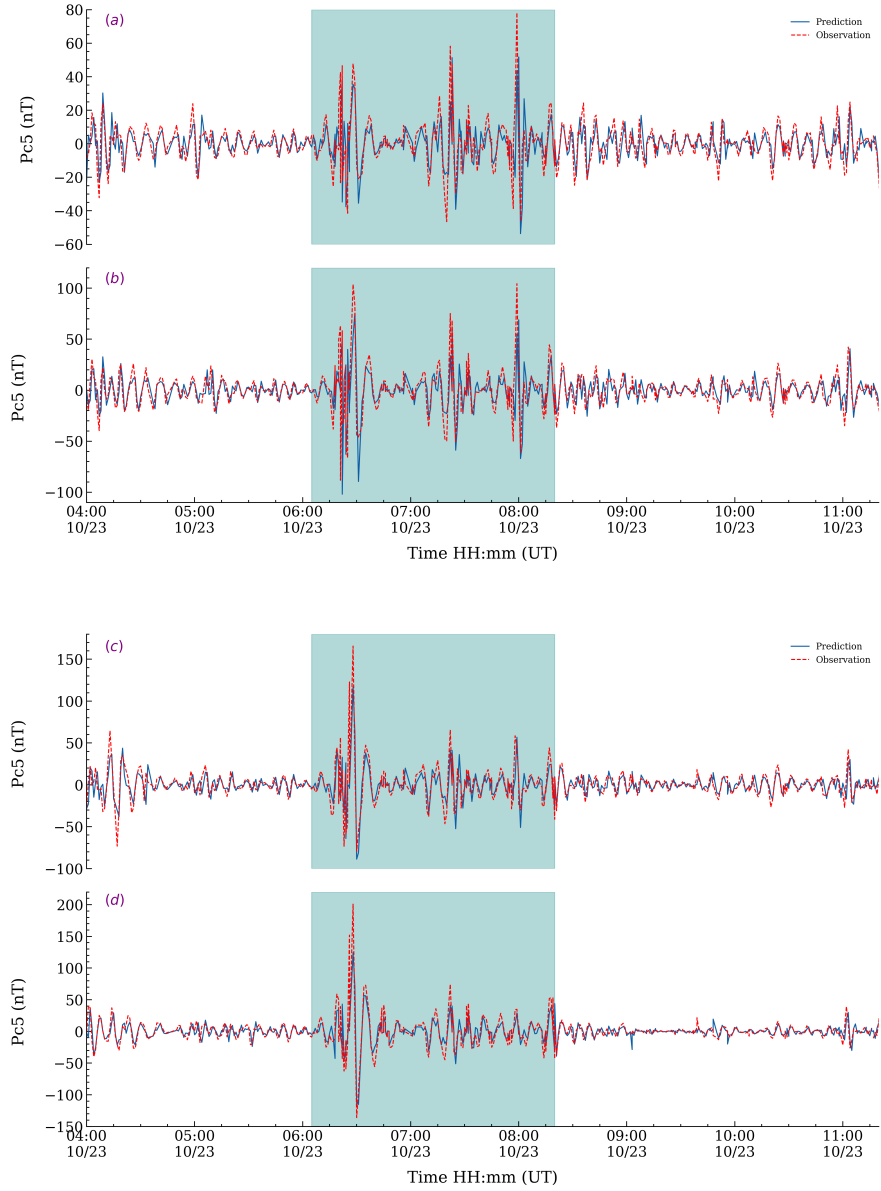
Abstract

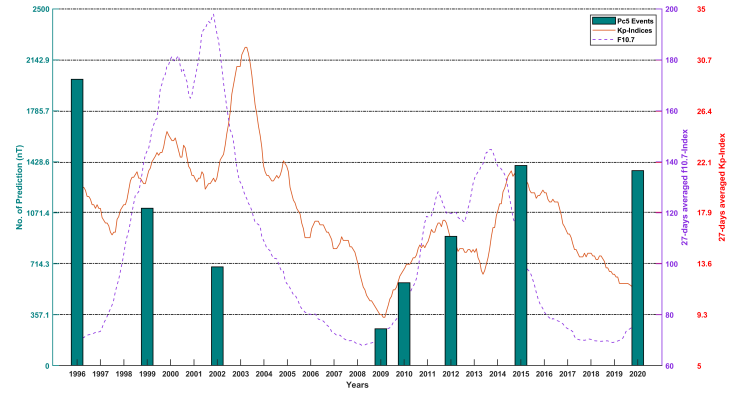
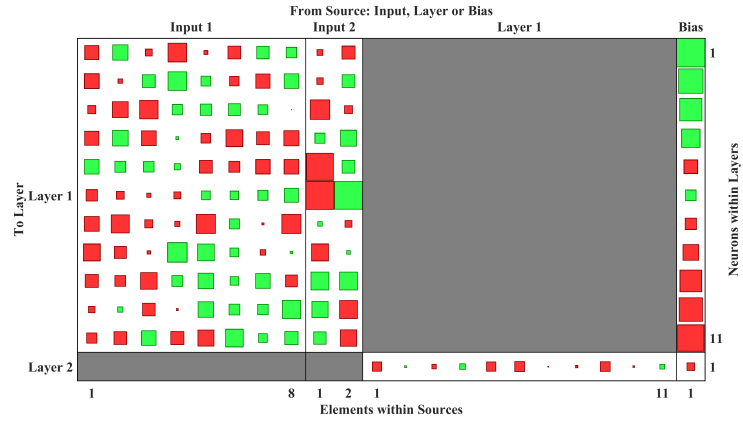
The coupling between the magnetosphere and solar wind contributes to the energy, momentum, and mass transfer between the systems. However, geomagnetic pulsations facilitate the continuation of this process in the magnetosphere and the production of discrete auroral arcs. Therefore, remote-sensing the magnetospheric conditions. Data analytics with machine learning (ML) gives insight into scalability, adaptability, and feature extraction compared to traditional empirical models. The availability of big data in the Svalbard network spanning 25years from 1996 motivated the current study. Hence, we present the forecasting of auroral Pc5 pulsations from solar wind parameters using the ML technique. In the training phase, there was a regression of 0.75 and MSE=11.90 nT². The relationship between Pc5 forecast and observations in low and high geomagnetic activity and solar activity showed good consistency with R=0.76 and MSE= 11.4 nT². For instance, the model adapted well to the St. Patrick geomagnetic storm of March 17th, 2015 despite uncertainties in the data. In addition, the model also adapted well with stunning performance in all Svalbard observatories with HOP leading with 6949 prediction events and NAL with the least. Thus, this was consistent with previous studies in terms of Pc5 pulsations latitudinal or L-shell dependence. Finally, validation with Kp and F10.7 indices presented excellent coherence between the models. Overall, The ML studied the connection between solar wind and interplanetary magnetic field properties to the ground magnetic field perturbations with good correlation results. Hence, the model will be fit for use by the magnetospheric community for space weather studies.

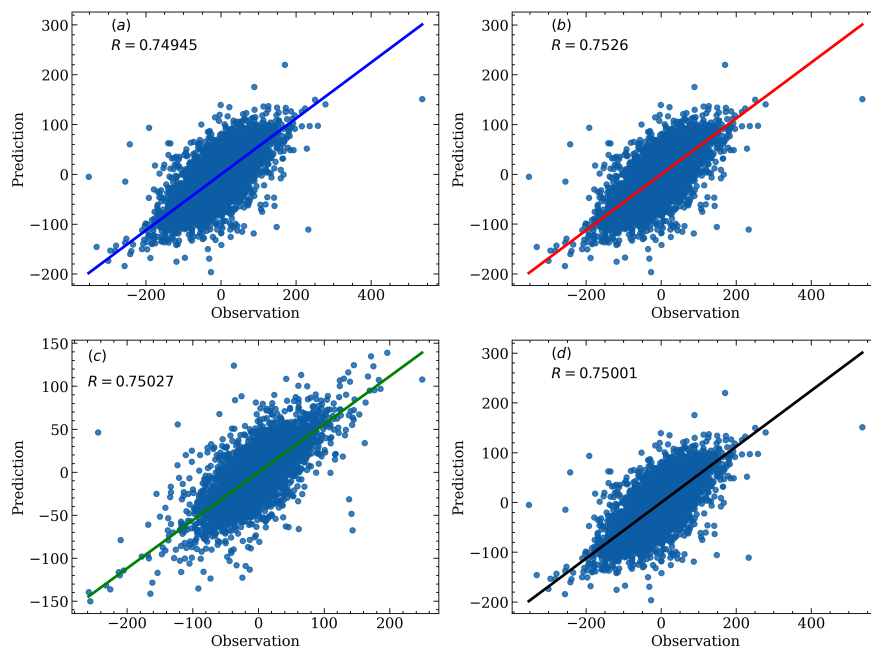
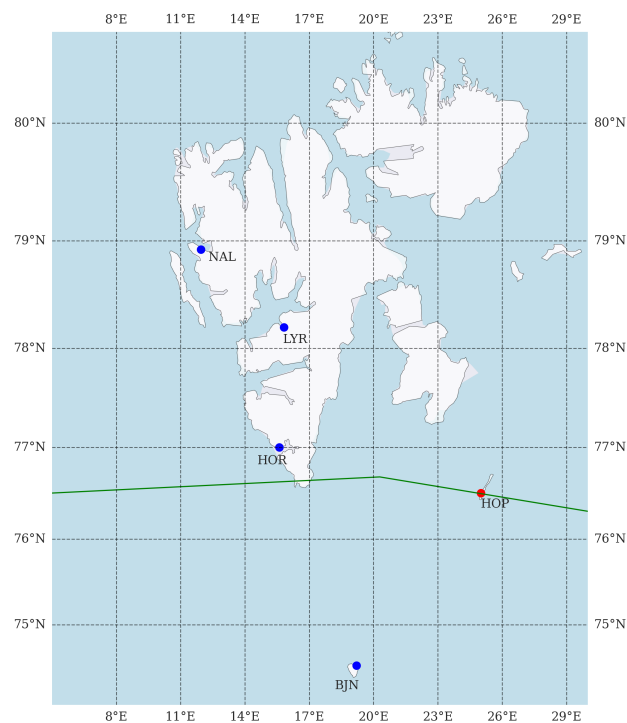


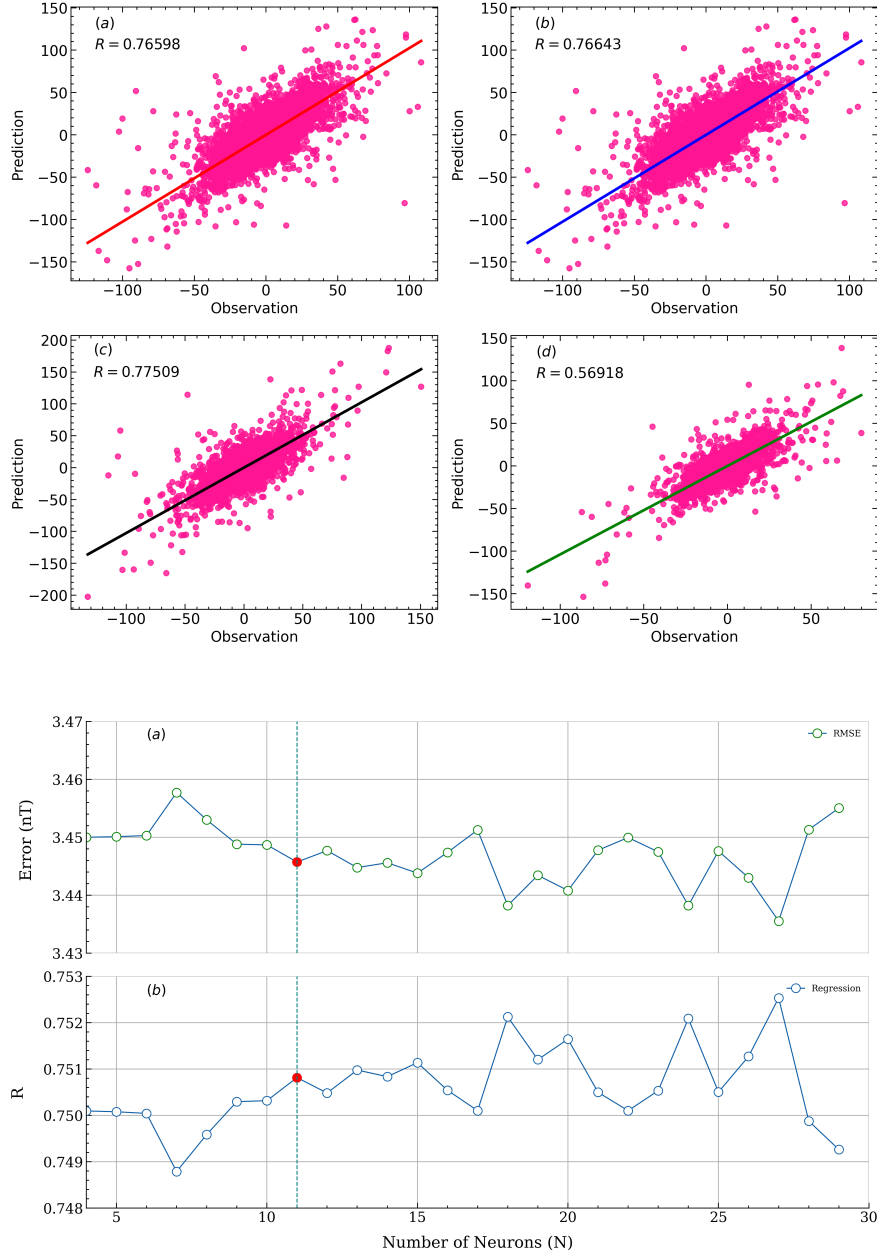


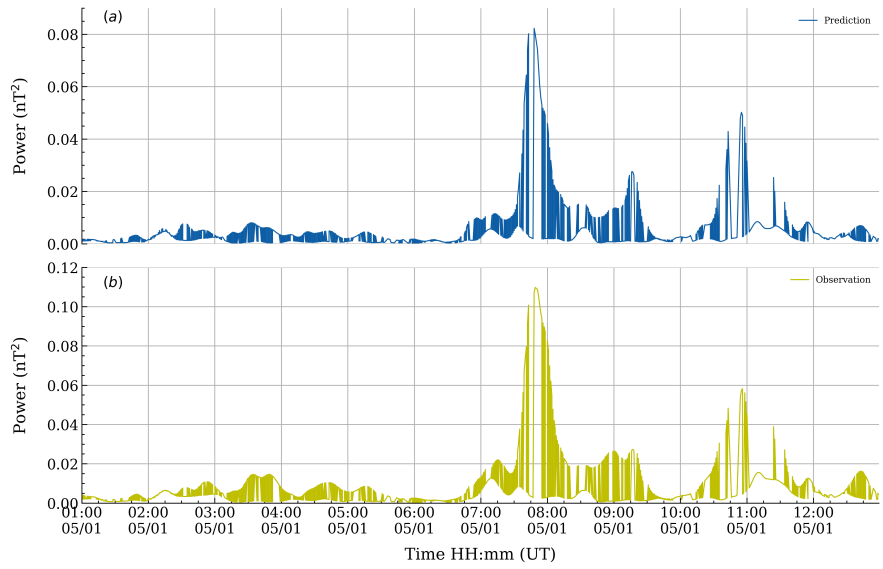
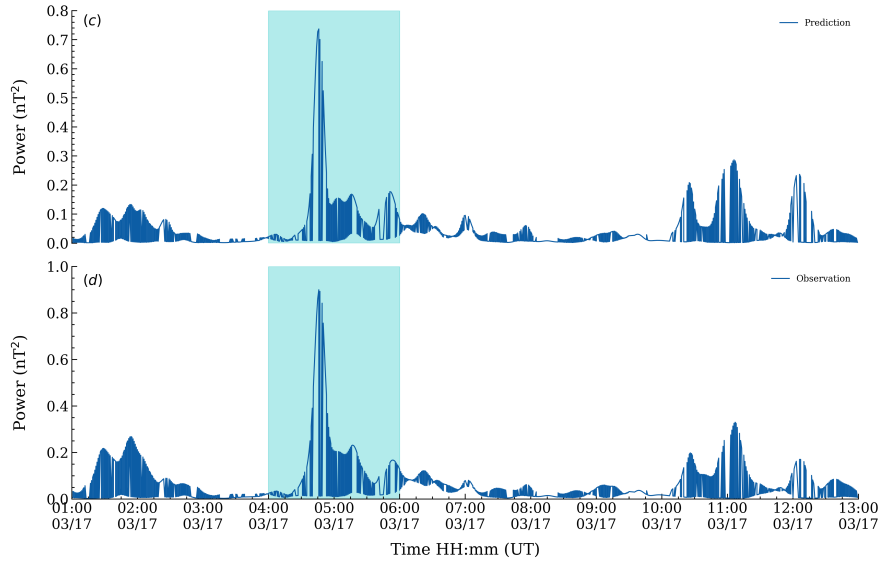


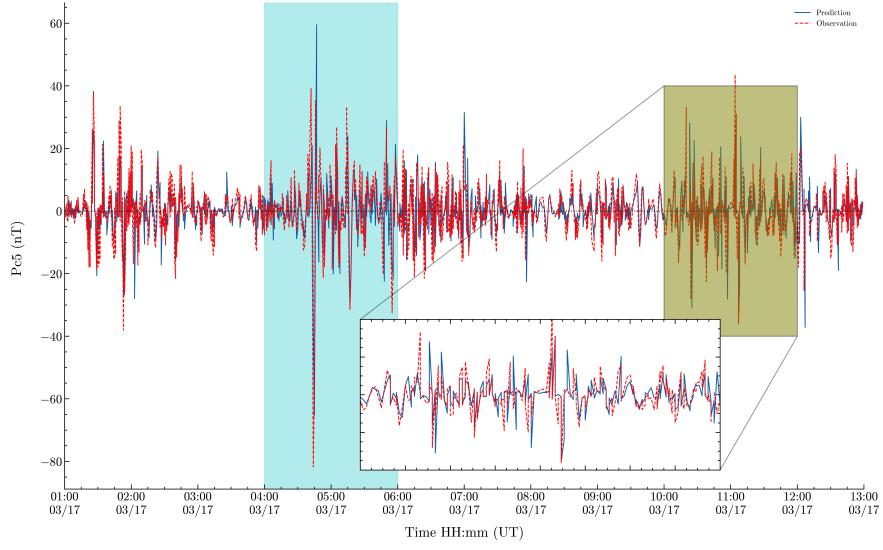












Forecasting of Auroral Pc5 Pulsations from Solar Wind Parameters Using Machine Learning Approach.

Stephen Omondi^{1,3}, Justice Allotey Pappoe¹, Sebawato Nasurudiin¹, Ayman Mahrous^{1,2}

¹Department of Space Environment, Institute of Basic and Applied Sciences, Egypt-Japan University of Science and Technology (E-JUST), New Borg El-Arab City, Alexandria 21934, Egypt

²Department of Physics, Faculty of Science, Helwan University, Helwan, Cairo, Egypt

³Jomo Kenyatta University of Agriculture and Technology, Physics department, P.O.Box 62000-00200, Nairobi, Kenya

Key Points:

- We carried out the prediction of auroral Pc5 pulsations from solar wind parameters with the NARX network.
- Wavelet analytics was used in the definition of predicted Pc5 events
- Hinton diagram was used to display the internal structure of the trained model

Corresponding author: Stephen Omondi, stephen.owino.omondi@outlook.com

Abstract

The coupling between the magnetosphere and solar wind contributes to the energy, momentum, and mass transfer between the systems. However, geomagnetic pulsations facilitate the continuation of this process in the magnetosphere and the production of discrete auroral arcs. Therefore, remote-sensing the magnetospheric conditions. Data analytics with machine learning (ML) gives insight into scalability, adaptability, and feature extraction compared to traditional empirical models. The availability of big data in the Svalbard network spanning 25 years from 1996 motivated the current study. Hence, we present the forecasting of auroral Pc5 pulsations from solar wind parameters using the ML technique. In the training phase, there was a regression of 0.75 and MSE=11.90 nT². The relationship between Pc5 forecast and observations in low and high geomagnetic activity and solar activity showed good consistency with R=0.76 and MSE= 11.4 nT². For instance, the model adapted well to the St. Patrick geomagnetic storm of March 17th, 2015 despite uncertainties in the data. In addition, the model also adapted well with stunning performance in all Svalbard observatories with HOP leading with 6949 prediction events and NAL with the least. Thus, this was consistent with previous studies in terms of Pc5 pulsations latitudinal or L-shell dependence. Finally, validation with Kp and F10.7 indices presented excellent coherence between the models. Overall, The ML studied the connection between solar wind and interplanetary magnetic field properties to the ground magnetic field perturbations with good correlation results. Hence, the model will be fit for use by the magnetospheric community for space weather studies.

1 Introduction

Geomagnetic pulsations of the frequency band (1.7-6.7) mHz are generated by magnetospheric ultra-low frequency (ULF) waves. These waves contribute to the momentum, mass, and energy transfer and in the discrete auroral arcs production (Samson et al., 1996). The characteristics of Pc5 waves, majorly determined by the length of and plasma distribution along magnetic flux tubes, give means of remote-sensing magnetospheric conditions, for example, the radial spreading of the equatorial plasma density in the inner magnetosphere (Waters et al., 1995). The field line resonance theory explains the generation of Pc5 undulations (Chen & Hasegawa, 1974; Southwood, 1974). Shear velocity in the plasma flow on the magnetopause excites the Kelvin-Helmholtz instability, and the resulting surface waves propagate and penetrate the Earth's magnetosphere as fast compressional mode waves. When the compressional waves meet the region where the local field line eigenfrequency matches the fast mode frequency, the energy of compressional waves is coupled into shear Alfvén waves by the field line resonances. Consequently, waveguide theory (Harrold & Samson, 1992) and Cavity mode theory (Kivelson et al., 1984) also explain the discrete frequency field resonances. Overall, field line resonances theory has successfully been adopted to explain numerous features of in situ and ground observation of geomagnetic pulsations (Baddeley et al., 2007).

Pc5 pulsations frequently monitored at the auroral latitudes mostly using radars and ground magnetometers (Ziesolleck & McDiarmid, 1994) are of large amplitude (reaching 100 nT). According to the study conducted by Samson et al. (1971), the sense of Pc5 pulsations polarization and their amplitude spectra exhibit marked latitude dependence. Therefore, the maximum Pc5 amplitude occurs around magnetic latitude (MLat) between 65° and 75° (Kleimenova et al., 2010). In the auroral strip, Pc5 polarization fluctuates near noon and at the latitude of maximum amplitude. Thus, the ground magnetic field perturbations are in principle the field due to the ionospheric Hall currents. These measurements show that the perturbation of the northward magnetic field component peaks near the resonant field line location and $\sim 180^\circ$ phase shift across the resonant latitude (Lee et al., 2007). The fast-mode surface waves arrive at the resonance point via the field lines, oscillating them in the transverse direction. In principle, the ground-based observation of Pc5 pulsations would show that they travel with a small azimuthal wave num-

ber westward in the morning and eastward in the afternoon. Therefore, the maximum Pc5 amplitudes and intensity always peak along 73° MLat (Pilipenko et al., 2001).

Consequently, in the auroral oval, there are two unrelated electrodynamic phenomena; Pc5 pulsations and auroral electrojets (AEJ). AEJs are part of 3-D ionospheric current systems resulting from solar wind-magnetosphere couplings. These currents also flow either westward or eastward and are latitudinally confined by the Hall current. It was noted that AEJ intensity and Pc5 power peak at the same latitude and determined by unrelated processes. The Pc5 maximum intensity and position shift in latitude remained within the strips of AEJ of about 8° wide. Rostoker and Lam (1978) proposed an explanation for this consistency, reporting these waves are the eigenmodes of a 3-dimensional terrestrial magnetosphere-ionosphere current system. Pilipenko et al. (2001) findings were similar to that of Rostoker and Lam (1978); Pc5 pulsation temporal and spatial variations in the prenoon or morning sectors are intimately related to the intensity and location of auroral electrojet currents. Implying possible modulation of Pc5 waves from the magnetic contribution of AEJs in the region. Omondi et al. (2023) piloted a study on the automatic detection of auroral Pc5 pulsations guided by wavelet technique in the region separating Pc5 pulsation from raw data. Their findings were consistent with traditional results reporting large amplitudes of detected Pc5 pulsations.

Studies of geomagnetic activities using geomagnetic indices have shown that the magnetosphere behaves as a nonlinear dynamic system (Kamide et al., 1998). Various methods based on the physical, analytical or empirical relationships between geomagnetic parameters and solar wind, artificial intelligence, and correlations have been used to forecast geomagnetic activities (Williscroft & Poole, 1996; Wu & Lundstedt, 1996; Wu et al., 1998; Weigel et al., 1999; Gholipour et al., 2004; Uwamahoro & Habarulema, 2014; Eastwood et al., 2017; Wintoft et al., 2017; Chandorkar et al., 2017). The nonlinear autoregressive with exogenous input (NARX) model has widely been used for forecasting and modeling nonlinear systems. The NARX model performs well in the recognition of nonlinear systems by selecting the high-ranked model terms from a dictionary comprising numerous candidate model terms (Billings, 2013). Given that the magnetosphere is a nonlinear process, NARX presents itself to be the most efficient method for space weather predictions. The NARX models have been successfully used in the prediction of various geomagnetic indices, for instance, the AE index (Gu et al., 2019), Kp index (Ayala Solares et al., 2016), and the Dst index (Balikhin et al., 2011; Boynton et al., 2011; Wei et al., 2004) with great performance. Cai et al. (2009) studied storms by forecasting SYMH using ACE data which yielded a good performance with RMSE of $14nT^2$ and a correlation coefficient of about 0.9. Bhaskar and Vichare (2019) extended Cai et al. (2009) studies to predict the ASYH index by use of the NARX network. In that, they used ASYH and SYMH indices during the great geomagnetic storms occurring between 1998-2015 in two solar cycles, 23 and 24. The results were astounding as the forecasting model reproduces the entire time profiles of ASYH and SYMH with small time variations of about 10-30 min within noise level tolerance.

Several studies on Pc5 pulsations have pointed out its significance to space weather monitoring. Currently, there is no report on an ANN-based forecasting model available for ground Pc5 pulsations using solar wind parameters. The ANN-based prediction of ground Pc5 pulsations will be useful in understanding the contribution of internal and external drivers in the observed asymmetries. The forecasting model can be deployed to complement the issue of data loss and integrity problems in one station based on observations in others within the same network. The current work complements Omondi et al. (2023) studies in the Svalbard network utilizing the same dataset of solar cycle 23 and 24 to perform the auroral Pc5 prediction. Therefore, the main objective of the study is to develop a ground Pc5 prediction model using a dynamic NARX simulation model in the Svalbard network trained with solar wind parameters as input and feedback from the output. The robustness of the NARX model's performance in previous studies was

120 the motivation for its selection in the current study. The current paper is organized into
 121 5 sections: Section 2 introduces time series NARX feedback neural networks, section 3
 122 describes the data and methodology, section 4 gives results and discussion, and finally
 123 conclusion.

124 2 Time Series NARX Feedback Neural Networks

125 Artificial neural networks (ANN) are computation simulations that mimic biolog-
 126 ical neural networks in the brain (Poulton, 2002). They were first suggested by McCulloch
 127 and Pitts (1943) to study non-linear systems problems. There are numerous kinds of ANNs
 128 for modeling physical systems. In particular, the most frequently used ANN for mod-
 129 eling physical time series data is the MultiLayer Perceptron (MLP) Network. Feed-forward
 130 neural networks have been more effective than MLP in modeling nonlinear time series
 131 (Omondi et al., 2023). When simulating nonlinear time series, recurrent dynamic net-
 132 works with feedback are preferred. Therefore, the suitable and powerful type of recur-
 133 rent Network for nonlinear systems (time-series) is a nonlinear autoregressive network
 134 with exogenous inputs (NARX). Normally nonlinear systems are selected the same way
 135 as linear systems by considering the right parameters. Thus, in nonlinear systems, one
 136 can reconstruct the relation of the kind

$$o[t] = g(o[t-1], o[t-2], \dots, o[t-n_o], x[t-1], x[t-2], \dots, x[t-n_x] + e[t]) \quad (1)$$

137 Equation 1 shows a time series NARX model (nonlinear ARX), where g is a nonlinear
 138 function of fixed inputs and outputs. In the event of training NARX, the data are de-
 139 fined sequentially as $\chi^j = [o[t-j], o[t-j-1], \dots, o[k-j-(n_o-1)], x[t-j], x[t-j-1], \dots, x[t-j-(n_x-1)]]^T$
 140 and $\gamma^j = o[t-j+1]$, for $j=1, \dots, M$ (Ayala Solares et al., 2016). Where χ^j defines the context outputs and inputs while the γ^j is the target data.
 141 Once the training is done and the model has learned with good results. Next, the model
 142 is ready and saved for deployment. In the event of prediction or forecasting future val-
 143 ues of $o[t]$, the previous values $o[t-1], o[t-2], \dots, o[k-n_o], x[t-1], o[t-2], \dots, x[t-n_x]$
 144 grouped in one (n_o+n_x) -dimensional input vector are passed along with external
 145 inputs, x . Therefore, in this study, the simulation model here functions as a multiple in-
 146 put single output (MISO) system for prediction. The resultant model architectural de-
 147 sign used in the current work is schematically presented in Figure 1.

149 To make steps ahead predictions by estimating $o[t]$ at time t , and re-using the $o[t]$
 150 estimates in the input vector to forecast $o[t+1]$ without using true $o[t]$, target, the NARX
 151 simulation functions as a recurrent neural network. This way the output of the network
 152 will always depend on the input attributes (Billings, 2013). In essence the $o(t+1)$ is
 153 dependent on the previous values of an independent (exogenous) input signal $x[t]$, and
 154 previous values of the output signal $o[t]$; n_o and n_x are time delays of the output and
 155 input variables, and $e(t)$ is the model error or residual between the target and forecasted
 156 values.

157 The output of the hidden layer at time t is determined by Eqn.2 (Cai et al., 2009):

$$h_j(t) = \tanh \left[\sum_{k=0}^{n_x} w_{jk} x(t-k) + \sum_{l=1}^{n_o} w_{jl} o(t-l) + a_j \right] \quad (2)$$

158 w_{jk} is the weight connection between input, $x(t-k)$ and the j^{th} hidden neurons while
 159 that between hidden and output layers, $o(t-l)$ is given by w_{jl} . a_j is the bias in the j^{th}
 160 hidden layer neuron.

161 Figure 1 shows a simple NARX simulation architectural model designed using re-
 162 sults from Figure 2. This model consists of one input layer comprising four input nodes
 163 defined by the number of input attributes $x_1 - x_4$ and feedback inputs f_b , one hidden
 164 layer composed of 11 nodes, and one output node, o , in the output layer. The feedback

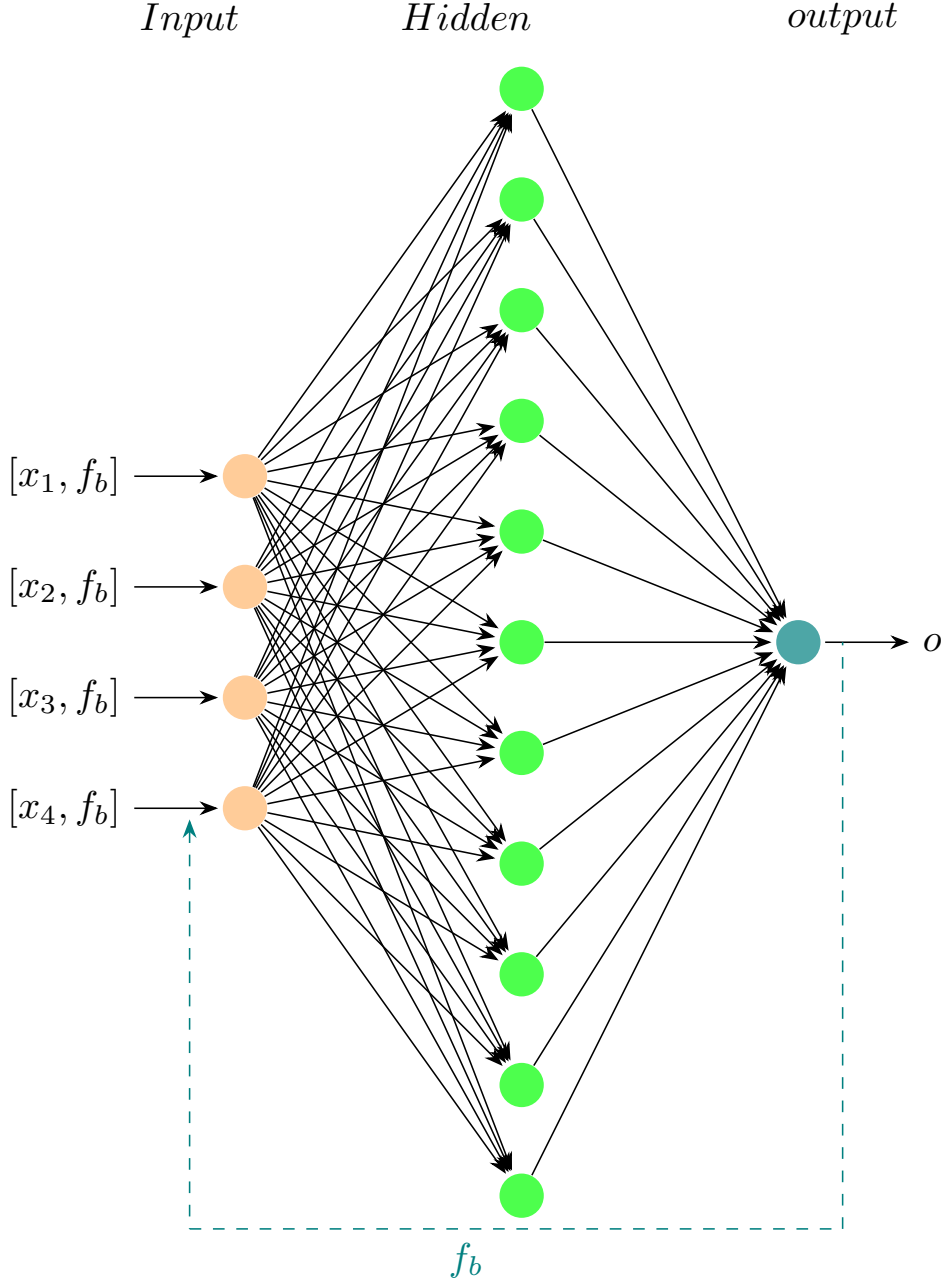


Figure 1. The simulation model architecture for NARX network. Where x_1-x_4 are the input values to the model input neurons (faint orange), the 11 green nodes in the middle are the hidden layer neurons while the teal node is the output layer neuron with o denoting the predictions. Finally, the feedback is denoted by f_b .

165 loop represented by f_b is the previous values from the model output, $o[t-1], \dots, o[t-4]$.
 166 Essentially, a dynamic neural network with the time steps synchronized data, $o[t]$ and
 167 $x[t]$ is illustrated by Figure 1. Figure 2 demonstrates the internal validation outcome of
 168 the NARX model performance on data during learning to obtain the optimum model
 169 with the best performance and less computation time. The first model's performance eval-

170 uation step was based on root mean square errors (RMSE) versus the number of nodes
 171 in the hidden layer. It became hard to select the model based on the first evaluation as
 172 there were many optimal model candidates based on this evaluation. Therefore, the sec-
 173 ond selection criterion on the regression against the number of neurons in the hidden layer
 174 was examined. Generally, we noticed all models qualify for learning machines except those
 175 below $N=8$. Where N is the number of nodes in the hidden layer. The argument on the
 176 error difference in RMSE and R values being less than a unit left the best choice to rely
 177 on the computation time. Keeping the same N and monitoring their computation time
 178 with a reasonable number of epochs to ensure no underfitting and overfitting in the learn-
 179 ing. Then that of fast computation time was selected. In principle, each dot plotted in
 180 Figure 2 represented a trained network against the number of hidden layer neurons in
 181 the x-axis and performance in the y-axis, upon which the optimal model is taken after
 182 25 trials. The selected optimal NARX model for the current work was the one with 11
 183 neurons in the hidden layers and an RMSE of 3.44 nT and $R=0.75$ as shown with the
 teal dashed line and red point in Figure 2 (a) and (b).

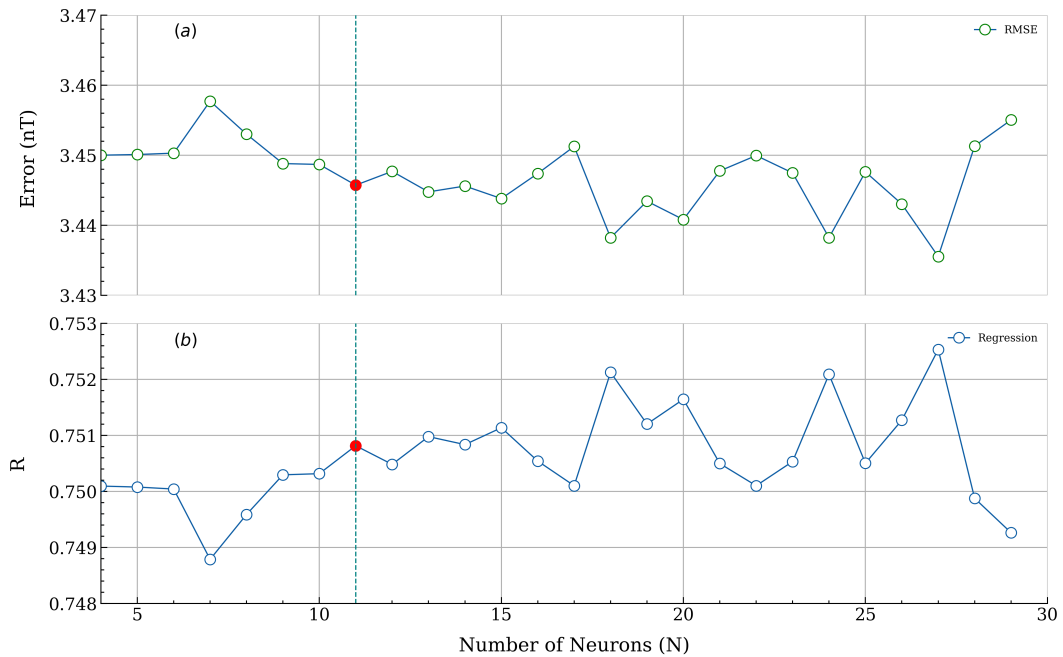


Figure 2. NARX model optimization profile of root mean square error and R versus the number of neurons in the hidden layer. The teal color dashed line indicates the selected number of neurons versus RMSE values for the present model for the prediction of Pc5 pulsation. The optimal model was (11,3.44) and (11,0.75) in terms of computation time.

184

185 3 Data and methodology

186 The ground magnetic field data of one minute resolution was obtained from the Sval-
 187 bard network for a period of 25 years from 1996 to 2020. These data were preprocessed
 188 and transformed into H-magnetic field coordinates from their X and Y-corrected geo-
 189 magnetic components. Svalbard network comprises 5 observatories, Bear Island (BJN),
 190 Hopen Island (HOP), Hornsund (HOR), Longyearbyen (LYR), and Ny Alesund (NAL).
 191 Pc5 pulsations were extracted by bandpass filtration technique from the H-component
 192 using Butterworth digital filter design (Omondi et al., 2023). The space events polar-

193
194

ized east-westward and south-northward are all captured by the H-component. Therefore, the H-component accounts for both local and global Pc5 pulsation beatings that would be observed worldwide during geomagnetic activity. Figure 3 illustrates the ge-

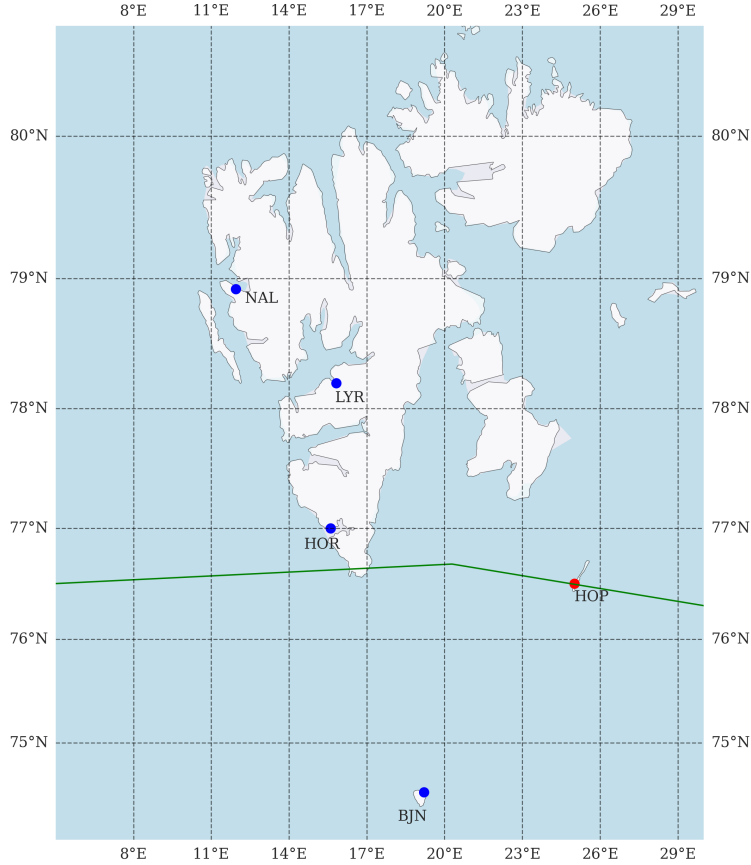


Figure 3. Topographical map of Svalbard network in the auroral region. The green-colored meridian is a line corresponding to the geomagnetic latitude recording the maximum amplitude and intensity of Pc5 pulsations, 73° .

195
196
197
198

ographical map of ground-based space monitoring stations of the Svalbard network. The green-colored meridian corresponds to the geomagnetic meridian of maximum Pc5 amplitude and intensity receptions (Pilipenko et al., 2001).

199
200
201
202
203
204
205

Benchmark of the previous study conducted by Omondi et al. (2023) to detect auroral Pc5 pulsations using machine learning; they found that the Pc5 pulsations under investigation were recorded simultaneously in the Svalbard network. Therefore, the same conclusion is applied in the current study. For this work, we used the NAL station in modeling machine learning algorithms in the training phase and the other four stations were used in the deployment of the model during the testing phase. The northward geolocation of the NAL observatory (75.25°) to other stations in the Svalbard network was

of interest as it is on the outer or near outer edge of the auroral oval strip (65°-75° magnetic latitude) since it records fairly clean space events relative to others in the auroral oval. Deployment of the machine learning model in other stations in the Svalbard network aside from the used to train it presents an interesting evaluation of the capability of the machine learning model in the complex data environment. Given that stations in the network receive the same Pc5 waves in terms of the frequency band, they are polarized differently (phases) with fluctuating powers dependent on the L-shell values.

The solar wind parameters observed near the Lagrange's (L-1) point of 1 minute cadence starting from 1996 to 2020 were employed. In particular, to train our machine learning algorithms, we selected four solar wind parameters measured near L-1 point; these parameters are regarded as the most important drivers triggering geomagnetic activity causing Pc5 pulsations. These variables comprise the Z-component of the interplanetary magnetic field magnitude (IMF- B_z) in GSM coordinate, the plasma temperature (T_e), the proton density (n_p), and the earthward solar wind velocity (V_x). The Z-component of the interplanetary magnetic field (IMF- B_z) contributes largely to the amount of momentum and energy transport from the solar wind to the Earth's magnetosphere by magnetic reconnection at the dayside magnetopause (Dungey, 1961). Thus, the knowledge of (IMF- B_z) fields is key for monitoring and forecasting the energy input into the magnetosphere-ionosphere system. Therefore, to guide the modeling of the non-linear system, the machine was to learn from the solar wind parameters with the Pc5 waves as the target.

The input datasets were wrangled to remove missing data and transformed into intelligible data suitable for machine learning, finally, synchronized with the Pc5 pulsations to have the same data frames. The data were partitioned into two categories, the training set spanning 17 years and shuffled 8 years of data from two solar cycles, 23 and 24 for testing or deployment purposes. In the training phase, we partition data 70% training, 15% internal testing, and 15% validation. The training dataset was randomly extracted from the 17 years of simulation time series distributed over two solar cycles, 23 and 24. The validation was done using Kp and F-10.7 indices, 27 days averaged with the model evaluation results from the test data. The Kp and F10.7 indices data set of 25 years from 1996 synchronized with 8 years of test data from two solar cycles. The training algorithm was based on the error back-propagation algorithm. The Levenberg-Marquardt backpropagation which uses `trainlm` to learn was utilized because it is faster to train (Omondi et al., 2023). For every epoch, the loss function (cost function) is calculated by Eqn. 3.

$$E = \frac{1}{2} \sum_{j=1}^M (T_j - O_j)^2 \quad (3)$$

where T_j and O_j are the true output and prediction output, where M is the number of the training samples (Cai et al., 2009). The prediction performance was obtained using the mean square error (MSE):

$$MSE(O, \hat{O}) = \frac{1}{m} \sum_{j=1}^m (O_j - \hat{O}_j)^2 \quad (4)$$

where the O_j is the j^{th} of m output of the initial open net network with T_e , IMF- B_z , n_p and V_x as its input, and \hat{O}_j is corresponding output as predicted by NARX. The root mean square error was calculated from the square root of MSE in equation 4. The cross-correlation coefficient, R, is given by equation 5.

$$R(O, \hat{O}) = \frac{1}{m} \sum_{j=1}^m \left(\frac{O_j - \mu(O)}{\sigma(O)} \right) \times \left(\frac{\hat{O}_j - \mu(\hat{O})}{\sigma(\hat{O})} \right) \quad (5)$$

The R values are used to determine the prediction accuracy of the neural network. where $\mu(\hat{O})$ and $\mu(O)$ represent the mean values of the predictions results and observations, respectively. $\sigma(\hat{O})$ and $\sigma(O)$ are the standard deviations.

250 Time series comprising nonstationary power at many distinct frequencies can be
 251 analyzed by wavelet transform (Daubechies 1990). Supposing that one has a time series
 252 observation, y_m , with equal time spacing δt and $m=0 \dots M-1$. If one also has wavelet functions, $\psi(\xi)$,
 253 which is dependent on a non-dimensional ‘time’ parameter ξ . To be permitted as a wavelet,
 254 this function must be localized in both frequency and time space and also have zero mean
 255 (Farge 1992). Consider the Morlet wavelet, consisting of a plane wave modulated by a
 256 Gaussian:

$$\psi_0(\xi) = \pi^{-\frac{1}{4}} \cdot e^{i\omega_0\xi} \cdot e^{-\frac{\xi^2}{2}} \quad (6)$$

257 where nondimensional frequency is given by ω_0 and taken to be 6 to satisfy the admis-
 258 sibility condition (Farge 1992). The continuous wavelet transform of y_m discrete signal
 259 is defined as the convolution of y_m with a translated and scaled version of $\psi_0(\xi)$:

$$W_m(s) = \sum_{m'=0}^{M-1} y_{m'} \psi^* \left[\frac{(m' - m)\delta t}{s} \right] \quad (7)$$

260 where the complex conjugate is indicated by (*).

$$\hat{\psi}(s\omega_k) = \left\{ \frac{2\pi s}{\delta t} \right\}^2 \psi_0(s\omega_k) \quad (8)$$

261 For morlet wavelet, the function $\hat{\psi}_0(s\omega_k) = \pi^{-\frac{1}{4}} \cdot H(\omega) \cdot e^{-\frac{(s\omega - \omega_0)^2}{2}}$ and each of the un-
 262 scaled $\hat{\psi}_0$ is defined to have $\int_{-\infty}^{+\infty} |\psi_0(\hat{\omega}')|^2 d\omega' = 1$, i.e they have to be normalized to a
 263 unit energy. Utilizing Normalizations at every scale s one has

$$\sum_{k=0}^{J-1} |\hat{\psi}(s\omega_k)|^2 = J \quad (9)$$

264 where the number of points is given by J . Using the convolution formula in equation 7,
 265 the normalization of the wavelet function is given by:

$$\psi \left[\frac{(m' - m)\delta t}{s} \right] = \left(\frac{\delta t}{s} \right) \psi_0 \left[\frac{(m' - m)\delta t}{s} \right] \quad (10)$$

266 where energy of $\psi_0(\xi)$ is normalized to unity. If the wavelet function $\psi(\xi)$ is complex,
 267 then its transform will also be complex, $W_m(s)$. Therefore, the real and complex com-
 268 ponents of wavelet transform are expressed as $\Re\{W_m(s)\}$ and $\Im\{W_m(s)\}$ respectively.
 269 The amplitude and phase of the wavelet transform are obtained as $|W_m(s)|$ and $\tan^{-1} \left[\frac{\Im\{W_m(s)\}}{\Re\{W_m(s)\}} \right]$
 270 correspondingly. Consequently, the wavelet power spectrum is defined by $|W_m(s)|^2$. Af-
 271 ter the successful selection of the wavelet function, the immediate task is to choose scales, s ,
 272 to use in the wavelet transform. Therefore, wavelet scales are written as a set of frac-
 273 tional powers of 2 shown in equations 11 and 12.

$$s_n = s_0 2^{n\delta n}, \quad n=0,1,2,\dots,N \quad (11)$$

274

$$N = \frac{\delta}{n} \log_2(J\delta t/s_0) \quad (12)$$

275 Where N and s_0 are the largest and smallest scales. In the Morlet wavelet, $\delta n = 0.5$
 276 is the largest permitted value that gives enough sampling in scales. Given that wavelet
 277 transform is essentially a bandpass filter with a known wavelet function (response func-
 278 tion). The original time series can be reconstructed after wavelet transformation using
 279 either an inverse or deconvolution filter. In our case, the original signal was reconstructed
 280 by taking the sum of the real part of the wavelet transform over all scales.

$$y_m = \frac{\delta_n \delta_t^{\frac{1}{2}}}{C_\delta \psi_0(0)} \sum_{n=0}^N \frac{\Re [W_m(s_n)]}{s_n^{\frac{1}{2}}} \quad (13)$$

281 The energy scaling is removed by $\psi_0(0)$ and the conversion of wavelet transform to en-
 282 ergy density is performed by $s_n^{\frac{1}{2}}$. The C_δ is the reconstruction factor of δ from its wavelet
 283 transformation using $\psi_0(\xi)$. Given a new wavelet function, C_δ can be derived by tak-
 284 ing time series of a δ function at times $m = 0$ provided $y_m = \delta_{m_0}$. Therefore, the wavelet
 285 transform becomes:

$$W_\delta(b) = \frac{1}{M} \sum_{k'=0}^{M-1} y_{m'} \psi^*(s\omega_k) \quad (14)$$

286 The reconstruction of equation 14 is:

$$C_\delta = \frac{\delta_n \delta_t^{\frac{1}{2}}}{\psi_0(0)} \sum_{n=0}^N \frac{\Re\{W_\delta(s_n)\}}{s_n^{\frac{1}{2}}} \quad (15)$$

287 where, the C_δ is constant and scale dependent for every wavelet function. Following the
 288 energy conservation principle the total energy is conserved and Parseval's theorem for
 289 wavelet analytics is:

$$\sigma^2 = \frac{\delta_n \delta_t^{\frac{1}{2}}}{C_\delta M} \sum_{m=0}^{M-1} \sum_{n=0}^N \frac{|W_m(s_n)|^2}{s_n^{\frac{1}{2}}} \quad (16)$$

290 where δ is for the reconstruction and σ^2 is the variance.

$$\overline{W_m^2} = \frac{\delta_n \delta_t^{\frac{1}{2}}}{C_\delta} \sum_{n=n_1}^{n_2} \frac{|W_m(s_n)|^2}{s_n^{\frac{1}{2}}} \quad (17)$$

291 Equation 17 and 16 illustrates wavelet scaled power averaging of a wavelet transform in
 292 the signal transformation and reconstruction formulations. After training the ML model,
 293 its performance was evaluated by wavelet power spectrum analysis. Thresholds for dis-
 294 tinguishing predicted events and non-events were set guided by wavelet power transform
 295 techniques. This technique was performed by passing the machine learning output sig-
 296 nal through a filter-like algorithm (wavelet power transform) to define the predicted Pc5
 297 events from background noise. This concept is visualized in the schematic diagram shown
 in Figure 4.

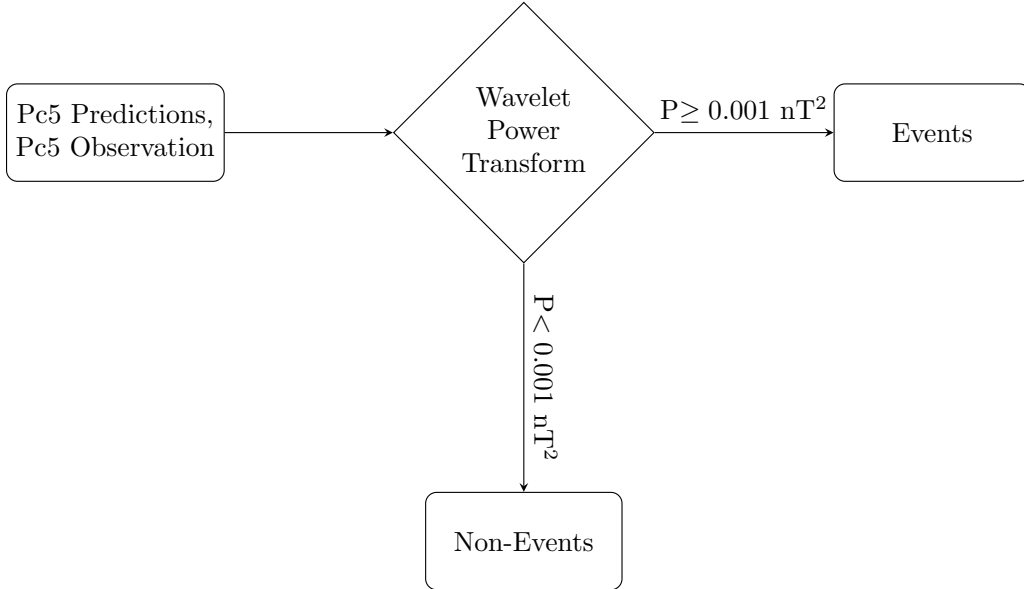


Figure 4. Illustration of Pc5 Event definition from forecast results

4 Results and Discussion

4.1 Network Performance

In the current study, we present the NARX neural network as a machine learning (ML) tool in predicting Pc5 pulsations. The network took 142 out of 1000 epochs to train the model with a performance of $MSE=11.90 \text{ nT}^2$. The overall training time of about 00:18:25 hours was observed. The number of epochs and time taken to train the model was fair enough to qualify good learning indicating that there were no overfitting and underfitting. Therefore, it was arguably convincing to state that the model indeed found it easy to learn from the data and regularize with the target data to yield a good performance. The resultant model's intelligible weights and biases were pictorially presented using the Hinton diagram shown in Figure 5. The color coding of the squares represents the weight and bias signs values, whereby red and green colors correspond to negative and positive values respectively. The scale size of each square is equivalent to the weight and bias magnitude values in each layer having a maximum magnitude equal to 1. The Hinton diagram demonstrates neuron connections of the learned model between inputs, hidden layer, and output giving more insight into trained weights distribution. To unravel the black box of the artificial network or network intelligence of the trained model, Figure 5 gives the intuition. In layer 1 of Figure 5 there are 8 parallel inputs in input 1 comprising of connection from 4 external inputs and 4 context inputs (feedback) to the 11 hidden nodes in the hidden layer forming an 8 by 11 network matrix. Hence, the overall distribution of weights in layer 1, input 1, is 88 connections and 88 weights. In the input 2, layer 1, there are 11 biases and 22 weights. In Layer 2 (the connection between the hidden layer and output) there are 11 weights and 1 bias. Contrary to Figure 1, the same arrangement as in Figure 5 was expected but there are only 4 inputs defined by input attributes looped with feedback. At the initial condition, the extra 4 context input does not exist as there is no output. These context inputs are automatically created during the machine-learning process. Therefore Hinton diagram comes in handy to give the resultant picture of the trained model weights and network distributions with more details. Overall, the ML model demonstrated a strong node connection.

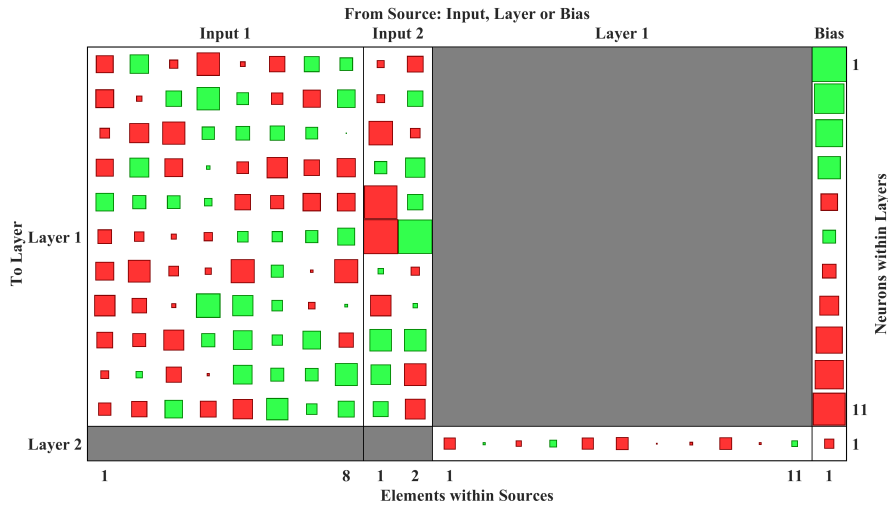


Figure 5. Hinton diagram of ML model showing trained weights and biases with their corresponding values and magnitudes. The diagram demonstrates strongly connected neurons presenting good learning. Where green and red colors are positive and negative values respectively. The size of the square represents the element magnitude.

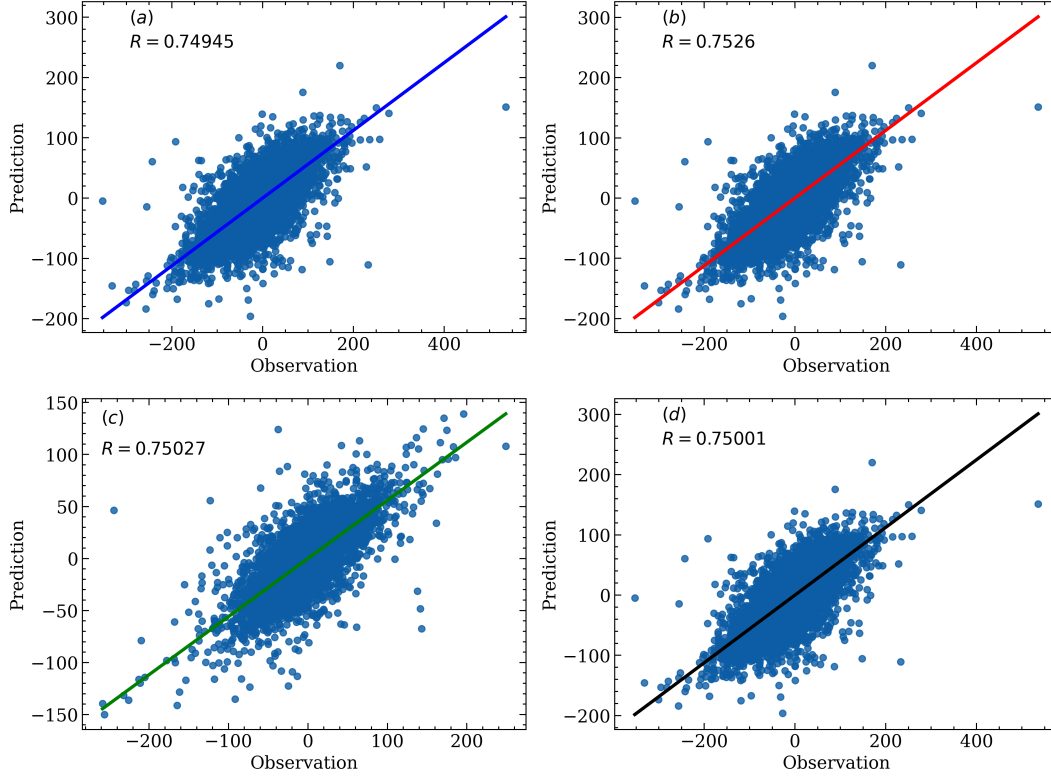


Figure 6. Machine Learning training results for 17 years of the two cycles, 23 and 24. Where (a)-(d) are scatter plots for training, testing, validation, and finally the overall performance.

327

328 Figure 6 shows the internal network evaluation in the training phase. Hence, the
 329 regression coefficient of the training, testing, validation, and general performances yielded
 330 an overall of 0.75. Hence, scaling well with big data. Despite high amplitude spikes and
 331 outliers in the data, the model responded with a good performance in the training phase.
 332 The model generalizes well with R values of 0.7495 indicating good learning. Validation
 333 and internal testing showed a good consistency between prediction and observation having
 334 R values of 0.75 overall. The metric measurement of the model training realizes an
 335 RMSE of 3.44 nT and MSE of 11.90 nT².

336

4.2 Model Performance on test data

337 After the training phase, the resultant simulation model was deployed on test data
 338 to evaluate its performance and robustness. Figure 7 shows the regression between ob-
 339 servation (target) and the prediction for both high and low solar activities from some
 340 selected years in the ascending and descending phases of solar cycles 23 and 24. Figure
 341 7 (a-c) illustrates the network model performances for the years 1999, 2002, and 2010
 342 with an averaged R-value of 0.76 while Figure 7 (d) shows the yield for the year 2020
 343 having R-value of 0.57. The metric evaluation on MSE also yielded 9.15 nT², 8.23 nT²,
 344 3.70 nT², and 24.52 nT² for 1999, 2002, 2010, and 2020 respectively. The performance
 345 in the year 2020 was unusual compared with other years in the test case, possibly due
 346 to the complexity of the dataset. Comparing 2020 performance generally with other years'
 347 test data as shown in Figure 15, the number of prediction events was also anomalous con-
 348 trary to the expectation as observed in the year 2009. This points out the dynamic re-
 349 sponse of the model to different dataset complexities. Overall, there was a good corre-

350
351

lation between prediction and observation with a performance of $\text{MSE} = 11.40 \text{ nT}^2$ despite uncertainties in the datasets.

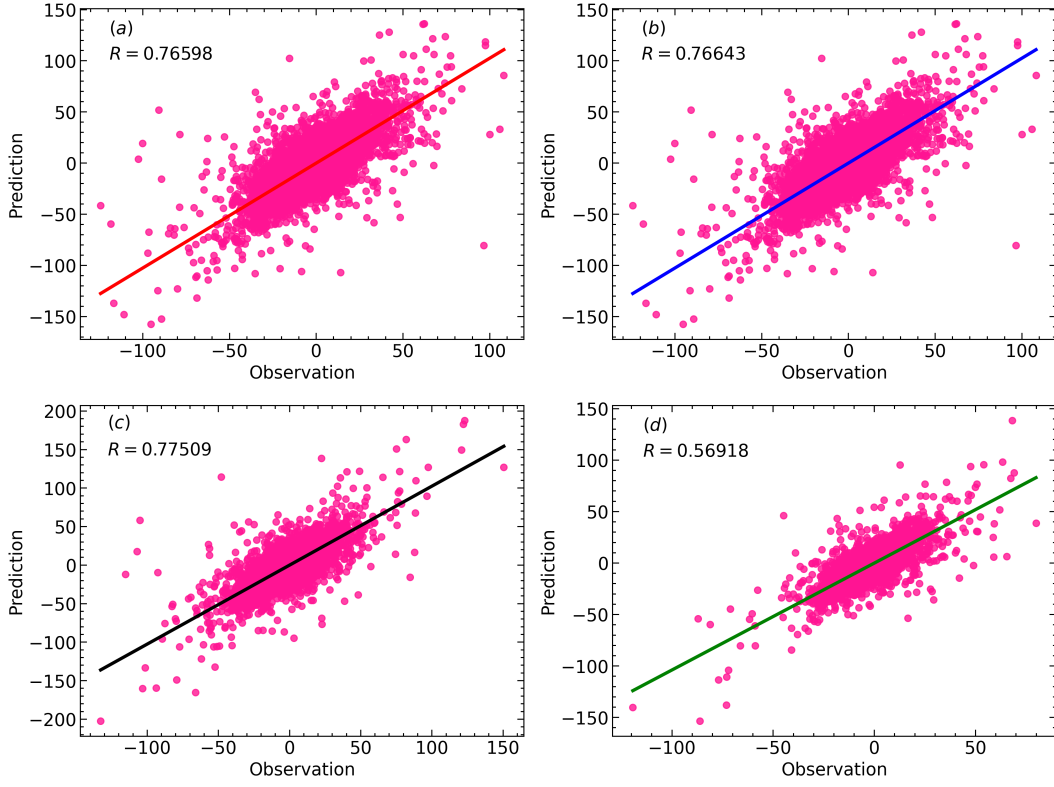


Figure 7. Machine learning test performance on a fresh data set of both active and high solar wind activities spanning both phases of solar cycle 23 and 24. Where (a),(b), (c), and (d) are test responses of the years 1999, 2002, 2010, and 2020 response from the NAL observatory respectively.

352
353
354
355
356
357
358
359
360
361
362
363
364
365
366
367
368
369

The model was also deployed to study the response to a strong geomagnetic storm. Therefore, the geomagnetic storm of St. Patrick's Day of March 17th, 2015 with maximum Ap and Kp indices of 108 and 8- ($7\frac{2}{3}$) respectively was picked as an illustrious case study. This storm was strong and caused disturbances in the magnetospheric current system and energy injection into the magnetosphere cavity. As a consequence, the injected energy resulted in the generation of plasma waves. These waves contribute to the transportation of momentum, mass, and energy in the entire geospace. Given that Pc5 waves are giant plasma waves of ultra-low frequency with wider bands generated from field line resonances. Thus, this became the first step of the model deployment of the Pc5 prediction in the nonlinear conditions of the magnetospheric system. Figure 8 shows the spectral analysis of the machine learning prediction outcome and Pc5 observation on the St. Patrick day. The zoomed plot of Figure 8 highlights a clear visualization of the relationship between ML output and the observations. There exists a strong match between the observation and ML outcome throughout the day with some small amount of outlier spikes. Overall, the predicted Pc5 wave patterns were excellently reproduced and had a good correlation with observation. Time-frequency and spectral characteristics of the prediction against the observation were studied in Figures (9 and 10) using the time window of intense Pc5 pulsation highlighted in teal color in Figure 8.

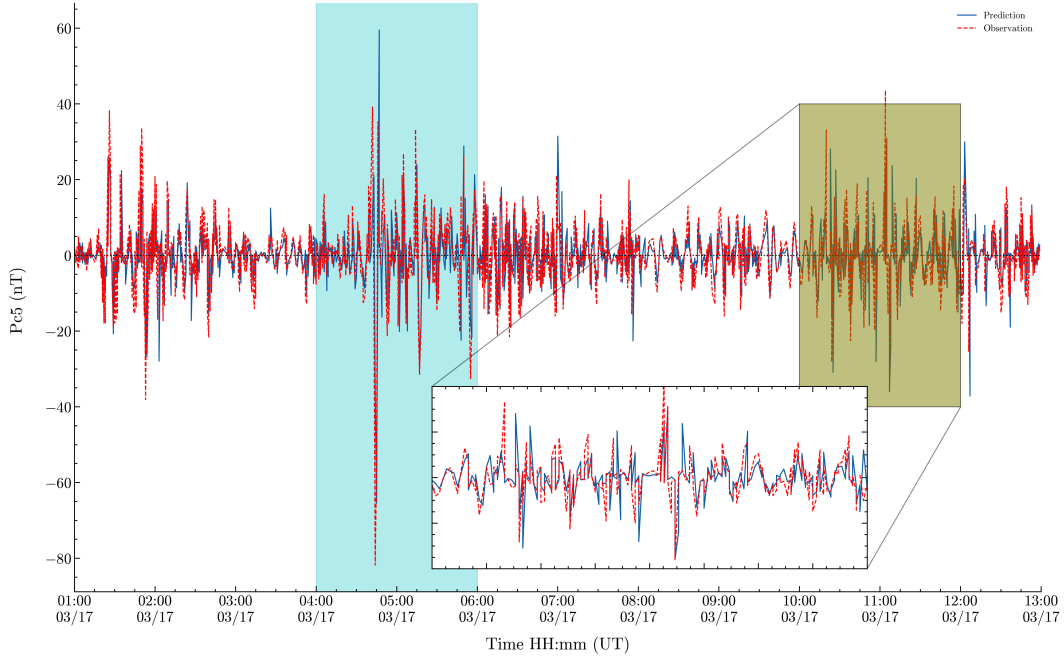


Figure 8. Time series prediction and observation plot on the geomagnetic storm of March 17, 2015 at NAL observatory. The zoomed graph shows the correlation between observation and prediction highlighted in light olive color.

370 Figure 9 shows wavelet analytics of the Pc5 prediction and observations correspond-
 371 ingly. Whereby, Figure 9 (a) & (b) are the scalograms of the actual observations and pre-
 372 dictions of Pc5 pulsations of the Morlet wavelet continuous transformation. The scalo-
 373 grams were of the signals highlighted in teal color in Figure 8. The signature of high am-
 374 plitudes seen in Figure 8 both for observation and predicted Pc5 dominated as well in
 375 the scalogram presenting high energy pulsations. Surprisingly, the prediction scalogram
 376 is more filtered than the observation one with clear patches, this is because of the wavelet
 377 time-frequency duality property. Fundamentally, the wavelet transformation works on
 378 the identification of real signals from noise-infested signals on the principle of time-frequency
 379 features. Figure 9 (a) and (b) show Pc5 signals corresponding to their frequencies and
 380 the approximation in green color. On the other hand, the Pc5 prediction event defini-
 381 tion was based on the analyses of Figure 9, 10 and 11. Therefore, carrying out the scale-
 382 averaged wavelet power spectrum analyses, the wavelet filter banks and signal in the in-
 383 put of the scaled-averaged wavelet function return the scales-averaged signals with their
 384 frequency and period coefficients. Figure 10 (c) & (d) are the scaled-averaged wavelet
 385 power spectra of Pc5 pulsations and predictions respectively. The results in 9 (a) & (b)
 386 and Figure 10 (c) & (d) showed that the detected Pc5 signals in the scalograms corre-
 387 spond to the energized power wavelet coefficients of the same signals having a good match.
 388 These report that the predicted signal was indeed Pc5 pulsations piloting further anal-
 389 yses to define the pure waves based on wavelet power analysis. To identify clean Pc5 pul-
 390 sations predictions against actual observation, the forecasted data were threshold at 0.001
 391 nT² against observations schematically demonstrated in Figure 4.

392 On the other hand, the event definition using the wavelet power spectrum technique
 393 was employed on a minor geomagnetic storm of January, 5th 2015 as a bare minimum
 394 of geomagnetic conditions. This was to account for Pc5 pulsations occurring due to magnetosphere-
 395 solar wind coupling dynamics other than the coronal mass ejections. Figure 11 (a) and
 396 (b) shows the Wavelet scale-average wavelet power spectrum of Pc5 pulsations of Jan-

397 uary, 5th 2015 minor geomagnetic storm. In comparison to Figure 10 (a) and (b), it was
 398 observed that the magnitude of normalized Pc5 pulsations was ten times as to the re-
 399 sponse in Figure 11 (a) and (b). This demonstrates the strength of St. Patrick's strong
 400 geomagnetic storm to minor storm. For this reason, the Pc5 events were defined using
 401 the observation in Figure 11 (a) and (b). In the previous study, Omondi et al. (2023)
 402 defined their Pc5 prediction events on the threshold above 20 nT. Historically in the auroral
 403 zone, it is well known to record large Pc5 pulsations. Therefore their threshold was
 404 to exclude ULF waves contributed by background noise as well as maintaining pulsations
 405 recorded in the quiet days. In the current study, ULF waves were detected using mor-
 406 let wavelet transform to observe time-frequency response and invite further diagnosis.
 407 Observing that these signals within the Pc5 band for both, there was a need to exclude
 408 those that mimic Pc5 waves by using wavelet power spectrum as they represent the back-
 ground noise.

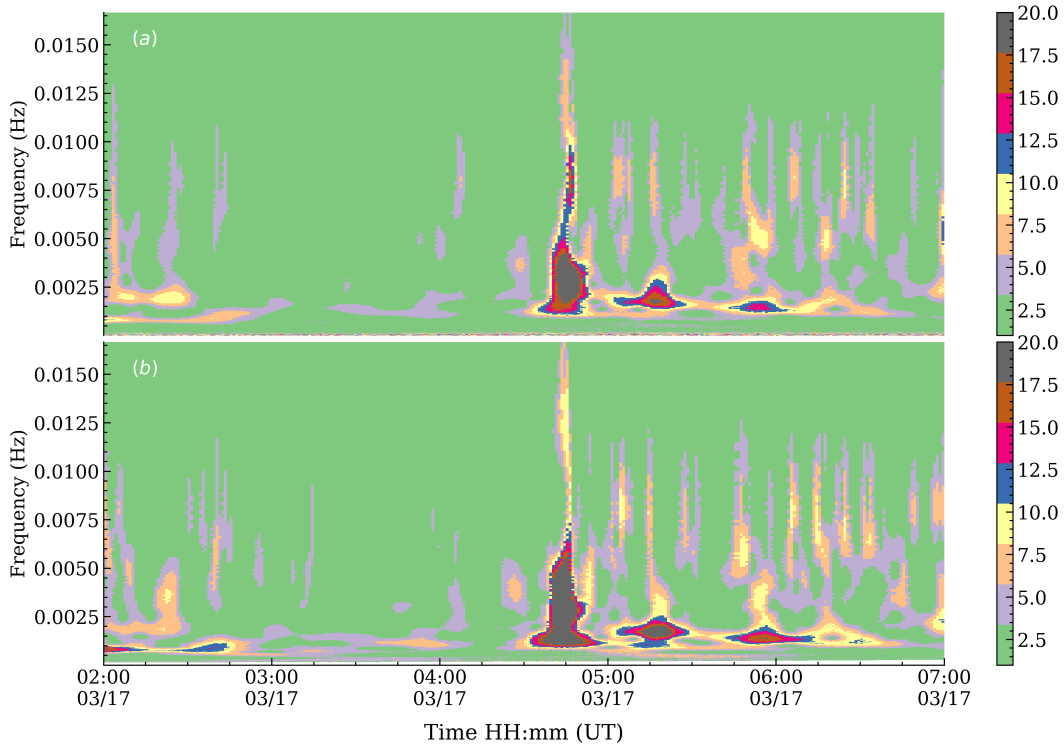


Figure 9. Wavelet analyses of Pc5 pulsations. Panels (a) and (b) are scalograms of actual Pc5 and Predicted. The measurement recorded on the geomagnetic storm occurred on St. Patrick day of March 17, 2015. The analysis presented corresponds to the highlighted section in cyan color in Figure 8.

409

410 Figure 12 (a) & (b) demonstrates the Pc5 events and non-events of the predictions
 411 and actual measurements respectively. These observations give more insights into Fig-
 412 ure 9 as hot colors corresponding to Pc5 events with a higher power as in Figure 12 (a).
 413 Consequently, the cool colors in the scalograms are background noise which is consid-
 414 ered non-events. Whereby, the hot colors are those greater than 5 while the cool ones
 415 are those within or less than 5 as indicated in the color bar. Therefore, wavelet power
 416 spectra and continuous wavelet transformation of the Pc5 pulsations analyses were im-
 417 portant in the determination of the number of Pc5 pulsations predicted in each station
 418 in the Svalbard network. Figure 12 (a) shows that there are more actual Pc5 events com-

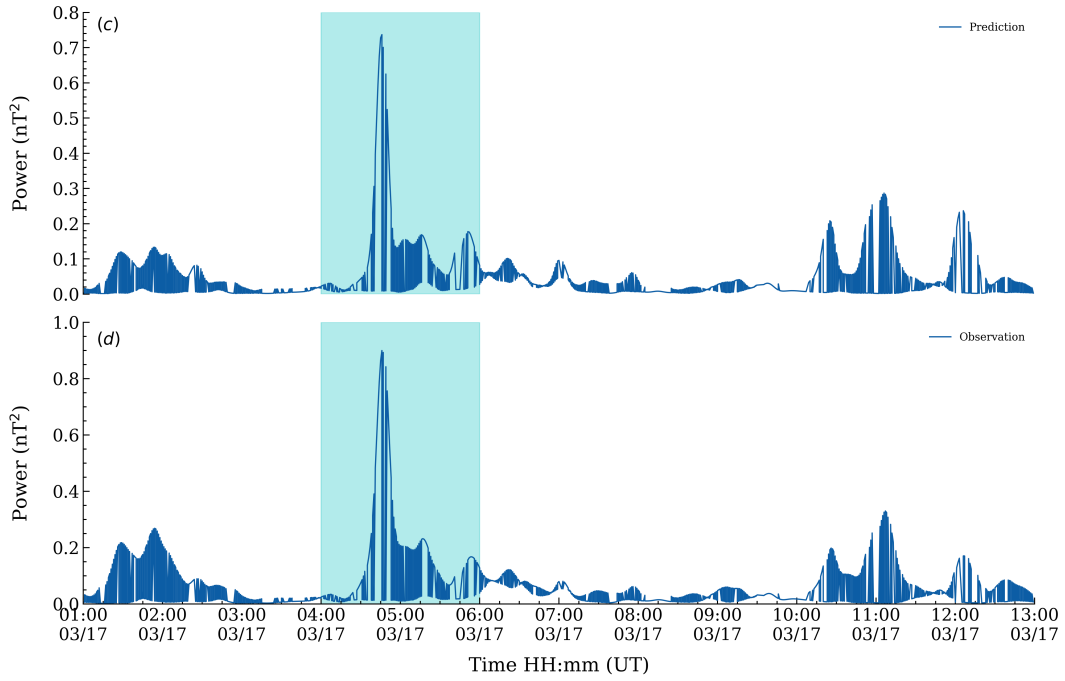


Figure 10. Wavelet scale-average wavelet power spectrum of Pc5 pulsations. Panels (c) and (d) are scaled-averaged wavelet power spectra. of prediction and observation. The highlighted area with cyan color corresponds to the study presented in Figure 9 and 8

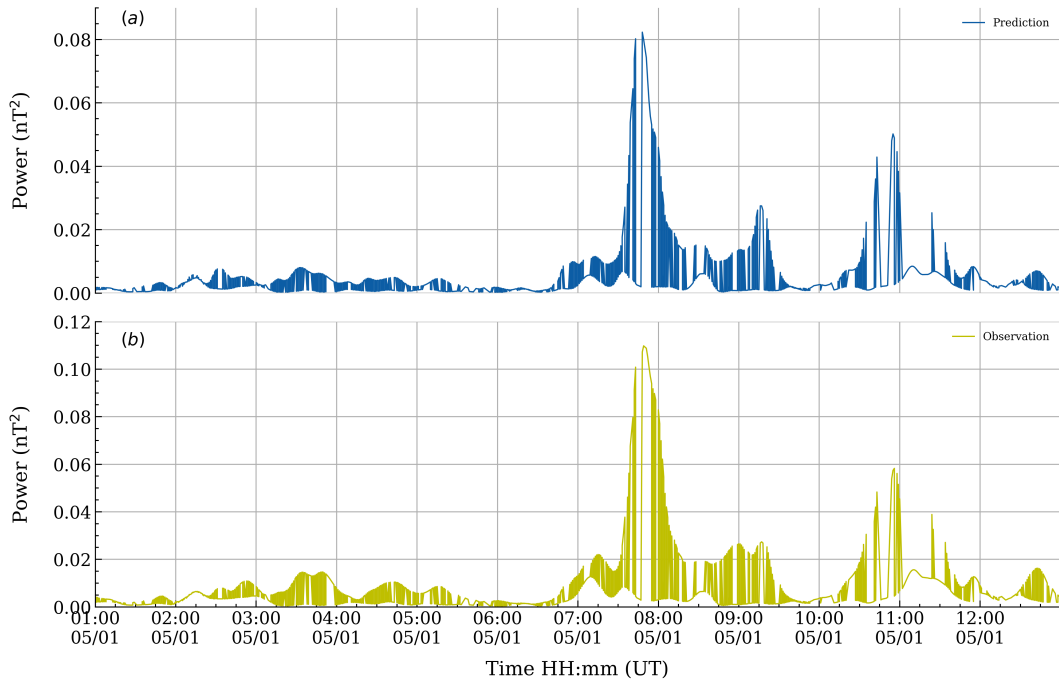


Figure 11. Wavelet scale-average wavelet power spectrum of Pc5 pulsations. Panels (a) and (b) are scaled-averaged wavelet power spectra of prediction and observation recorded on January, 1st 2015.

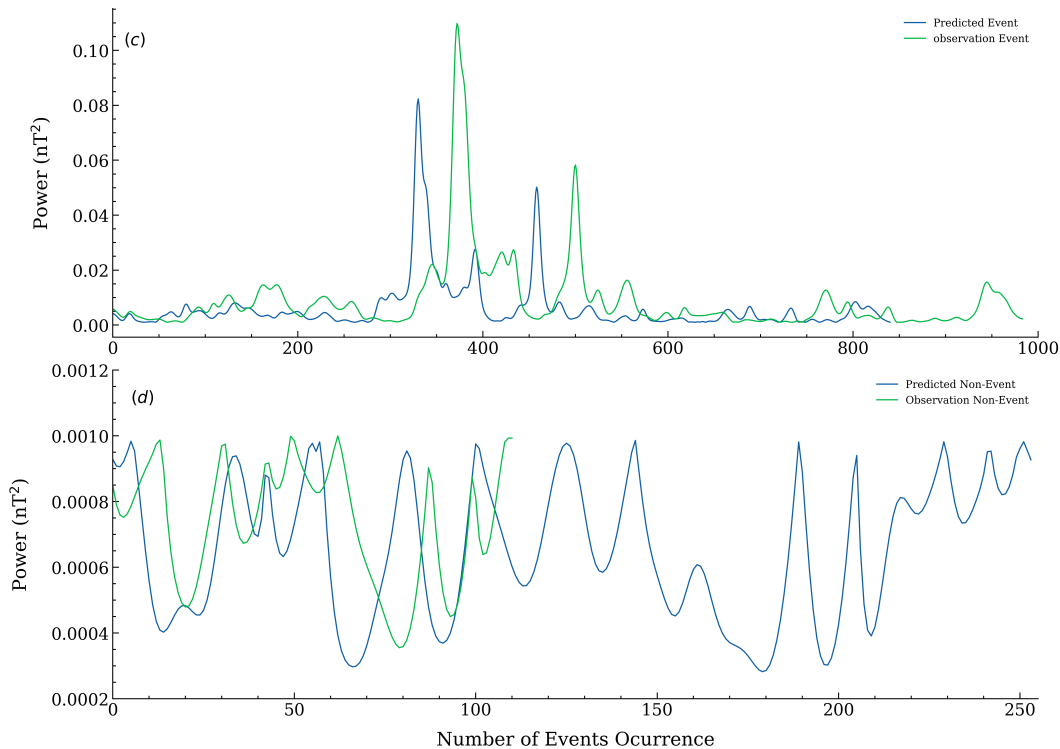


Figure 12. Pc5 event definition by wavelet power transform. Panels (c) and (d) are the predicted scaled-averaged Pc5 events and non-events respectively. These measurements are extracted from the response illustrated in Figure 11

419 compared to the number of predictions. This is accounted for by the loss function, given that
 420 we had a regression of 0.75 on average, implying that 0.25 of the original signals were
 421 lost. Nevertheless, the model was within an acceptable level and the prediction results
 422 showed similar results seen in Figure 12 (a). Table 4.2 illustrates the number of Pc5 pre-
 423 diction outcomes from the Svalbard network with NAL recording the least and HOP the
 424 highest in the year 1996. These unique results correspond to the latitudinal distributions
 425 of stations in the auroral strip and the geomagnetic activity in the region. Field line res-
 426 onance theory dictates that these ULF waves are produced by remote Alfvén oscillations
 427 in the magnetospheric Alfvénic resonator excited by MHD fluctuations from the local
 428 part of the magnetosphere. Hence, Pc5 waves peak at the latitude where the external
 429 disturbance frequency resonates with the local Alfvén frequency. Pilipenko et al. (2001)
 430 reported a possible relationship between AEJ current and Pc5 waves in the auroral lat-
 431 itude of maximum peak and intensity of the events, 73°. They argued that the Pc5 re-
 432 sponse is stimulated by the intensification of eastward AEJ with a noticeably lower mag-
 433 nitude compared to the westward AEJ. Given that the HOP station lies on the latitude
 434 of field line resonance, consequently had to record the highest corresponding to the pre-
 435 diction results.

436 The model was tested in a quiet geomagnetic condition of a weak auroral geomag-
 437 netic activity of October 23rd, 1996. This was a minor geomagnetic storm with a max-
 438 imum kp index of +7 and Ap=37. Generally, 1996 was a quiet geomagnetic year in the
 439 minimum phase of solar cycle 23. Deploying the model in other Svalbard stations ex-
 440 cept for the NAL station on the storm of October 23rd, 1996 provided astonishing re-
 441 sults. Thus, the time series prediction against actual measurements in the Svalbard net-

Table 1. Number of Pc5 pulsations predicted in the Svalbard network for the year 1996. Where Mlat is the magnetic latitude.

Station code	Mlat	Station Name	Number of Pc5 Predictions
NAL	75.25	NyAlesund	2091
LYR	75.12	Longyearbyen	3584
HOR	74.13	Hornsund	6181
HOP	73.06	HopenIsland	6949
BJN	71.09	BearIsland	6625

work was illustrated by Figure 13 and 14. Whereby, the time series observations and predictions are shown by red dotted and blue solid lines respectively.

Figure 13 (a)-(b) and Figure 13 (c)-(d) shows the model test results predicted from LYR & HOR, and HOP & BJN correspondingly. It was observed that each ground observatory observation showed a good match with the predictions illustrating the stability and integrity of the model in terms of performance. In the Four observatories, it was also noted that the HOP station' prediction response to pulsations observations recorded maximum amplitudes with more than 100 nT than other stations. The BJN & HOR recorded second and third highest, and finally, LYR recorded the lowest. The finding supports the previous studies on the auroral Pc5 pulsation characteristics (Pahud et al., 2009). This was possibly contributed by the electrodynamic convection processes resulting from ionosphere-magnetosphere current systems in the auroral strip (Rostoker & Lam, 1978). The spatial and temporal variation of Pc5 ULF waves is co-related to the location of the auroral electrojet, therefore, the maximum Pc5 wave responses are observed at the latitude of the maximum AEJ peak. Overall, the fundamental feature of auroral Pc5 pulsation such as frequency component and amplitude was predicted with higher accuracy. At last, despite complexities in the data, the model deployed in those observatories performed well with a high degree of accuracy. The spikes and inherent features of each signal in the Svalbard network were reproduced with a good consistency to the original signal. Demonstrating the power of the NARX model in nonlinear system modeling (Billings, 2013).

ULF wave power has shown dependence on L-shell and solar wind activity. There exists a strong consistency between ULF wave power and solar activity (Kessel et al., 2004), especially in the declining phase of the solar cycle having the highest correlation when the radiation belts are active (Li et al., 2011; Mann et al., 2004). Most studies have demonstrated that solar wind is the key external source and control of the geomagnetic pulsations (Mathie & Mann, 2001). Mathie and Mann (2001) pointed out that Pc5 waves decay exponentially with a declining L shell, and the decay rate increases with solar wind speed, showing a stronger dependence of ULF wave power on solar wind speed at higher L shells of the band L=3.75–6.79. The decreasing Pc5 amplitude from HOP to BJN and LYR observatories on either side of the auroral magnitude latitude (73°) as illustrated in Figure 13 and 14 are in agreement with the Rae et al. (2012) findings. Rae et al. (2012) broadened the range of L-shells in the study of Mathie and Mann (2001) to both higher and lower values and found that the ULF wave power decreases toward the higher L-shells (L=8) as well as toward lower L shells.

Ozeke et al. (2014) used statistical THEMIS and GOES observations to come up with the analytic expression for L against power for different geomagnetic activity lev-

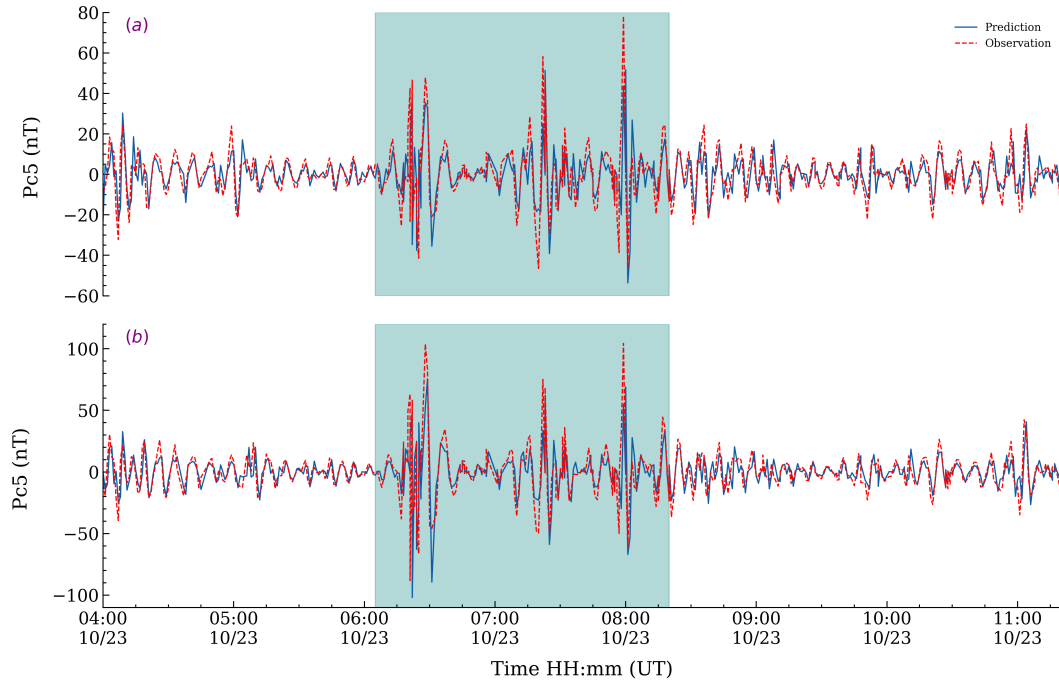


Figure 13. The prediction and Observation of Pc5 pulsations in the Svalbard network. Where panels (a), and (b) are model test results from LYR and HOR observatories in 1996.

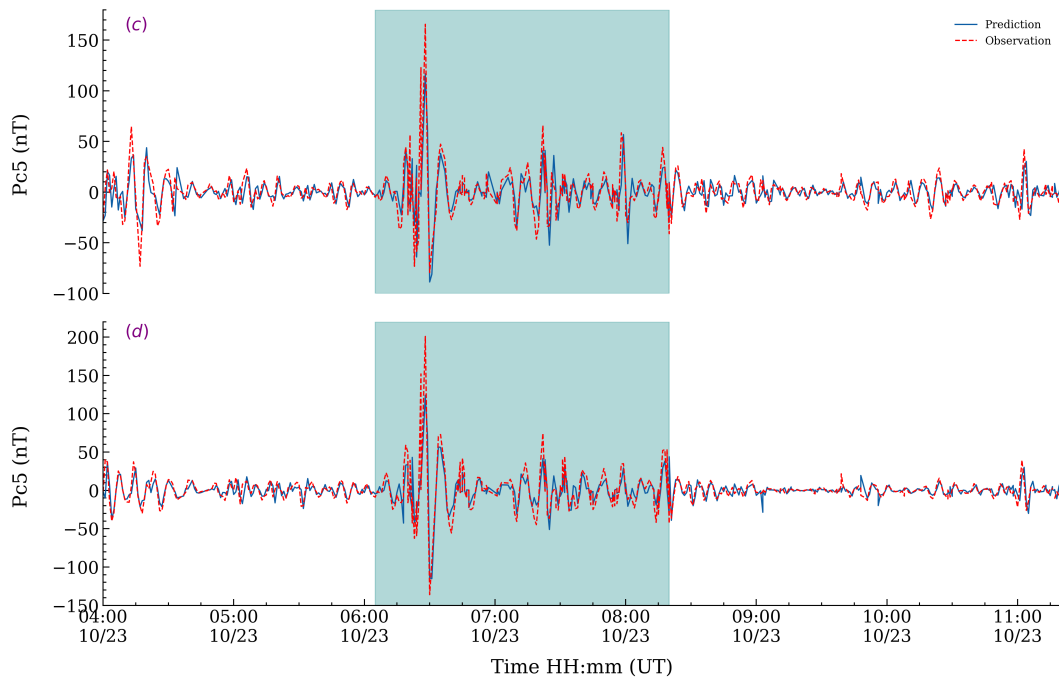


Figure 14. The prediction and Observation of Pc5 pulsations in the Svalbard network. Where panels (c), and (d) are model test results from HOP, and BJN observatories in 1996.

479 els, which can easily be used in the global radiation belt models. Recently, Dimitrakoudis
 480 et al. (2015) reported that the Kp-index is the single best parameter to investigate the

481 statistical ULF wave power driving radial diffusion. Therefore, we utilized the same con-
 482 cept in choosing Kp-index as the qualifying validation model for our model outcome. Fig-
 483 ure 15 illustrates the validation results of Pc5 prediction outcomes on testing deployment
 484 with Kp indices for two solar cycles, 23 and 24. Amongst the 8-year test datasets, 1996
 485 emerged as the most active year while 2009 was the least. There was a good correlation
 486 between Kp-index and model predictions. This implies that the ML model had good per-
 formance. It was observed that the number of occurrences of Pc5 pulsation was high in

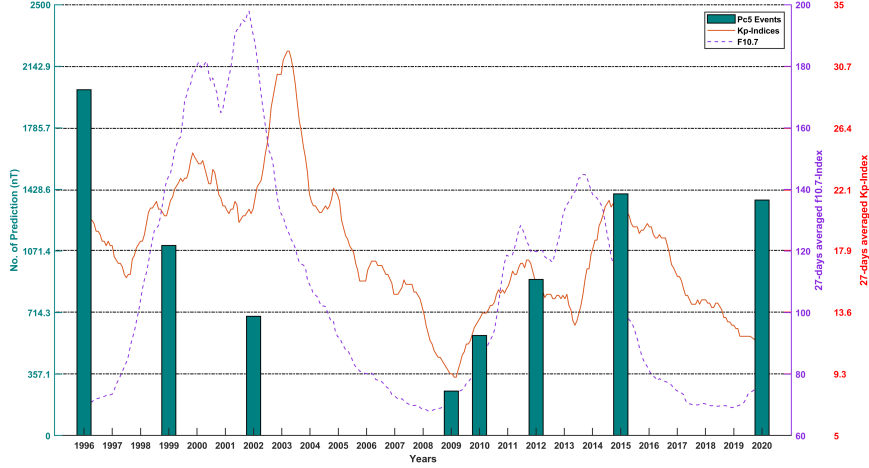


Figure 15. Kp profile index with the selected number year number of Pc5 prediction events correlation for two solar cycles. The bar graphs indicate the number of predicted Pc5 events for 8 different years of model testing while the line plot is 27days averaged Kp indices for 25 years

487 the low solar activity. The same results are reflected in the prediction of Pc5 undulations.
 488 In the ascending phase of solar cycle 23 indicated by the F10.7 index in Figure 15 shows
 489 a decreasing trend in the number of Pc5 predictions. In contrast, solar cycle 24 provided
 490 an interesting observation contrary to that of solar cycle 23. Whereby the minimum phase
 491 for solar cycle 23 recorded 264 and ascending phase 2022 Pc5 prediction events while solar
 492 cycle 24 was 1382 events in 2020. It can be noted that in both cycles there was a high
 493 geomagnetic activity in solar cycle 23 ascending phase indicated by Kp-index and low
 494 solar activity. On the other hand, the solar cycle 23 and 24 minimum phase had both
 495 minimum solar and geomagnetic activities. In relevance to machine model performance
 496 on the test set. Overall, there was good coherence between the solar activity models (F10.7),
 497 Pc5 predictions, and geomagnetic activity models (Kp).
 498

499 5 Conclusion

500 In the current study, we have developed a machine learning model based on the NARX
 501 recurrent neural network to predict time series ground Pc5 pulsations in the Svalbard
 502 network using solar wind parameters. The model was trained with 17 years of datasets
 503 and tested on 8 years of data shuffled from solar cycles 23 and 24. After the training phase,
 504 the model’s internal evaluation yielded $R=0.75$ and $MSE=11.90 \text{ nT}^2$. It was also deployed
 505 in various geomagnetic conditions, solar activities, and finally in different locations in
 506 the Svalbard network. Studies on the St.patrick storm day on March 17, 2015, demon-
 507 strated good coherence between the observation and the prediction. Consequently, the
 508 ML model showed also good performance in the four other ground observatories on the

509 minor storm of October 23rd, 1996. Therefore, these were in agreement with the other
 510 studies on this region, given that Pc5 waves recorded in one observatory are simultane-
 511 ously observed in other stations (Omondi et al., 2023). On the contrary, given that the
 512 geomagnetic Pulsations monitored in the auroral oval are the same in terms of frequency
 513 information but unique in terms of amplitude and phase. Therefore, presenting complex-
 514 ities in data. Provided the model was trained with different data from one observatory
 515 and deployed in different observatories and still able to give excellent performance de-
 516 spite uncertainties in data. This demonstrates the power of machine learning in pattern
 517 recognition from complex and large volumes of data. For example, the HOP station pro-
 518 duced a higher number of predictions compared to other stations. It also had maximum
 519 amplitude predicted Pc5 pulsations with a decaying amplitude in other stations in high
 520 and low magnetic latitudes from HOP. Given that, there were good results despite data
 521 complexity in the year 2020 and 1996. Comparing the observation in Figure 15 with Fig-
 522 ure 17 in Omondi et al. (2023) studies, there is a common trend in solar 23 and 24 pre-
 523 dictions except in 2020. Thus, in the current study, 2020 became an outlier performing
 524 average with $R=0.57$. On the contrary, more predictions were observed deviating from
 525 the trend with other observations. We conclude that the model performance was robust
 526 and fit for deployment in space weather forecasting. This was the first ground-based Pc5
 527 prediction in the auroral zone using a machine-learning technique using solar wind pa-
 528 rameters. Overall, the ML model yielded good results and useful tool in the magneto-
 529 spheric community. Therefore, to improve the model's performance, future work would
 530 focus on probabilistic prediction and forecasting.

531 Data Accessibility Statement

532 The magnetic field observations used in this study were obtained from the Sval-
 533 bard network in the International Monitor for Auroral Geomagnetic Effects (IMAGE)
 534 was accessed through (<https://space.fmi.fi/image/www/index.php>). The Solar wind
 535 parameters data utilized for prediction were retrieved from Omniweb, through ([https://](https://omniweb.gsfc.nasa.gov/)
 536 omniweb.gsfc.nasa.gov/). The Kp and F10.7 data were also obtained from the NASA
 537 data center via OmniWeb.

538 Acknowledgement

539 The corresponding Author extends his sincere gratitude to Egypt Japan Univer-
 540 sity of Science and Technology (E-JUST) and JICA cooperation for supporting the E-
 541 JUST International Alumni program which facilitated his visit and conducted the cur-
 542 rent study with the magnetospheric group of SERL-Lab. We give much appreciation to
 543 NASA for openly providing data through Omniweb (<http://cdaweb.gsfc.nasa.gov>). We
 544 give special appreciation to the institutions maintaining the IMAGE Magnetometer Ar-
 545 ray and providing data for science: Tromsø Geophysical Observatory of UiT the Arc-
 546 tic University of Norway(Norway), Finnish Meteorological Institute (Finland), GFZ Ger-
 547 man Research Centre for Geosciences (Germany), Institute of Geophysics Polish Academy
 548 of Sciences (Poland), Swedish Institute of Space Physics (Sweden), Geological Survey
 549 of Sweden(Sweden), Polar Geophysical Institute (Russia) and Sodankyla Geophysical
 550 Observatory of the University of Oulu (Finland).

551 References

- 552 Ayala Solares, J. R., Wei, H.-L., Boynton, R. J., Walker, S. N., & Billings, S. A.
 553 (2016). Modeling and prediction of global magnetic disturbance in near-earth
 554 space: A case study for kp index using narx models. *Space Weather*, *14*(10),
 555 899–916.
 556 Baddeley, L., Yeoman, T., McWilliams, K., & Wright, D. (2007). Global pc5
 557 wave activity observed using superdarn radars and ground magnetometers

- 558 during an extended period of northward imf. *Planetary and Space Science*,
 559 55(6), 792-808. (Ultra-Low Frequency Waves in the Magnetosphere) doi:
 560 <https://doi.org/10.1016/j.pss.2006.01.009>
- 561 Balikhin, M. A., Boynton, R. J., Walker, S. N., Borovsky, J. E., Billings, S. A., &
 562 Wei, H. L. (2011). Using the narmax approach to model the evolution of en-
 563 ergetic electrons fluxes at geostationary orbit. *Geophysical Research Letters*,
 564 38(18). doi: <https://doi.org/10.1029/2011GL048980>
- 565 Bhaskar, A., & Vichare, G. (2019). Forecasting of symh and asyh indices for geo-
 566 magnetic storms of solar cycle 24 including st. patrick's day, 2015 storm using
 567 narx neural network. *Journal of Space Weather and Space Climate*, 9, A12.
- 568 Billings, S. A. (2013). *Nonlinear system identification: Narmax methods in the time,*
 569 *frequency, and spatio-temporal domains.* John Wiley & Sons. doi: [https://doi](https://doi.org/10.1002/9781118535561)
 570 [.org/10.1002/9781118535561](https://doi.org/10.1002/9781118535561)
- 571 Boynton, R. J., Balikhin, M. A., Billings, S. A., Wei, H. L., & Ganushkina, N.
 572 (2011). Using the narmax ols-err algorithm to obtain the most influential
 573 coupling functions that affect the evolution of the magnetosphere. *Journal of*
 574 *Geophysical Research: Space Physics*, 116(A5). doi: [https://doi.org/10.1029/](https://doi.org/10.1029/2010JA015505)
 575 [2010JA015505](https://doi.org/10.1029/2010JA015505)
- 576 Cai, L., Ma, S., Cai, H., Zhou, Y., & Liu, R. (2009). Prediction of sym-h index by
 577 narx neural network from imf and solar wind data. *Science in China Series E:*
 578 *Technological Sciences*, 52, 2877–2885.
- 579 Chandorkar, M., Camporeale, E., & Wing, S. (2017). Probabilistic forecasting of the
 580 disturbance storm time index: An autoregressive gaussian process approach.
 581 *Space Weather*, 15(8), 1004–1019.
- 582 Chen, L., & Hasegawa, A. (1974). A theory of long-period magnetic pulsations:
 583 1. steady state excitation of field line resonance. *Journal of Geophysical*
 584 *Research (1896-1977)*, 79(7), 1024-1032. doi: [https://doi.org/10.1029/](https://doi.org/10.1029/JA079i007p01024)
 585 [JA079i007p01024](https://doi.org/10.1029/JA079i007p01024)
- 586 Dimitrakoudis, S., Mann, I. R., Balasis, G., Papadimitriou, C., Anastasiadis, A.,
 587 & Daglis, I. A. (2015). Accurately specifying storm-time ulf wave radial
 588 diffusion in the radiation belts. *Geophysical Research Letters*, 42(14), 5711-
 589 5718. Retrieved from [https://agupubs.onlinelibrary.wiley.com/doi/abs/](https://agupubs.onlinelibrary.wiley.com/doi/abs/10.1002/2015GL064707)
 590 [10.1002/2015GL064707](https://doi.org/10.1002/2015GL064707) doi: <https://doi.org/10.1002/2015GL064707>
- 591 Dungey, J. W. (1961). Interplanetary magnetic field and the auroral zones. *Physical*
 592 *Review Letters*, 6(2), 47.
- 593 Eastwood, J., Nakamura, R., Turc, L., Mejnertsen, L., & Hesse, M. (2017). The sci-
 594 entific foundations of forecasting magnetospheric space weather. *Space Science*
 595 *Reviews*, 212, 1221–1252.
- 596 Gholipour, A., Lucas, C., & Araabi, B. N. (2004). Black box modeling of magneto-
 597 spheric dynamics to forecast geomagnetic activity. *Space Weather*, 2(7).
- 598 Gu, Y., Wei, H.-L., Boynton, R. J., Walker, S. N., & Balikhin, M. A. (2019). Sys-
 599 tem identification and data-driven forecasting of ae index and prediction un-
 600 certainty analysis using a new cloud-narx model. *Journal of Geophysical*
 601 *Research: Space Physics*, 124(1), 248-263. doi: [https://doi.org/10.1029/](https://doi.org/10.1029/2018JA025957)
 602 [2018JA025957](https://doi.org/10.1029/2018JA025957)
- 603 Harrold, B. G., & Samson, J. C. (1992). Standing ulf modes of the magnetosphere:
 604 A theory. *Geophysical Research Letters*, 19(18), 1811-1814. doi: [https://doi](https://doi.org/10.1029/92GL01802)
 605 [.org/10.1029/92GL01802](https://doi.org/10.1029/92GL01802)
- 606 Kamide, Y., Baumjohann, W., Daglis, I. A., Gonzalez, W. D., Grande, M., Jose-
 607 lyn, J. A., ... Vasyliunas, V. M. (1998). Current understanding of magnetic
 608 storms: Storm-substorm relationships. *Journal of Geophysical Research: Space*
 609 *Physics*, 103(A8), 17705-17728. doi: <https://doi.org/10.1029/98JA01426>
- 610 Kessel, R., Mann, I., Fung, S., Milling, D., & O'Connell, N. (2004). Correlation
 611 of pc5 wave power inside and outside the magnetosphere during high speed
 612 streams. In *Annales geophysicae* (Vol. 22, pp. 629–641).

- 613 Kivelson, M. G., Etcheto, J., & Trotignon, J. G. (1984). Global compressional os-
 614 cillations of the terrestrial magnetosphere: The evidence and a model. *Journal*
 615 *of Geophysical Research: Space Physics*, 89(A11), 9851-9856. doi: [https://doi](https://doi.org/10.1029/JA089iA11p09851)
 616 [.org/10.1029/JA089iA11p09851](https://doi.org/10.1029/JA089iA11p09851)
- 617 Kleimenova, N., Kozyreva, O., Vlasov, A., Uspensky, M., & Kauristie, K. (2010).
 618 Afternoon pc5 geomagnetic pulsations on the earth's surface and in the iono-
 619 sphere (stare radars). *Geomagnetism and Aeronomy*, 50, 329-338. doi:
 620 <https://doi.org/10.1134/S0016793210030072>
- 621 Lee, E. A., Mann, I. R., Loto'aniu, T. M., & Dent, Z. C. (2007). Global pc5 pul-
 622 sations observed at unusually low l during the great magnetic storm of 24
 623 march 1991. *Journal of Geophysical Research: Space Physics*, 112(A5). doi:
 624 <https://doi.org/10.1029/2006JA011872>
- 625 Li, X., Temerin, M., Baker, D. N., & Reeves, G. D. (2011). Behavior of mev elec-
 626 trons at geosynchronous orbit during last two solar cycles. *Journal of Geo-*
 627 *physical Research: Space Physics*, 116(A11). doi: [https://doi.org/10.1029/](https://doi.org/10.1029/2011JA016934)
 628 [2011JA016934](https://doi.org/10.1029/2011JA016934)
- 629 Mann, I., O'Brien, T., & Milling, D. (2004). Correlations between ulf wave power,
 630 solar wind speed, and relativistic electron flux in the magnetosphere: solar
 631 cycle dependence. *Journal of Atmospheric and Solar-Terrestrial Physics*,
 632 66(2), 187-198. (Space Weather in the Declining Phase of the Solar Cycle) doi:
 633 <https://doi.org/10.1016/j.jastp.2003.10.002>
- 634 Mathie, R., & Mann, I. (2001). On the solar wind control of pc5 ulf pulsation
 635 power at mid-latitudes: Implications for mev electron acceleration in the outer
 636 radiation belt. *Journal of Geophysical Research: Space Physics*, 106(A12),
 637 29783-29796.
- 638 McCulloch, W. S., & Pitts, W. (1943). A logical calculus of the ideas immanent in
 639 nervous activity. *The bulletin of mathematical biophysics*, 5, 115-133. doi:
 640 <https://doi.org/10.1007/BF02478259>
- 641 Omondi, S., Yoshikawa, A., Zahra, W. K., Fathy, I., & Mahrous, A. (2023). Auto-
 642 matic detection of auroral pc5 geomagnetic pulsation using machine learning
 643 approach guided with discrete wavelet transform. *Advances in Space Research*,
 644 72(3), 866-883. doi: <https://doi.org/10.1016/j.asr.2022.06.063>.
- 645 Ozeke, L. G., Mann, I. R., Murphy, K. R., Jonathan Rae, I., & Milling, D. K.
 646 (2014). Analytic expressions for ulf wave radiation belt radial diffusion co-
 647 efficients. *Journal of Geophysical Research: Space Physics*, 119(3), 1587-1605.
 648 doi: <https://doi.org/10.1002/2013JA019204>
- 649 Pahud, D., Rae, I., Mann, I., Murphy, K., & Amalraj, V. (2009). Ground-based pc5
 650 ulf wave power: Solar wind speed and mlt dependence. *Journal of Atmospheric*
 651 *and Solar-Terrestrial Physics*, 71(10-11), 1082-1092.
- 652 Pilipenko, V., Watermann, J., Popov, V., & Papitashvili, V. (2001). Relationship
 653 between auroral electrojet and pc5 ulf waves. *Journal of Atmospheric and*
 654 *Solar-Terrestrial Physics*, 63(14), 1545-1557. doi: [https://doi.org/10.1016/](https://doi.org/10.1016/S1364-6826(01)00031-1)
 655 [S1364-6826\(01\)00031-1](https://doi.org/10.1016/S1364-6826(01)00031-1)
- 656 Poulton, M. M. (2002). Neural networks as an intelligence amplification tool: A
 657 review of applications. *Geophysics*, 67(3), 979-993. doi: [https://doi.org/10](https://doi.org/10.1190/1.1484539)
 658 [.1190/1.1484539](https://doi.org/10.1190/1.1484539).
- 659 Rae, I. J., Mann, I. R., Murphy, K. R., Ozeke, L. G., Milling, D. K., Chan, A. A.,
 660 ... Honary, F. (2012). Ground-based magnetometer determination of
 661 in situ pc4-5 ulf electric field wave spectra as a function of solar wind
 662 speed. *Journal of Geophysical Research: Space Physics*, 117(A4). doi:
 663 <https://doi.org/10.1029/2011JA017335>
- 664 Rostoker, G., & Lam, H.-L. (1978). A generation mechanism for pc 5 micropulsa-
 665 tions in the morning sector. *Planetary and Space Science*, 26(5), 493-505.
- 666 Samson, J., Cogger, L., & Pao, Q. (1996). Observations of field line resonances,
 667 auroral arcs, and auroral vortex structures. *Journal of Geophysical Research:*

- 668 *Space Physics*, 101(A8), 17373–17383.
- 669 Samson, J., Jacobs, J. A., & Rostoker, G. (1971). Latitude-dependent character-
670 istics of long-period geomagnetic micropulsations. *Journal of Geophysical Re-*
671 *search (1896-1977)*, 76(16), 3675–3683.
- 672 Southwood, D. (1974). Some features of field line resonances in the magne-
673 tosphere. *Planetary and Space Science*, 22(3), 483–491. Retrieved from
674 <https://www.sciencedirect.com/science/article/pii/0032063374900786>
675 doi: [https://doi.org/10.1016/0032-0633\(74\)90078-6](https://doi.org/10.1016/0032-0633(74)90078-6)
- 676 Uwamahoro, J., & Habarulema, J. B. (2014). Empirical modeling of the storm time
677 geomagnetic indices: a comparison between the local k and global kp indices.
678 *Earth, Planets and Space*, 66, 1–8.
- 679 Waters, C., Samson, J., & Donovan, E. (1995). The temporal variation of the fre-
680 quency of high latitude field line resonances. *Journal of Geophysical Research:*
681 *Space Physics*, 100(A5), 7987–7996.
- 682 Wei, H. L., Billings, S. A., & Balikhin, M. (2004). Prediction of the dst index us-
683 ing multiresolution wavelet models. *Journal of Geophysical Research: Space*
684 *Physics*, 109(A7). doi: <https://doi.org/10.1029/2003JA010332>
- 685 Weigel, R., Horton, W., Tajima, T., & Detman, T. (1999). Forecasting auroral
686 electrojet activity from solar wind input with neural networks. *Geophysical re-*
687 *search letters*, 26(10), 1353–1356.
- 688 Willisroft, L.-A., & Poole, A. W. (1996). Neural networks, fof2, sunspot number
689 and magnetic activity. *Geophysical research letters*, 23(24), 3659–3662.
- 690 Wintoft, P., Wik, M., Matzka, J., & Shprits, Y. (2017). Forecasting kp from solar
691 wind data: input parameter study using 3-hour averages and 3-hour range
692 values. *Journal of Space Weather and Space Climate*, 7, A29.
- 693 Wu, J.-G., & Lundstedt, H. (1996). Prediction of geomagnetic storms from solar
694 wind data using elman recurrent neural networks. *Geophysical research letters*,
695 23(4), 319–322.
- 696 Wu, J.-G., Lundstedt, H., Wintoft, P., & Detman, T. (1998). Neural network models
697 predicting the magnetospheric response to the 1997 january halo-cme event.
698 *Geophysical research letters*, 25(15), 3031–3034.
- 699 Ziesolleck, C. W. S., & McDiarmid, D. R. (1994). Auroral latitude pc 5 field line
700 resonances: Quantized frequencies, spatial characteristics, and diurnal varia-
701 tion. *Journal of Geophysical Research: Space Physics*, 99(A4), 5817–5830. doi:
702 <https://doi.org/10.1029/93JA02903>

Figure.

Input

Hidden

output

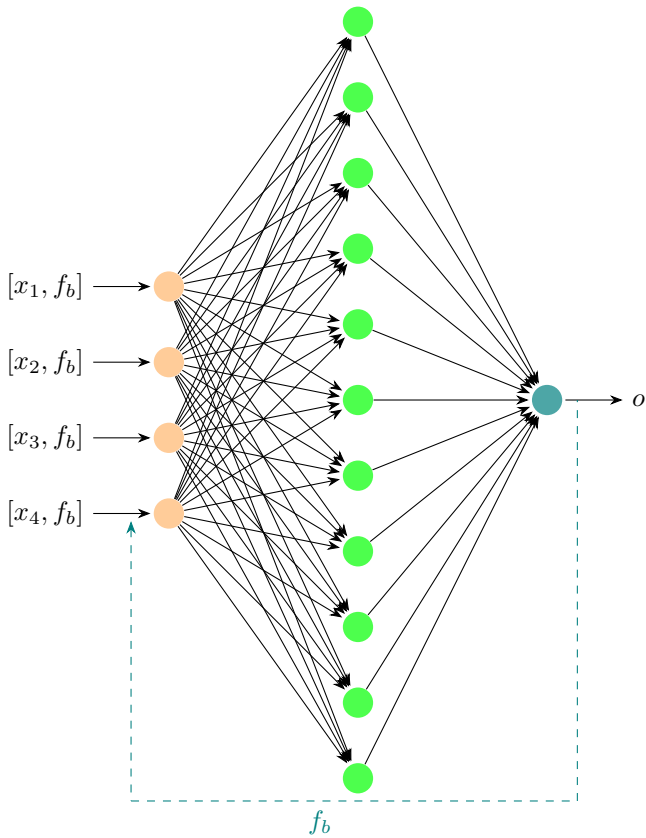


Figure.

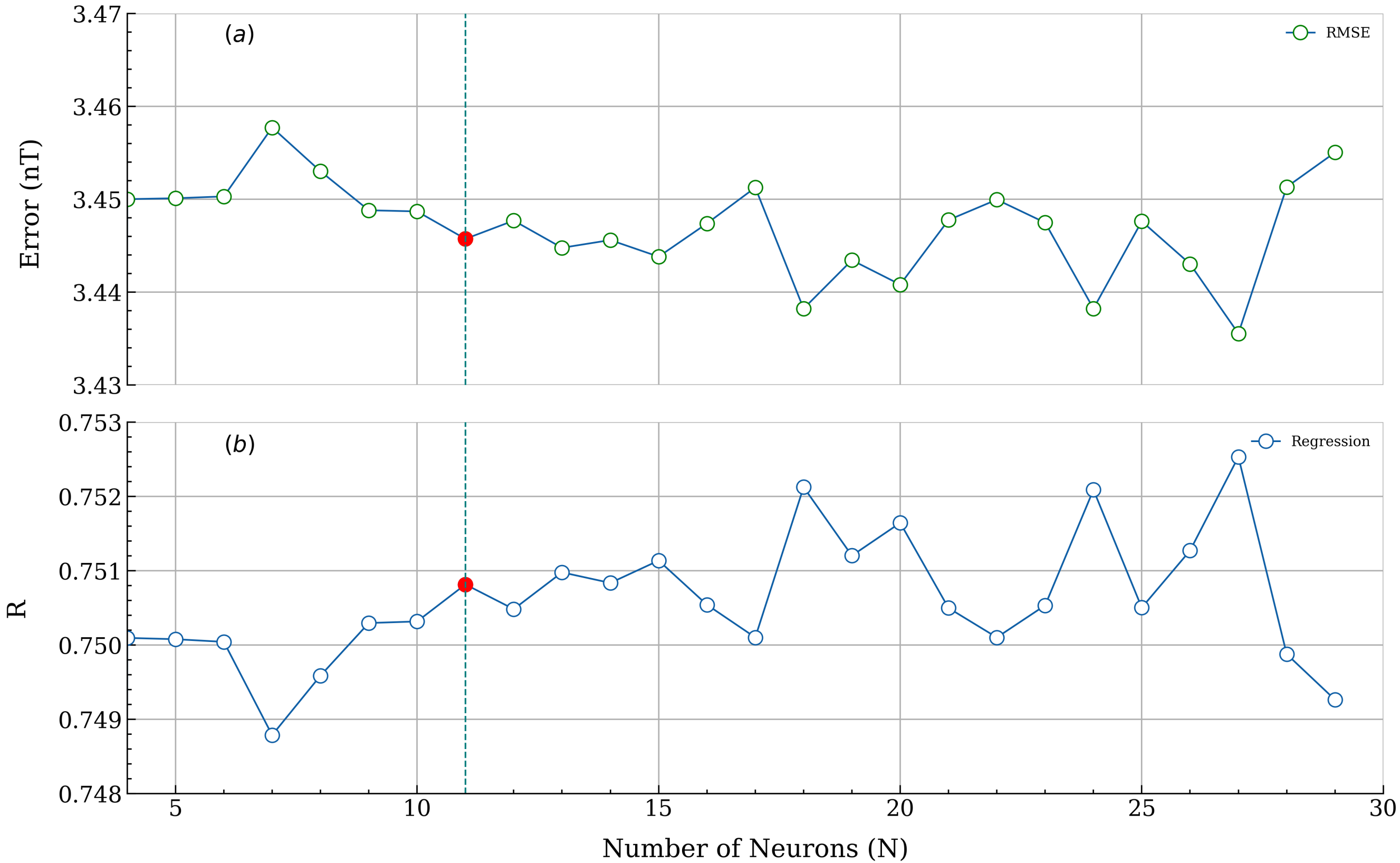


Figure.

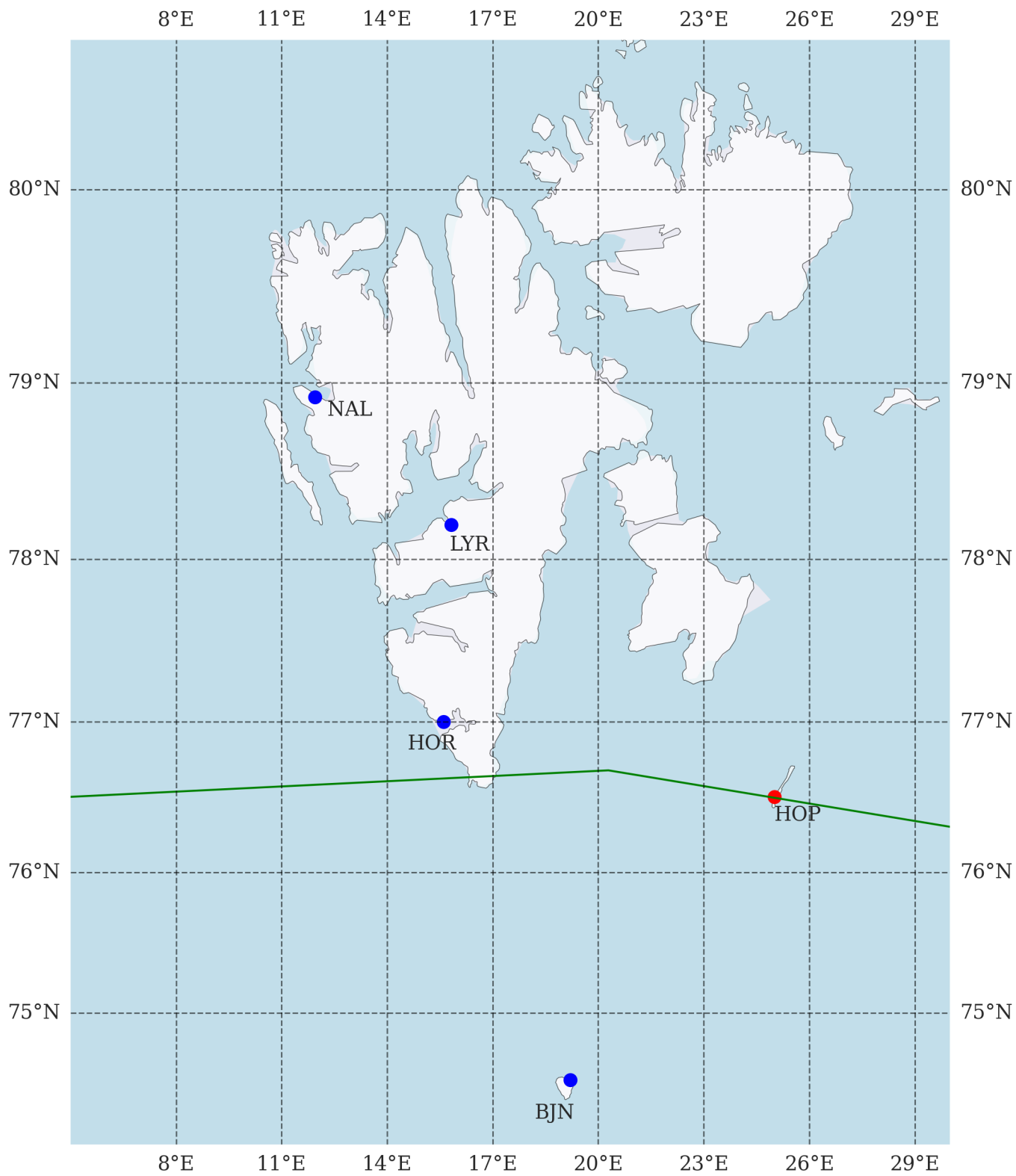


Figure.

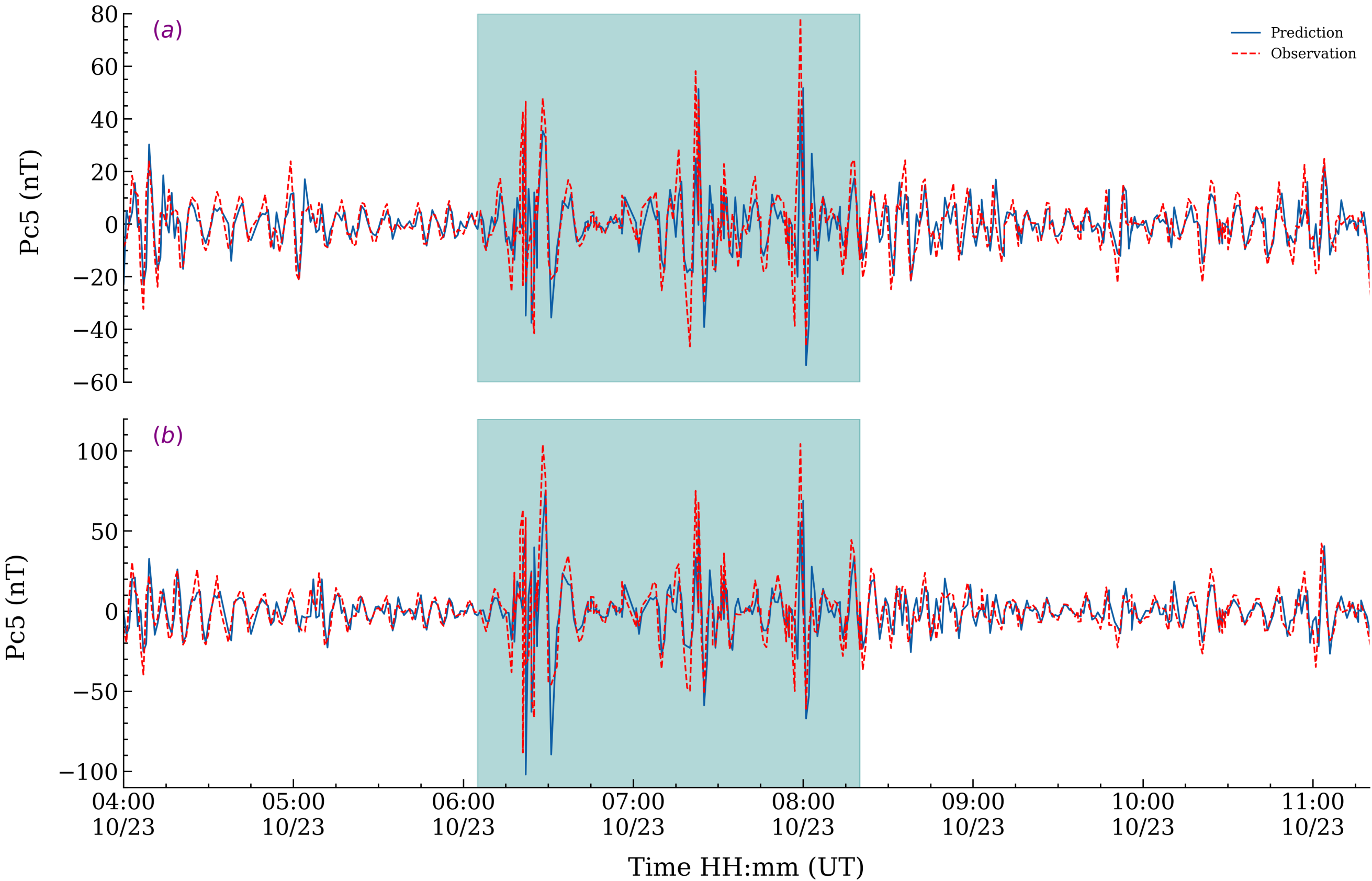


Figure.

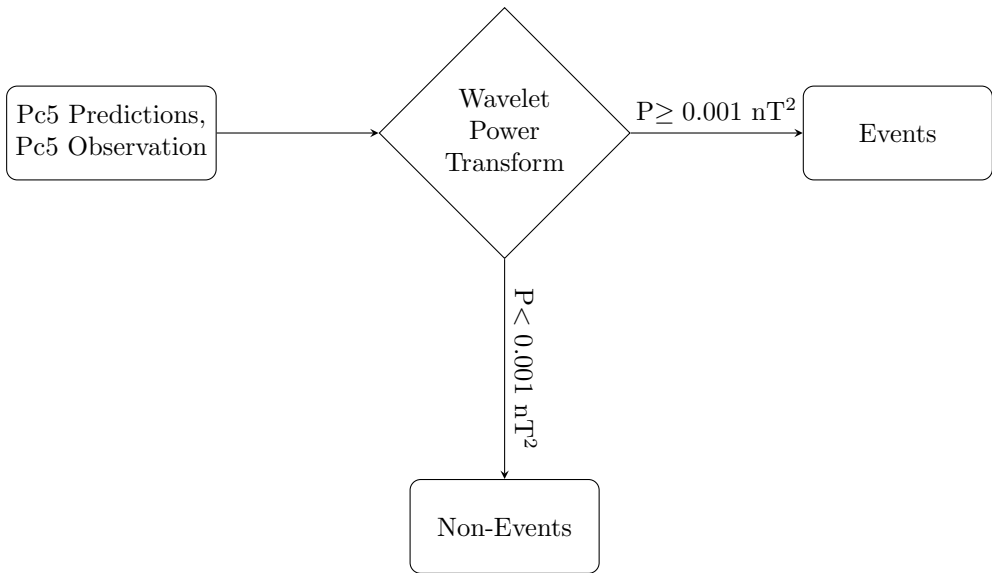


Figure.

Figure.

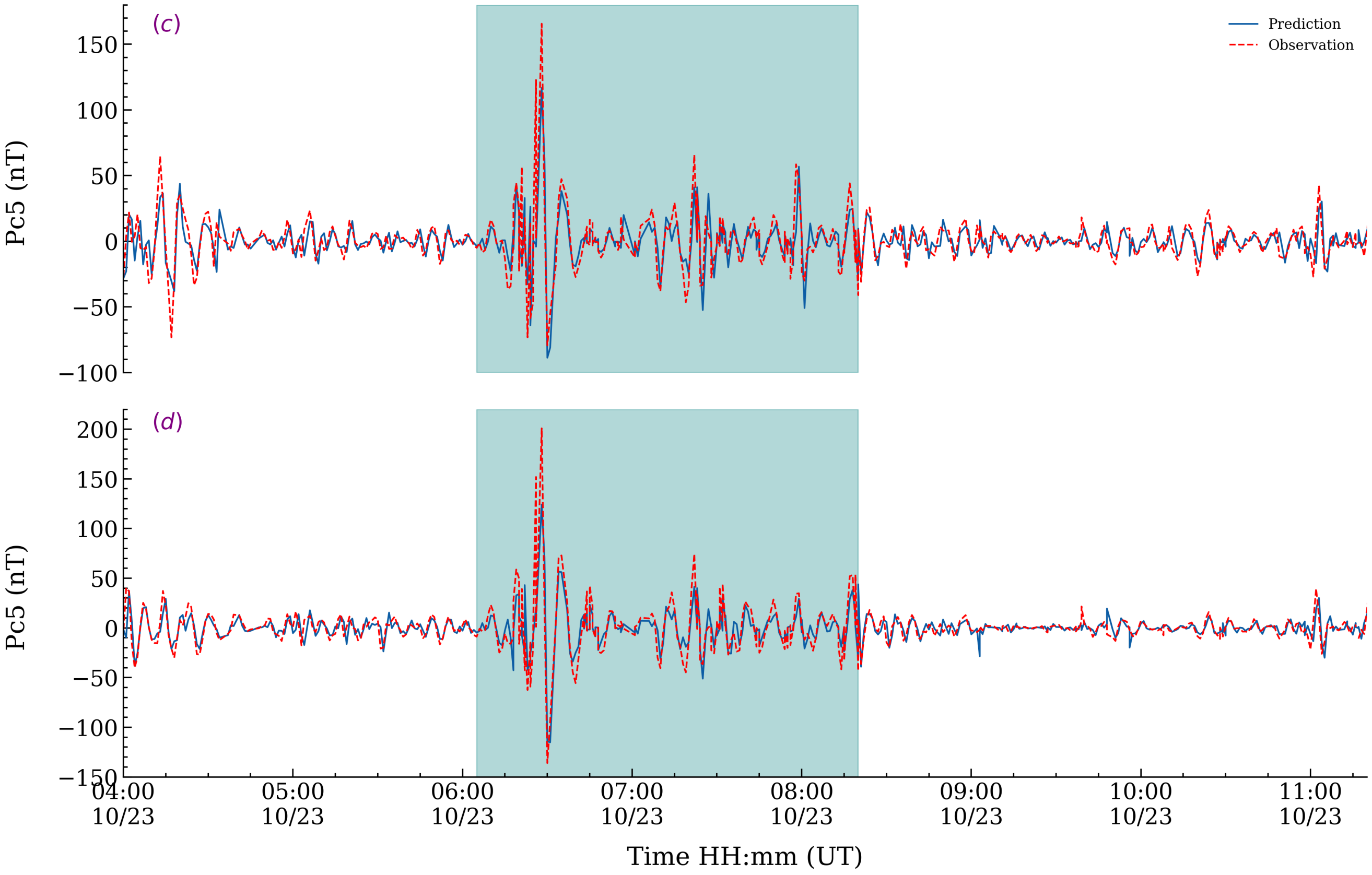


Figure.

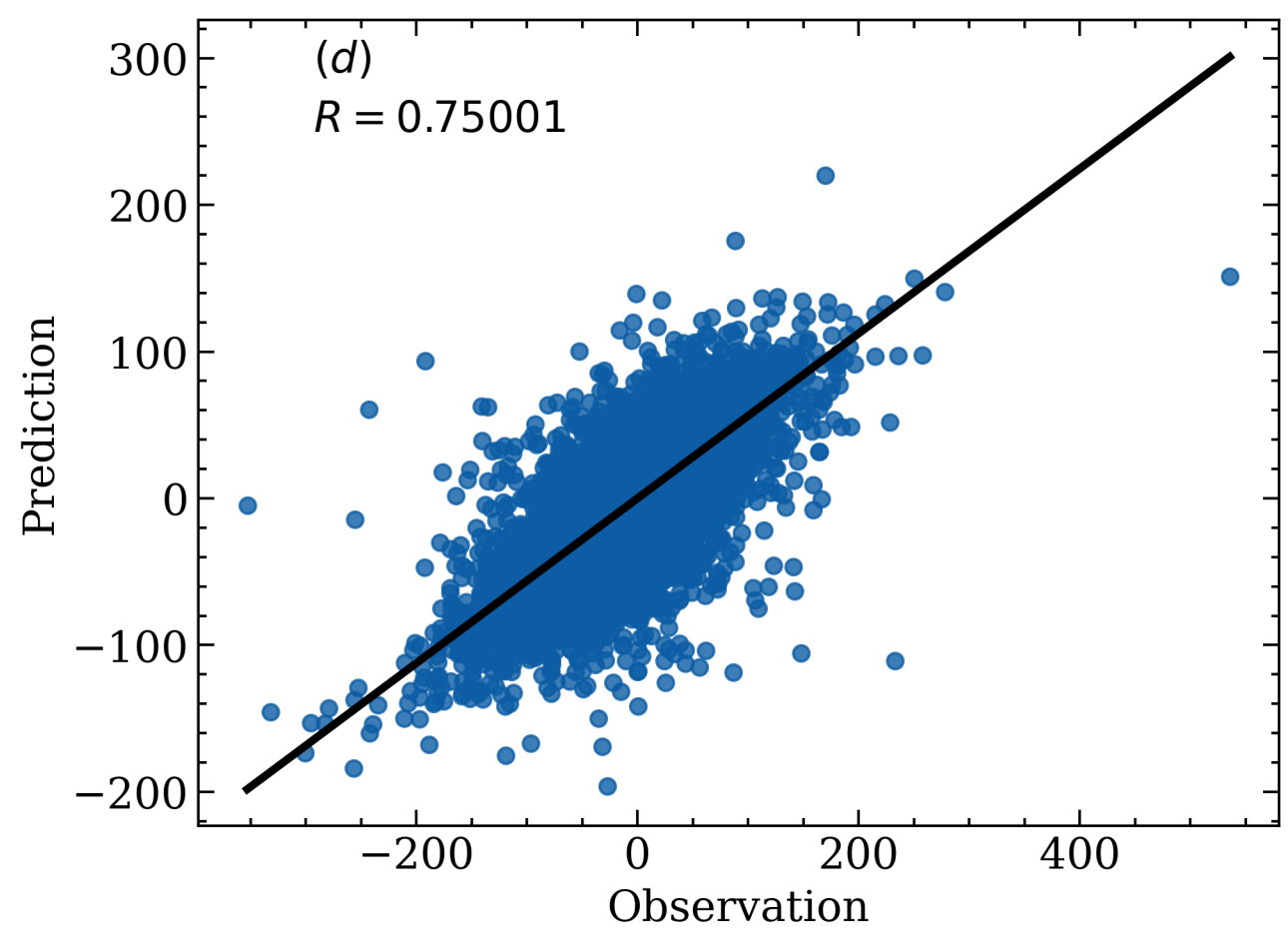
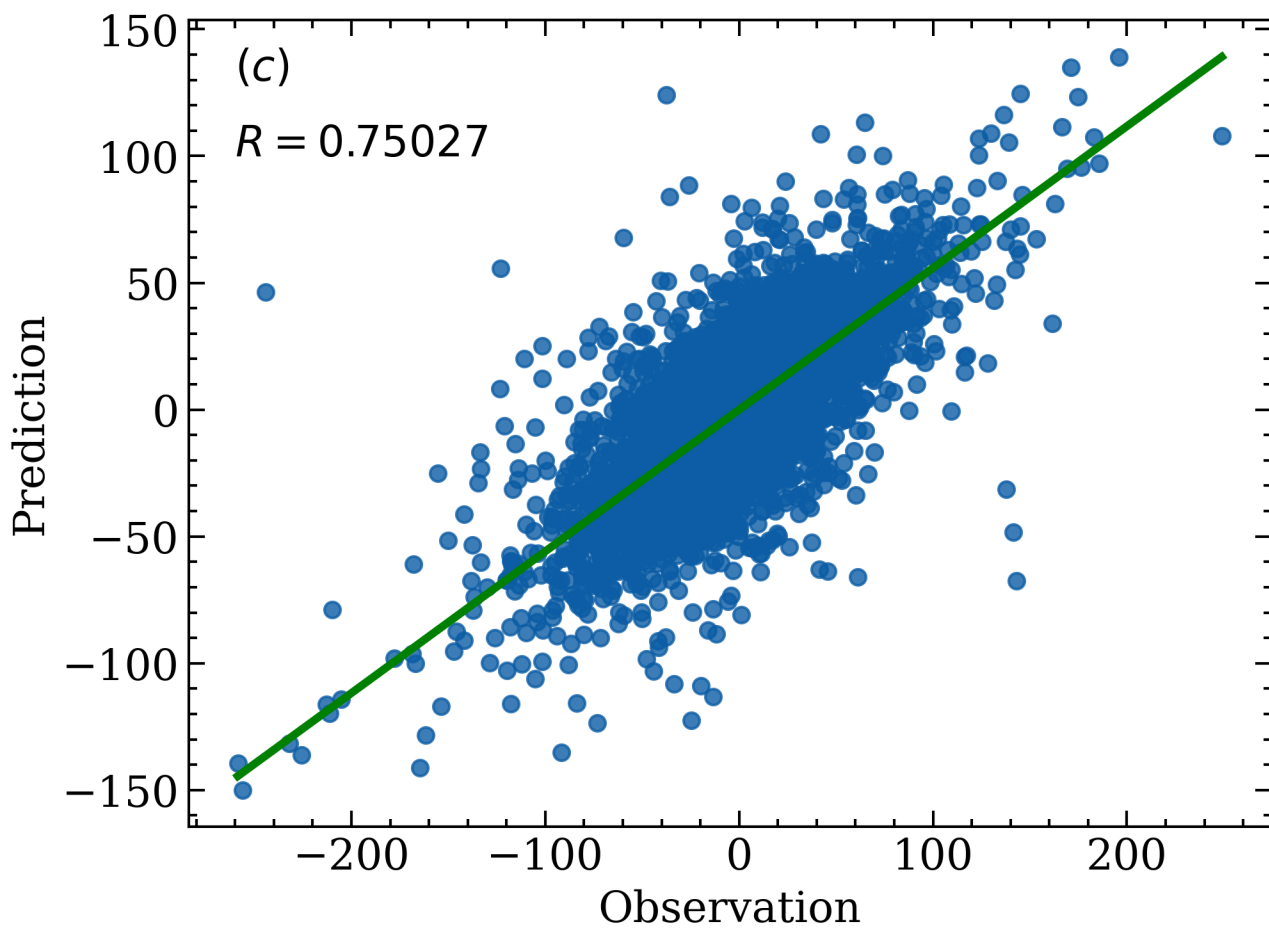
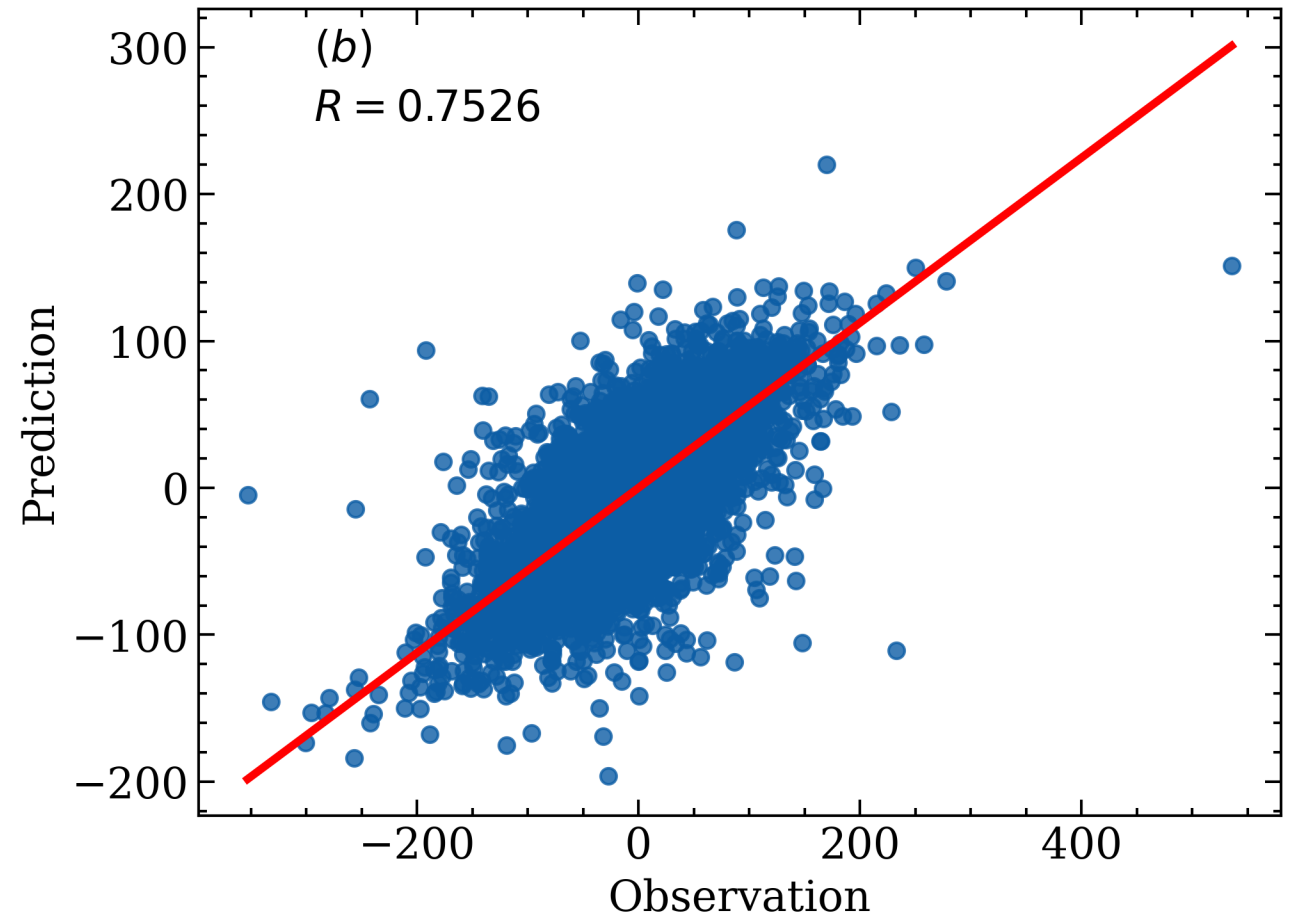
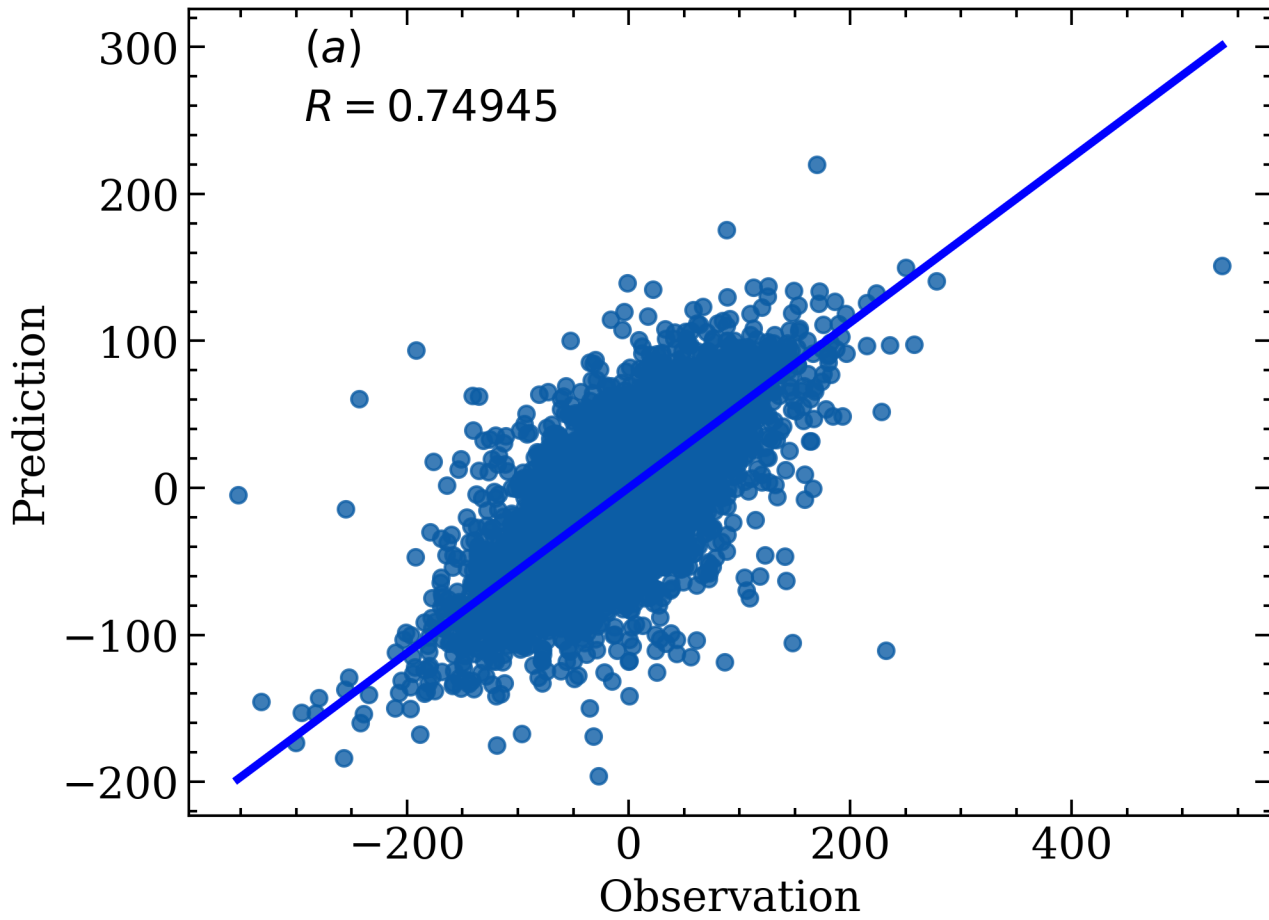


Figure.

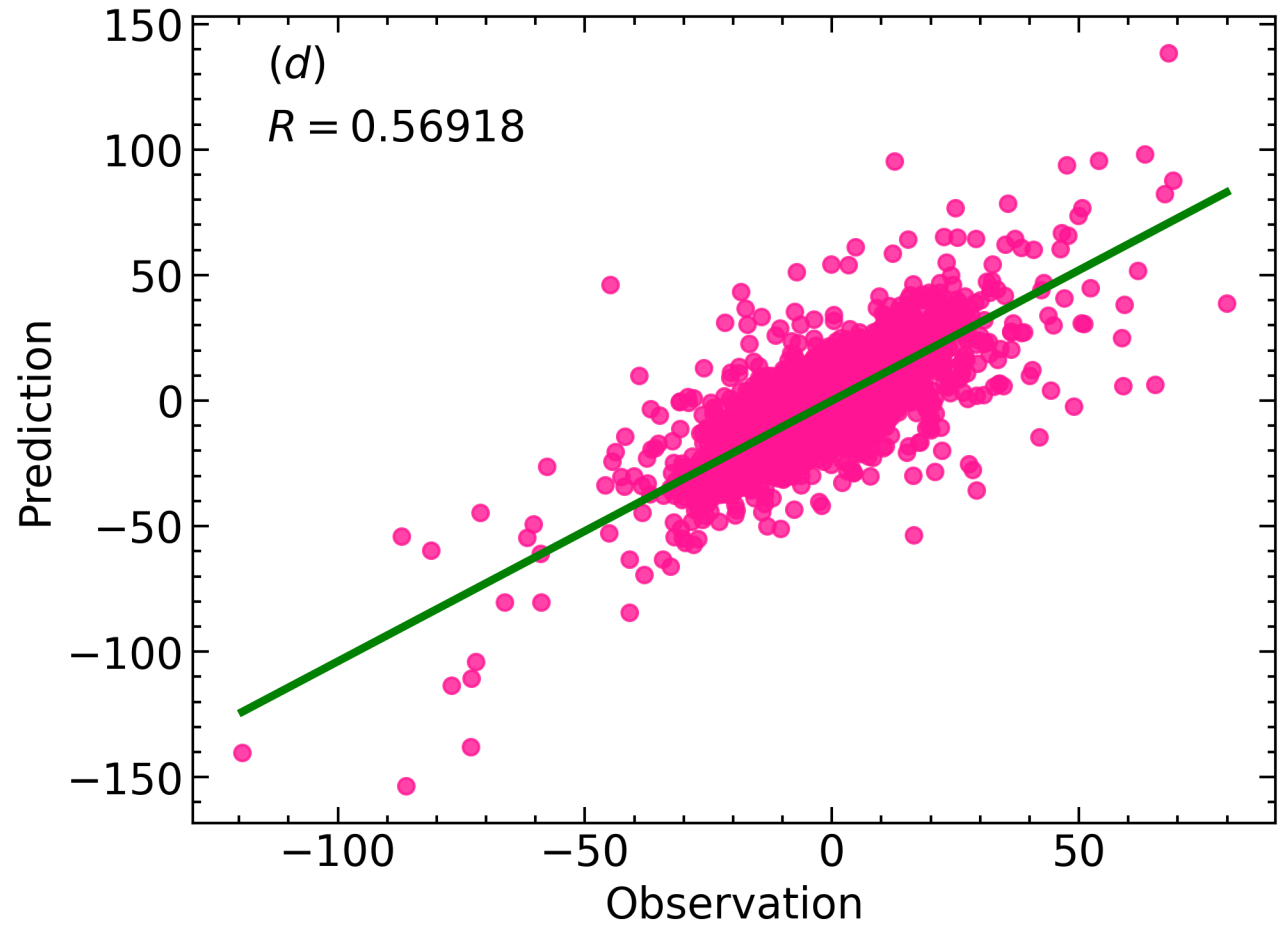
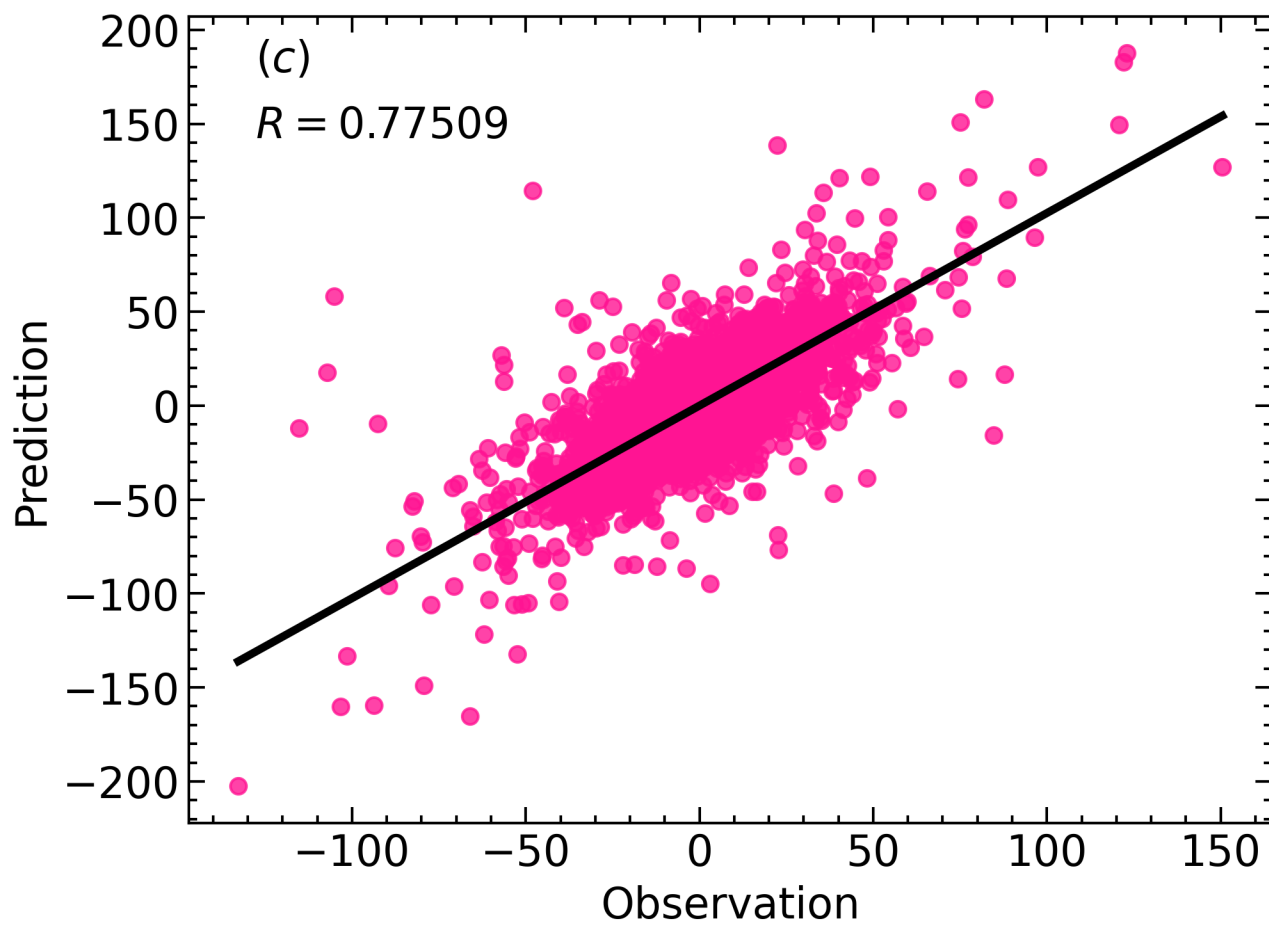
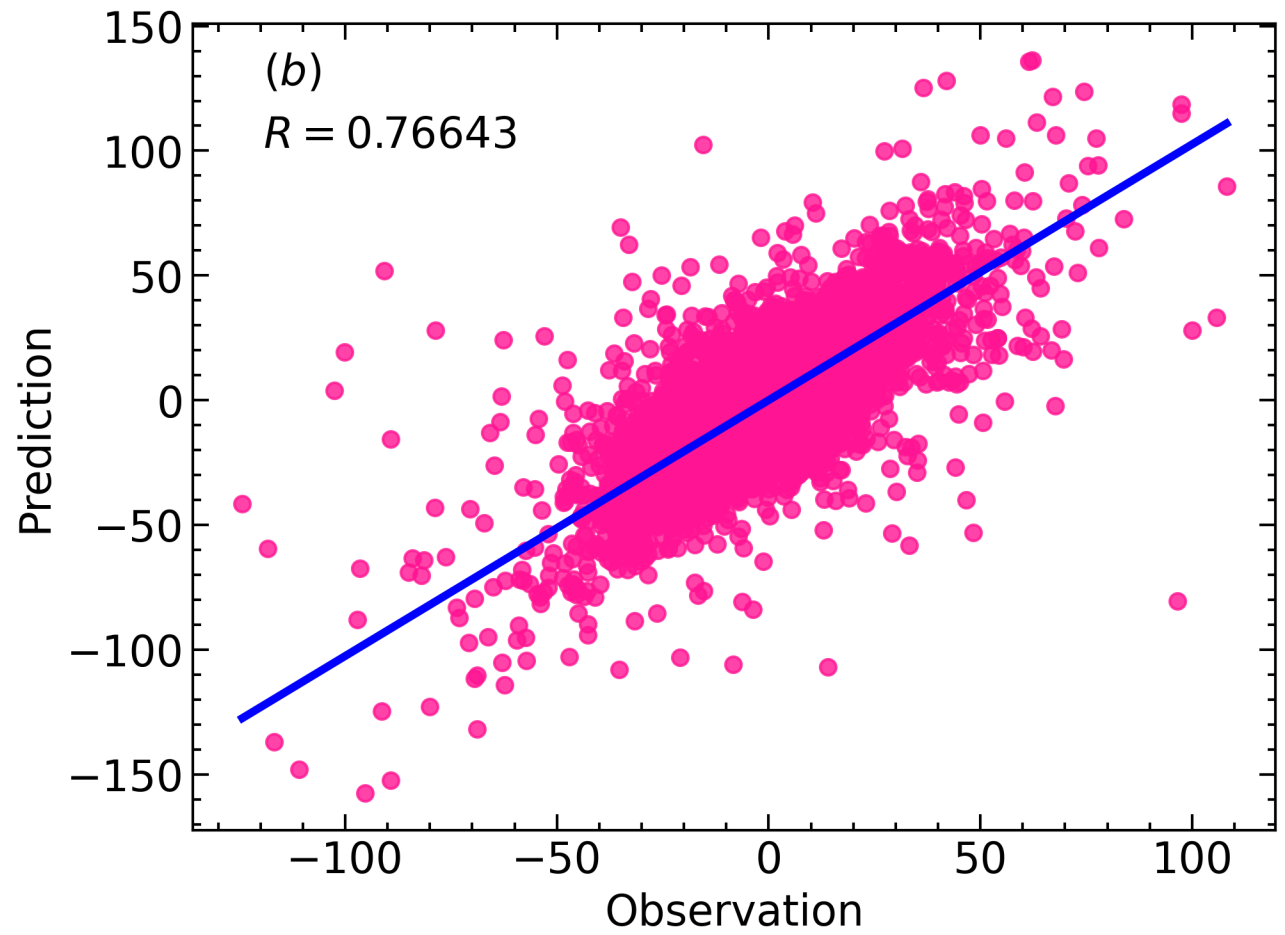
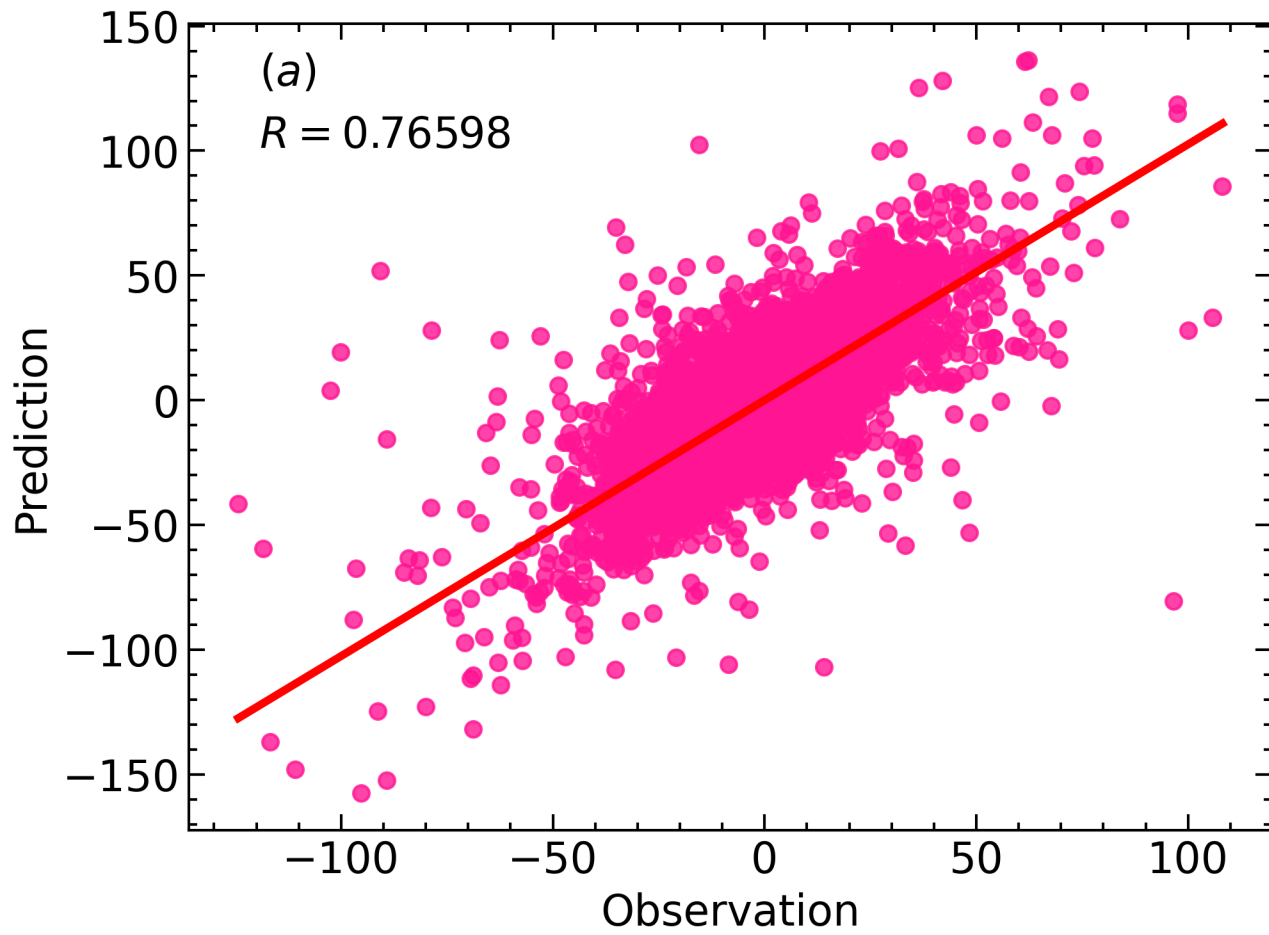


Figure.

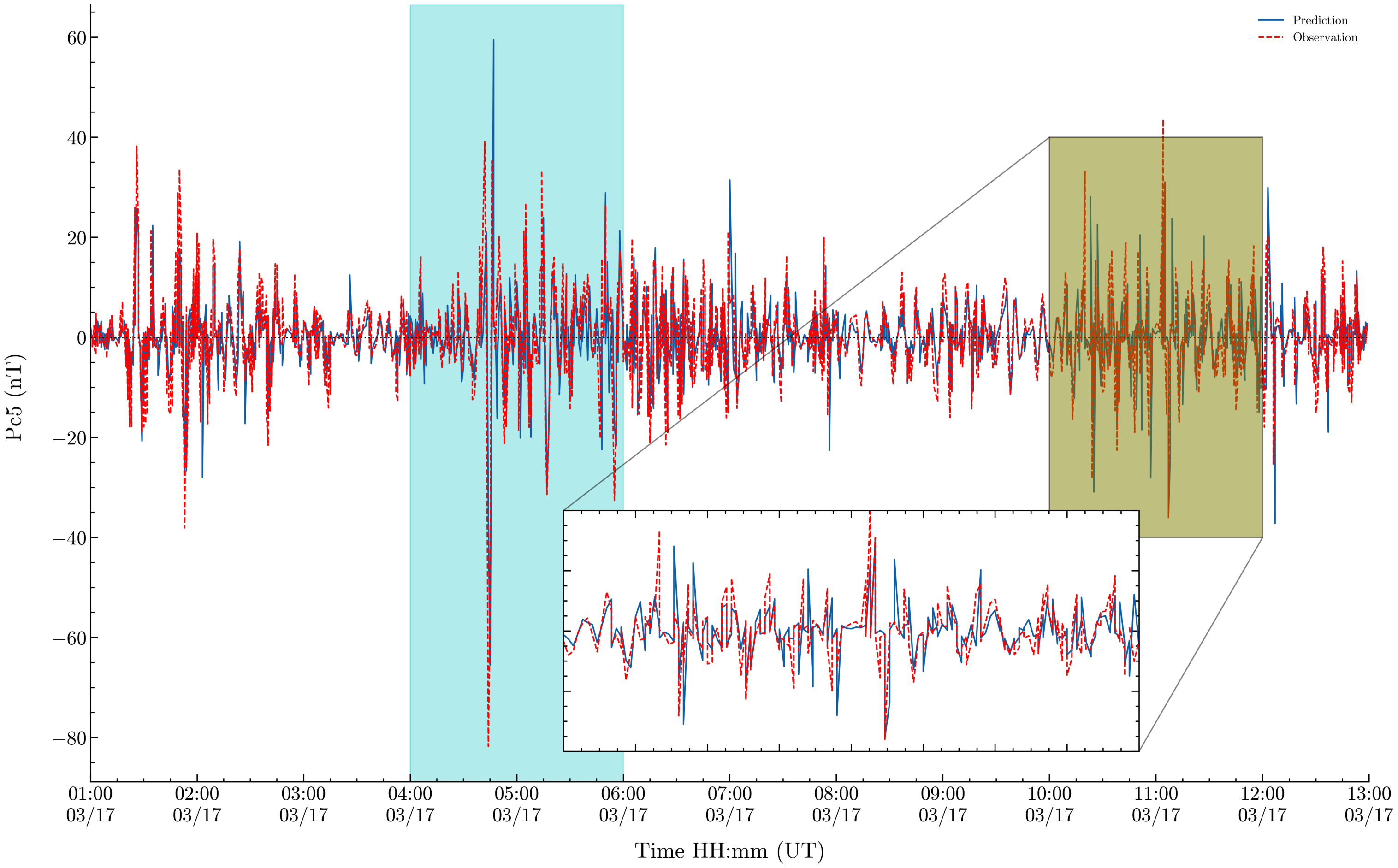


Figure.

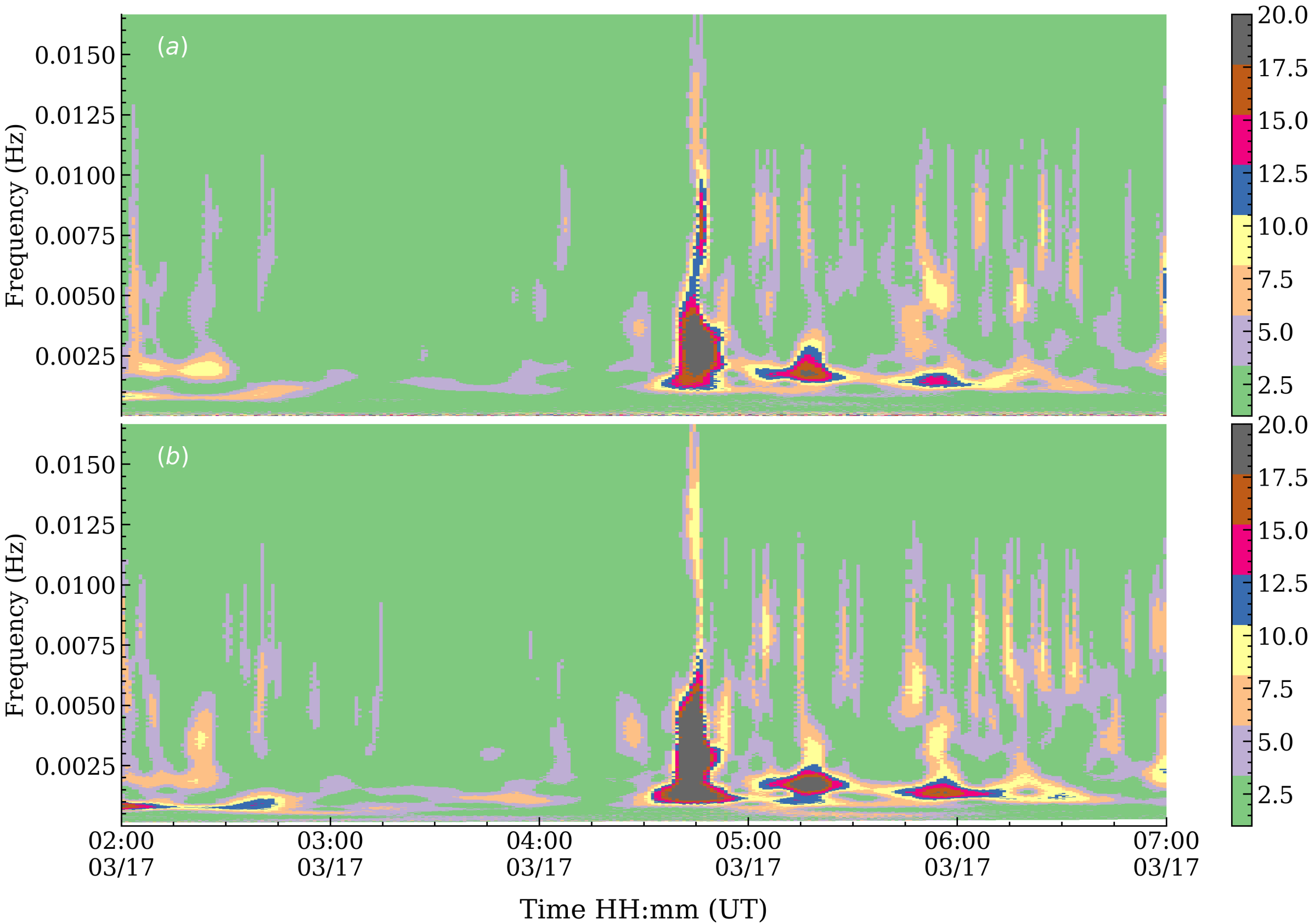


Figure.

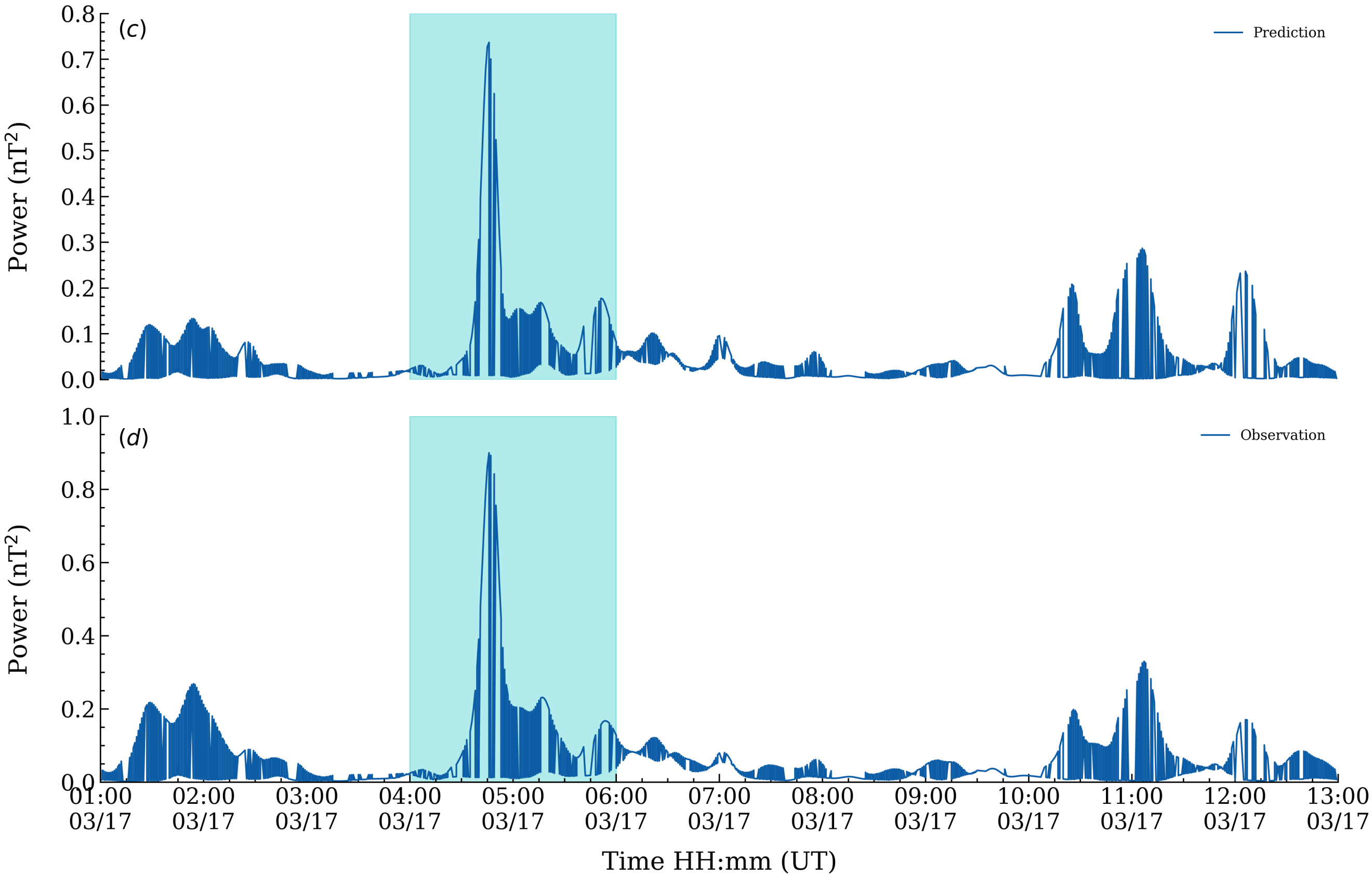


Figure.

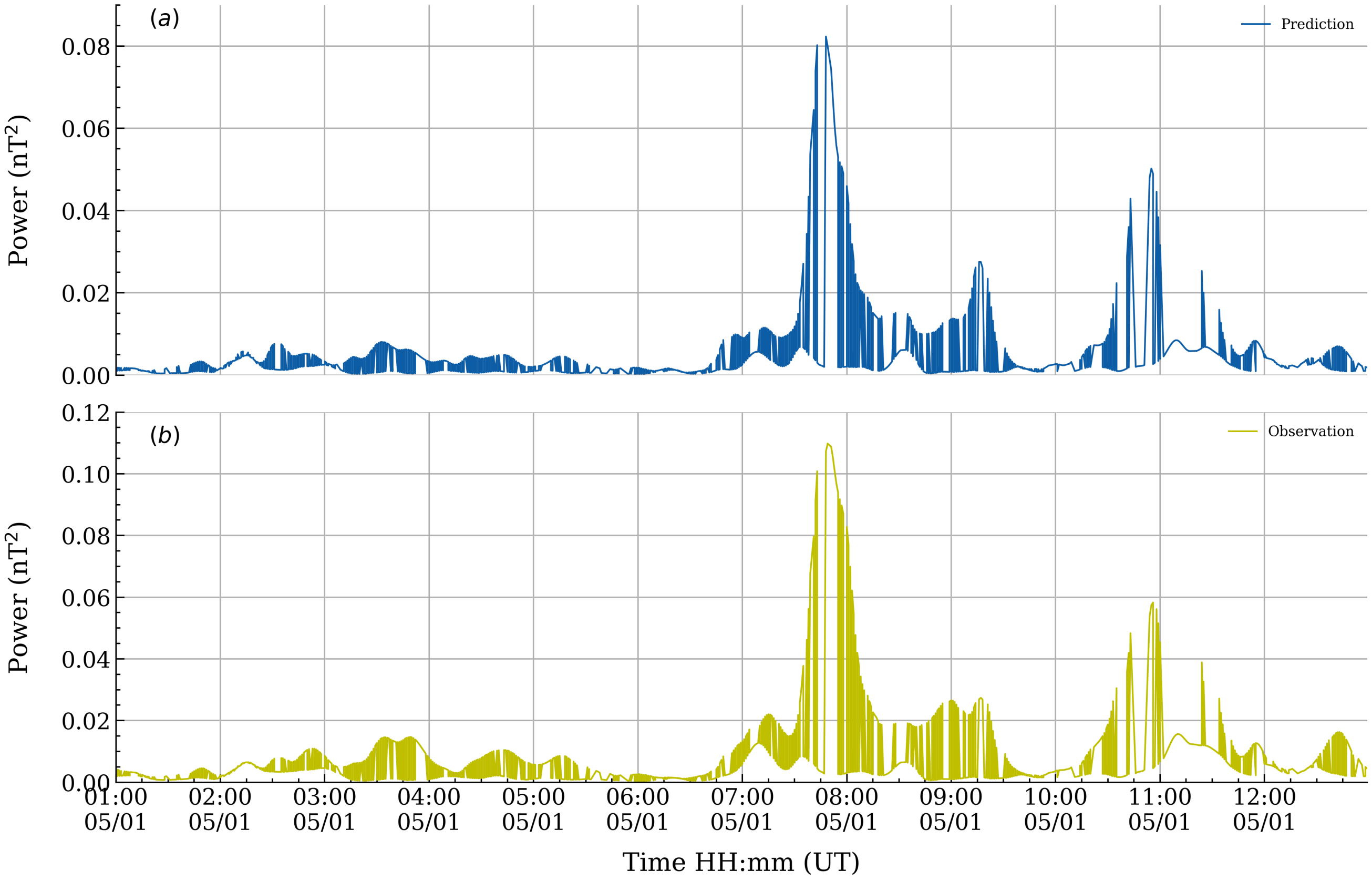


Figure.

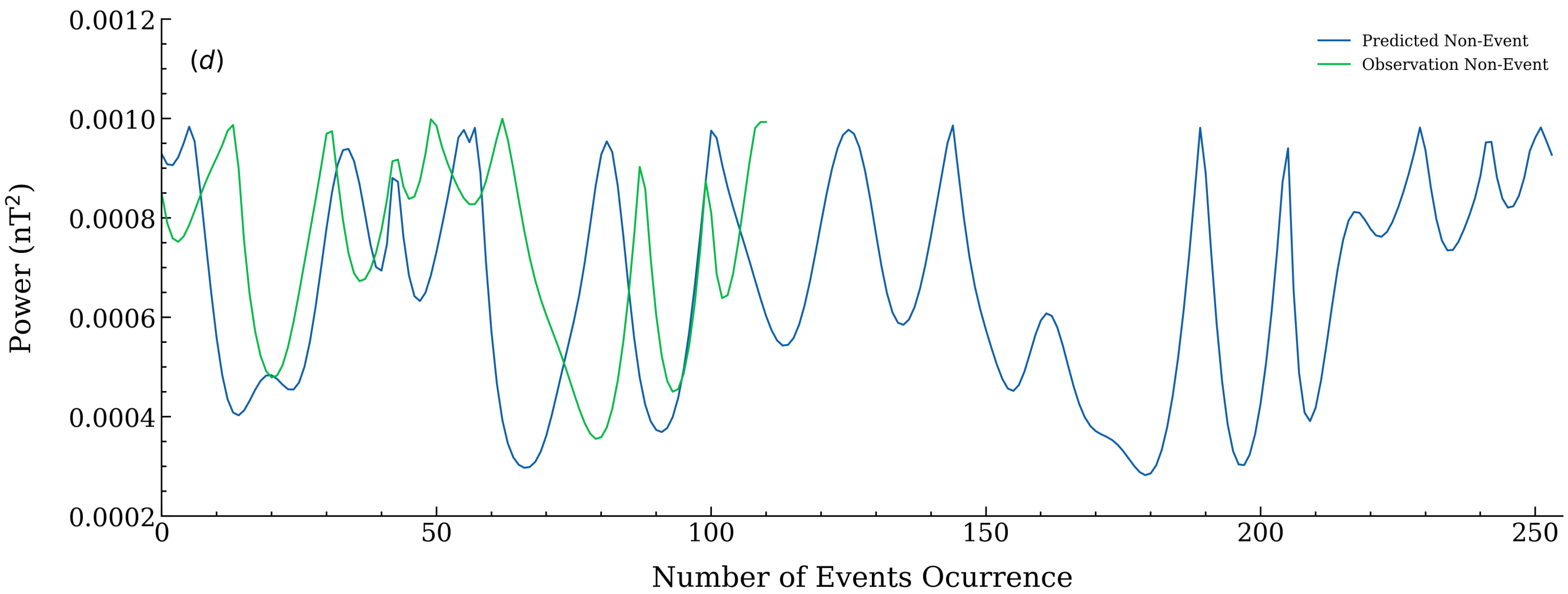
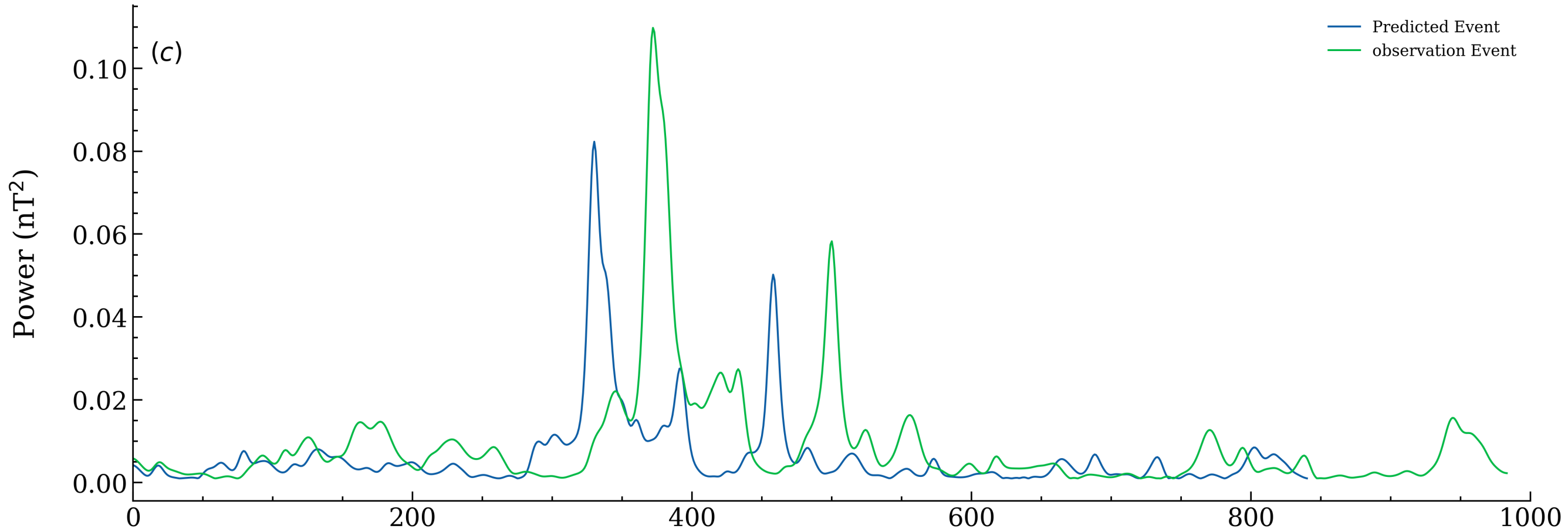
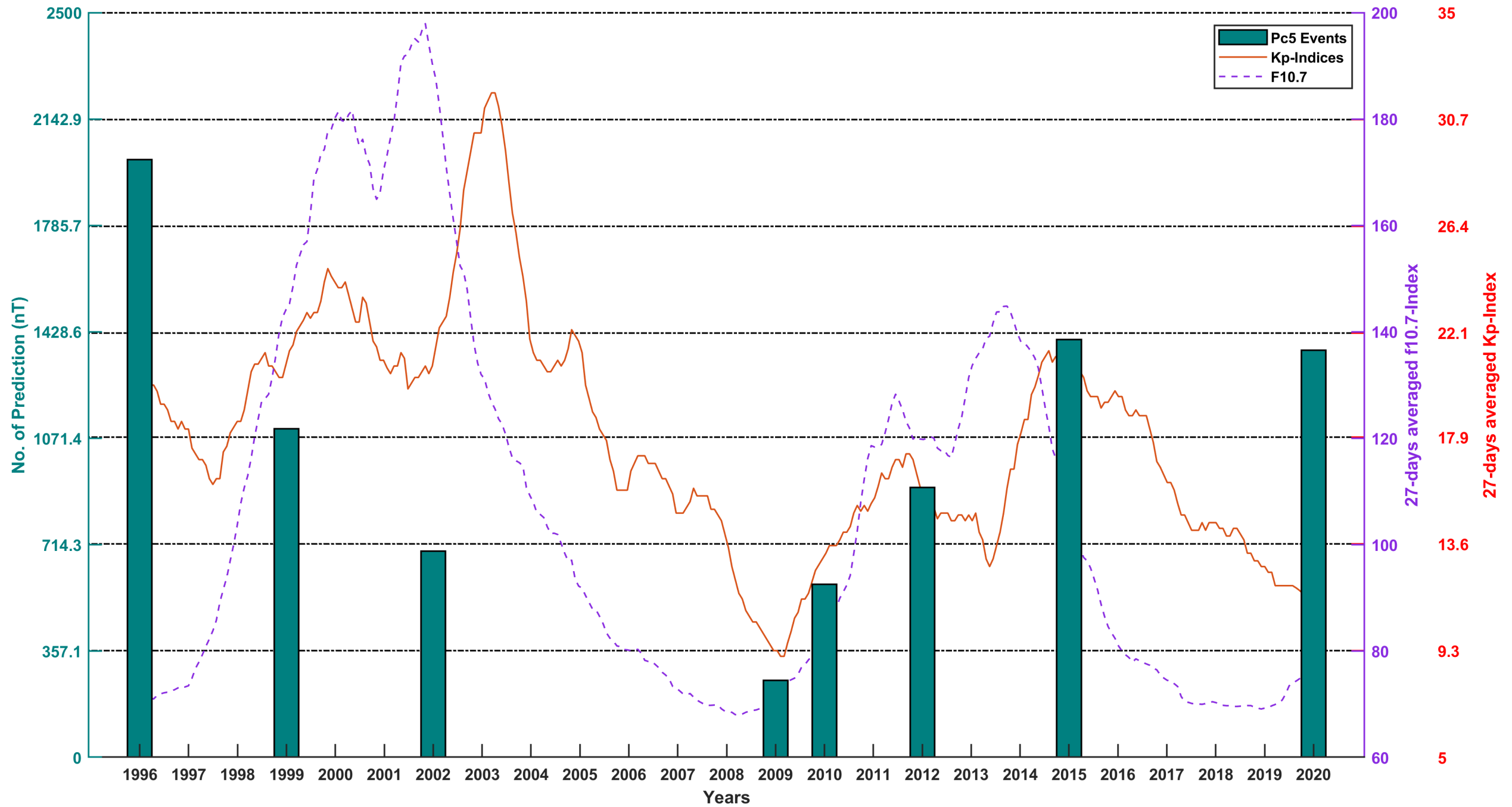


Figure.



Forecasting of Auroral Pc5 Pulsations from Solar Wind Parameters Using Machine Learning Approach.

Stephen Omondi^{1,3}, Justice Allotey Pappoe¹, Sebawato Nasurudiin¹, Ayman Mahrous^{1,2}

¹Department of Space Environment, Institute of Basic and Applied Sciences, Egypt-Japan University of Science and Technology (E-JUST), New Borg El-Arab City, Alexandria 21934, Egypt

²Department of Physics, Faculty of Science, Helwan University, Helwan, Cairo, Egypt

³Jomo Kenyatta University of Agriculture and Technology, Physics department, P.O.Box 62000-00200, Nairobi, Kenya

Key Points:

- We carried out the prediction of auroral Pc5 pulsations from solar wind parameters with the NARX network.
- Wavelet analytics was used in the definition of predicted Pc5 events
- Hinton diagram was used to display the internal structure of the trained model

Corresponding author: Stephen Omondi, stephen.owino.omondi@outlook.com

Abstract

The coupling between the magnetosphere and solar wind contributes to the energy, momentum, and mass transfer between the systems. However, geomagnetic pulsations facilitate the continuation of this process in the magnetosphere and the production of discrete auroral arcs. Therefore, remote-sensing the magnetospheric conditions. Data analytics with machine learning (ML) gives insight into scalability, adaptability, and feature extraction compared to traditional empirical models. The availability of big data in the Svalbard network spanning 25 years from 1996 motivated the current study. Hence, we present the forecasting of auroral Pc5 pulsations from solar wind parameters using the ML technique. In the training phase, there was a regression of 0.75 and MSE=11.90 nT². The relationship between Pc5 forecast and observations in low and high geomagnetic activity and solar activity showed good consistency with R=0.76 and MSE= 11.4 nT². For instance, the model adapted well to the St. Patrick geomagnetic storm of March 17th, 2015 despite uncertainties in the data. In addition, the model also adapted well with stunning performance in all Svalbard observatories with HOP leading with 6949 prediction events and NAL with the least. Thus, this was consistent with previous studies in terms of Pc5 pulsations latitudinal or L-shell dependence. Finally, validation with Kp and F10.7 indices presented excellent coherence between the models. Overall, The ML studied the connection between solar wind and interplanetary magnetic field properties to the ground magnetic field perturbations with good correlation results. Hence, the model will be fit for use by the magnetospheric community for space weather studies.

1 Introduction

Geomagnetic pulsations of the frequency band (1.7-6.7) mHz are generated by magnetospheric ultra-low frequency (ULF) waves. These waves contribute to the momentum, mass, and energy transfer and in the discrete auroral arcs production (Samson et al., 1996). The characteristics of Pc5 waves, majorly determined by the length of and plasma distribution along magnetic flux tubes, give means of remote-sensing magnetospheric conditions, for example, the radial spreading of the equatorial plasma density in the inner magnetosphere (Waters et al., 1995). The field line resonance theory explains the generation of Pc5 undulations (Chen & Hasegawa, 1974; Southwood, 1974). Shear velocity in the plasma flow on the magnetopause excites the Kelvin-Helmholtz instability, and the resulting surface waves propagate and penetrate the Earth's magnetosphere as fast compressional mode waves. When the compressional waves meet the region where the local field line eigenfrequency matches the fast mode frequency, the energy of compressional waves is coupled into shear Alfvén waves by the field line resonances. Consequently, waveguide theory (Harrold & Samson, 1992) and Cavity mode theory (Kivelson et al., 1984) also explain the discrete frequency field resonances. Overall, field line resonances theory has successfully been adopted to explain numerous features of in situ and ground observation of geomagnetic pulsations (Baddeley et al., 2007).

Pc5 pulsations frequently monitored at the auroral latitudes mostly using radars and ground magnetometers (Ziesolleck & McDiarmid, 1994) are of large amplitude (reaching 100 nT). According to the study conducted by Samson et al. (1971), the sense of Pc5 pulsations polarization and their amplitude spectra exhibit marked latitude dependence. Therefore, the maximum Pc5 amplitude occurs around magnetic latitude (MLat) between 65° and 75° (Kleimenova et al., 2010). In the auroral strip, Pc5 polarization fluctuates near noon and at the latitude of maximum amplitude. Thus, the ground magnetic field perturbations are in principle the field due to the ionospheric Hall currents. These measurements show that the perturbation of the northward magnetic field component peaks near the resonant field line location and $\sim 180^\circ$ phase shift across the resonant latitude (Lee et al., 2007). The fast-mode surface waves arrive at the resonance point via the field lines, oscillating them in the transverse direction. In principle, the ground-based observation of Pc5 pulsations would show that they travel with a small azimuthal wave num-

ber westward in the morning and eastward in the afternoon. Therefore, the maximum Pc5 amplitudes and intensity always peak along 73° MLat (Pilipenko et al., 2001).

Consequently, in the auroral oval, there are two unrelated electrodynamic phenomena; Pc5 pulsations and auroral electrojets (AEJ). AEJs are part of 3-D ionospheric current systems resulting from solar wind-magnetosphere couplings. These currents also flow either westward or eastward and are latitudinally confined by the Hall current. It was noted that AEJ intensity and Pc5 power peak at the same latitude and determined by unrelated processes. The Pc5 maximum intensity and position shift in latitude remained within the strips of AEJ of about 8° wide. Rostoker and Lam (1978) proposed an explanation for this consistency, reporting these waves are the eigenmodes of a 3-dimensional terrestrial magnetosphere-ionosphere current system. Pilipenko et al. (2001) findings were similar to that of Rostoker and Lam (1978); Pc5 pulsation temporal and spatial variations in the prenoon or morning sectors are intimately related to the intensity and location of auroral electrojet currents. Implying possible modulation of Pc5 waves from the magnetic contribution of AEJs in the region. Omondi et al. (2023) piloted a study on the automatic detection of auroral Pc5 pulsations guided by wavelet technique in the region separating Pc5 pulsation from raw data. Their findings were consistent with traditional results reporting large amplitudes of detected Pc5 pulsations.

Studies of geomagnetic activities using geomagnetic indices have shown that the magnetosphere behaves as a nonlinear dynamic system (Kamide et al., 1998). Various methods based on the physical, analytical or empirical relationships between geomagnetic parameters and solar wind, artificial intelligence, and correlations have been used to forecast geomagnetic activities (Williscroft & Poole, 1996; Wu & Lundstedt, 1996; Wu et al., 1998; Weigel et al., 1999; Gholipour et al., 2004; Uwamahoro & Habarulema, 2014; Eastwood et al., 2017; Wintoft et al., 2017; Chandorkar et al., 2017). The nonlinear autoregressive with exogenous input (NARX) model has widely been used for forecasting and modeling nonlinear systems. The NARX model performs well in the recognition of nonlinear systems by selecting the high-ranked model terms from a dictionary comprising numerous candidate model terms (Billings, 2013). Given that the magnetosphere is a nonlinear process, NARX presents itself to be the most efficient method for space weather predictions. The NARX models have been successfully used in the prediction of various geomagnetic indices, for instance, the AE index (Gu et al., 2019), Kp index (Ayala Solares et al., 2016), and the Dst index (Balikhin et al., 2011; Boynton et al., 2011; Wei et al., 2004) with great performance. Cai et al. (2009) studied storms by forecasting SYMH using ACE data which yielded a good performance with RMSE of $14nT^2$ and a correlation coefficient of about 0.9. Bhaskar and Vichare (2019) extended Cai et al. (2009) studies to predict the ASYH index by use of the NARX network. In that, they used ASYH and SYMH indices during the great geomagnetic storms occurring between 1998-2015 in two solar cycles, 23 and 24. The results were astounding as the forecasting model reproduces the entire time profiles of ASYH and SYMH with small time variations of about 10-30 min within noise level tolerance.

Several studies on Pc5 pulsations have pointed out its significance to space weather monitoring. Currently, there is no report on an ANN-based forecasting model available for ground Pc5 pulsations using solar wind parameters. The ANN-based prediction of ground Pc5 pulsations will be useful in understanding the contribution of internal and external drivers in the observed asymmetries. The forecasting model can be deployed to complement the issue of data loss and integrity problems in one station based on observations in others within the same network. The current work complements Omondi et al. (2023) studies in the Svalbard network utilizing the same dataset of solar cycle 23 and 24 to perform the auroral Pc5 prediction. Therefore, the main objective of the study is to develop a ground Pc5 prediction model using a dynamic NARX simulation model in the Svalbard network trained with solar wind parameters as input and feedback from the output. The robustness of the NARX model's performance in previous studies was

120 the motivation for its selection in the current study. The current paper is organized into
 121 5 sections: Section 2 introduces time series NARX feedback neural networks, section 3
 122 describes the data and methodology, section 4 gives results and discussion, and finally
 123 conclusion.

124 2 Time Series NARX Feedback Neural Networks

125 Artificial neural networks (ANN) are computation simulations that mimic biolog-
 126 ical neural networks in the brain (Poulton, 2002). They were first suggested by McCulloch
 127 and Pitts (1943) to study non-linear systems problems. There are numerous kinds of ANNs
 128 for modeling physical systems. In particular, the most frequently used ANN for mod-
 129 eling physical time series data is the MultiLayer Perceptron (MLP) Network. Feed-forward
 130 neural networks have been more effective than MLP in modeling nonlinear time series
 131 (Omondi et al., 2023). When simulating nonlinear time series, recurrent dynamic net-
 132 works with feedback are preferred. Therefore, the suitable and powerful type of recur-
 133 rent Network for nonlinear systems (time-series) is a nonlinear autoregressive network
 134 with exogenous inputs (NARX). Normally nonlinear systems are selected the same way
 135 as linear systems by considering the right parameters. Thus, in nonlinear systems, one
 136 can reconstruct the relation of the kind

$$o[t] = g(o[t-1], o[t-2], \dots, o[t-n_o], x[t-1], x[t-2], \dots, x[t-n_x] + e[t]) \quad (1)$$

137 Equation 1 shows a time series NARX model (nonlinear ARX), where g is a nonlinear
 138 function of fixed inputs and outputs. In the event of training NARX, the data are de-
 139 fined sequentially as $\chi^j = [o[t-j], o[t-j-1], \dots, o[k-j-(n_o-1)], x[t-j], x[t-j-1], \dots, x[t-j-(n_x-1)]]^T$
 140 and $\gamma^j = o[t-j+1]$, for $j=1, \dots, M$ (Ayala Solares et al., 2016). Where χ^j defines the context outputs and inputs while the γ^j is the target data.
 141 Once the training is done and the model has learned with good results. Next, the model
 142 is ready and saved for deployment. In the event of prediction or forecasting future val-
 143 ues of $o[t]$, the previous values $o[t-1], o[t-2], \dots, o[k-n_o], x[t-1], o[t-2], \dots, x[t-n_x]$
 144 grouped in one (n_o+n_x) -dimensional input vector are passed along with external
 145 inputs, x . Therefore, in this study, the simulation model here functions as a multiple in-
 146 put single output (MISO) system for prediction. The resultant model architectural de-
 147 sign used in the current work is schematically presented in Figure 1.

149 To make steps ahead predictions by estimating $o[t]$ at time t , and re-using the $o[t]$
 150 estimates in the input vector to forecast $o[t+1]$ without using true $o[t]$, target, the NARX
 151 simulation functions as a recurrent neural network. This way the output of the network
 152 will always depend on the input attributes (Billings, 2013). In essence the $o(t+1)$ is
 153 dependent on the previous values of an independent (exogenous) input signal $x[t]$, and
 154 previous values of the output signal $o[t]$; n_o and n_x are time delays of the output and
 155 input variables, and $e(t)$ is the model error or residual between the target and forecasted
 156 values.

157 The output of the hidden layer at time t is determined by Eqn.2 (Cai et al., 2009):

$$h_j(t) = \tanh \left[\sum_{k=0}^{n_x} w_{jk} x(t-k) + \sum_{l=1}^{n_o} w_{jl} o(t-l) + a_j \right] \quad (2)$$

158 w_{jk} is the weight connection between input, $x(t-k)$ and the j^{th} hidden neurons while
 159 that between hidden and output layers, $o(t-l)$ is given by w_{jl} . a_j is the bias in the j^{th}
 160 hidden layer neuron.

161 Figure 1 shows a simple NARX simulation architectural model designed using re-
 162 sults from Figure 2. This model consists of one input layer comprising four input nodes
 163 defined by the number of input attributes $x_1 - x_4$ and feedback inputs f_b , one hidden
 164 layer composed of 11 nodes, and one output node, o , in the output layer. The feedback

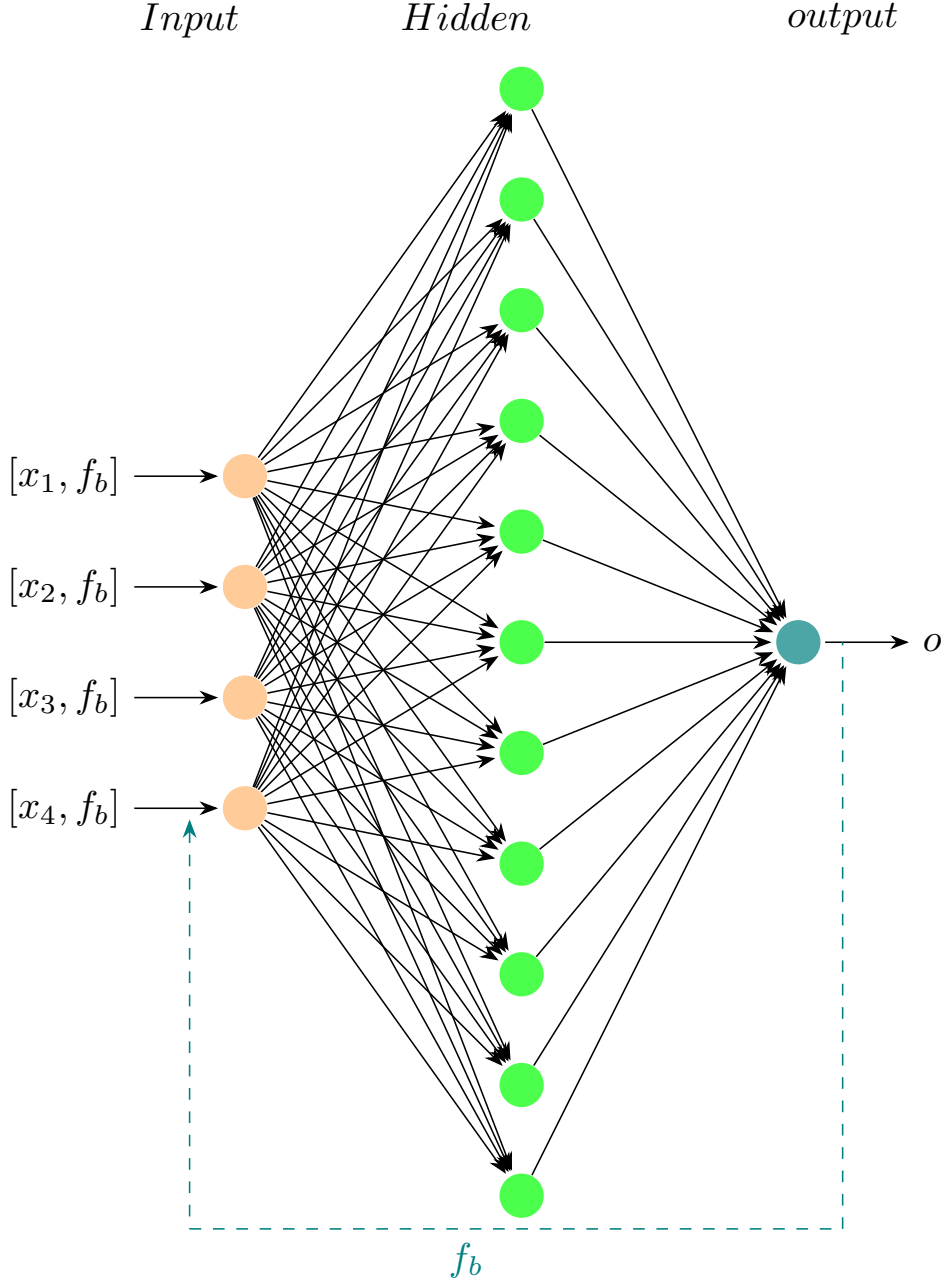


Figure 1. The simulation model architecture for NARX network. Where x_1-x_4 are the input values to the model input neurons (faint orange), the 11 green nodes in the middle are the hidden layer neurons while the teal node is the output layer neuron with o denoting the predictions. Finally, the feedback is denoted by f_b .

165 loop represented by f_b is the previous values from the model output, $o[t-1], \dots, o[t-4]$.
 166 Essentially, a dynamic neural network with the time steps synchronized data, $o[t]$ and
 167 $x[t]$ is illustrated by Figure 1. Figure 2 demonstrates the internal validation outcome of
 168 the NARX model performance on data during learning to obtain the optimum model
 169 with the best performance and less computation time. The first model's performance eval-

170 uation step was based on root mean square errors (RMSE) versus the number of nodes
 171 in the hidden layer. It became hard to select the model based on the first evaluation as
 172 there were many optimal model candidates based on this evaluation. Therefore, the sec-
 173 ond selection criterion on the regression against the number of neurons in the hidden layer
 174 was examined. Generally, we noticed all models qualify for learning machines except those
 175 below $N=8$. Where N is the number of nodes in the hidden layer. The argument on the
 176 error difference in RMSE and R values being less than a unit left the best choice to rely
 177 on the computation time. Keeping the same N and monitoring their computation time
 178 with a reasonable number of epochs to ensure no underfitting and overfitting in the learn-
 179 ing. Then that of fast computation time was selected. In principle, each dot plotted in
 180 Figure 2 represented a trained network against the number of hidden layer neurons in
 181 the x-axis and performance in the y-axis, upon which the optimal model is taken after
 182 25 trials. The selected optimal NARX model for the current work was the one with 11
 183 neurons in the hidden layers and an RMSE of 3.44 nT and $R=0.75$ as shown with the
 teal dashed line and red point in Figure 2 (a) and (b).

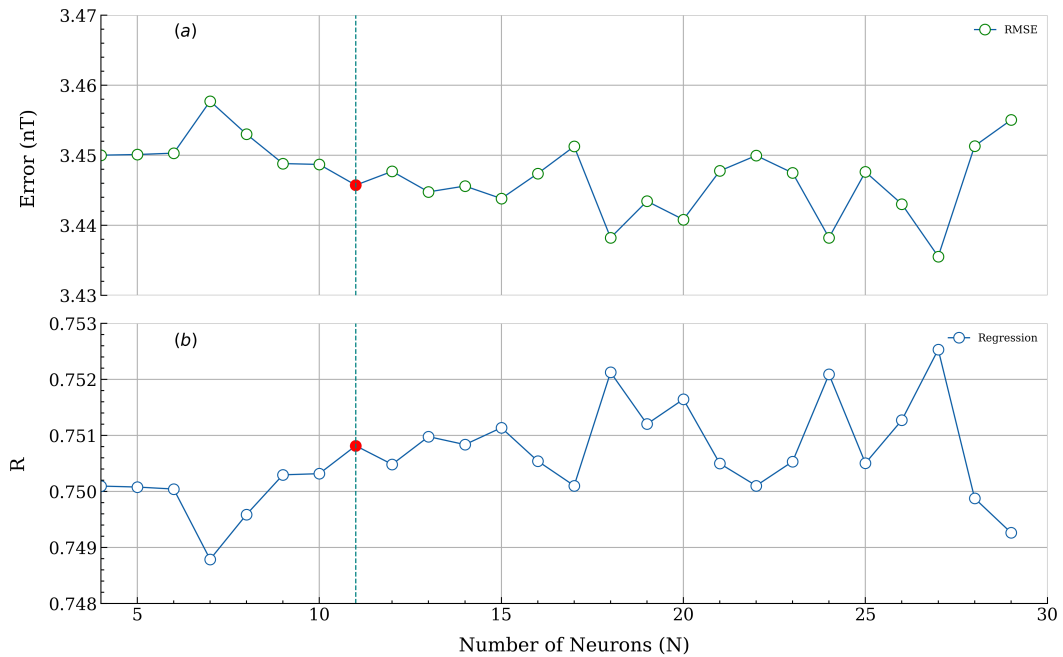


Figure 2. NARX model optimization profile of root mean square error and R versus the number of neurons in the hidden layer. The teal color dashed line indicates the selected number of neurons versus RMSE values for the present model for the prediction of Pc5 pulsation. The optimal model was (11,3.44) and (11,0.75) in terms of computation time.

184

185 3 Data and methodology

186 The ground magnetic field data of one minute resolution was obtained from the Sval-
 187 bard network for a period of 25 years from 1996 to 2020. These data were preprocessed
 188 and transformed into H-magnetic field coordinates from their X and Y-corrected geo-
 189 magnetic components. Svalbard network comprises 5 observatories, Bear Island (BJN),
 190 Hopen Island (HOP), Hornsund (HOR), Longyearbyen (LYR), and Ny Alesund (NAL).
 191 Pc5 pulsations were extracted by bandpass filtration technique from the H-component
 192 using Butterworth digital filter design (Omondi et al., 2023). The space events polar-

193
194

ized east-westward and south-northward are all captured by the H-component. Therefore, the H-component accounts for both local and global Pc5 pulsation beatings that would be observed worldwide during geomagnetic activity. Figure 3 illustrates the ge-

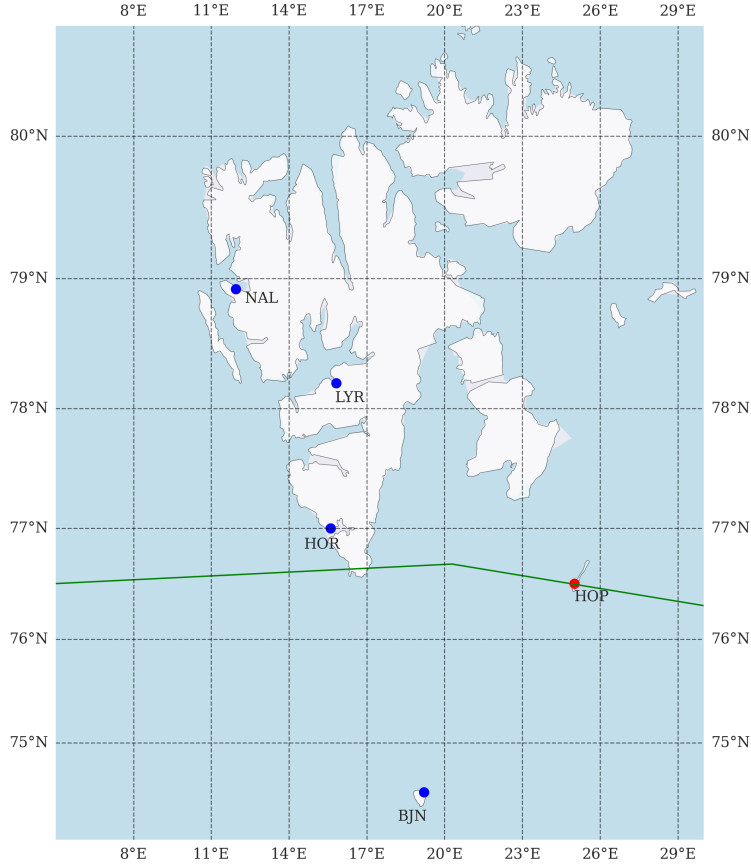


Figure 3. Topographical map of Svalbard network in the auroral region. The green-colored meridian is a line corresponding to the geomagnetic latitude recording the maximum amplitude and intensity of Pc5 pulsations, 73° .

195
196
197
198

ographical map of ground-based space monitoring stations of the Svalbard network. The green-colored meridian corresponds to the geomagnetic meridian of maximum Pc5 amplitude and intensity receptions (Pilipenko et al., 2001).

199
200
201
202
203
204
205

Benchmark of the previous study conducted by Omondi et al. (2023) to detect auroral Pc5 pulsations using machine learning; they found that the Pc5 pulsations under investigation were recorded simultaneously in the Svalbard network. Therefore, the same conclusion is applied in the current study. For this work, we used the NAL station in modeling machine learning algorithms in the training phase and the other four stations were used in the deployment of the model during the testing phase. The northward geolocation of the NAL observatory (75.25°) to other stations in the Svalbard network was

206 of interest as it is on the outer or near outer edge of the auroral oval strip (65°-75° mag-
 207 netic latitude) since it records fairly clean space events relative to others in the auroral
 208 oval. Deployment of the machine learning model in other stations in the Svalbard net-
 209 work aside from the used to train it presents an interesting evaluation of the capability
 210 of the machine learning model in the complex data environment. Given that stations in
 211 the network receive the same Pc5 waves in terms of the frequency band, they are polar-
 212 ized differently (phases) with fluctuating powers dependent on the L-shell values.

213 The solar wind parameters observed near the Lagrange's (L-1) point of 1 minute
 214 cadence starting from 1996 to 2020 were employed. In particular, to train our machine
 215 learning algorithms, we selected four solar wind parameters measured near L-1 point;
 216 these parameters are regarded as the most important drivers triggering geomagnetic ac-
 217 tivity causing Pc5 pulsations. These variables comprise the Z-component of the inter-
 218 planetary magnetic field magnitude (IMF- B_z) in GSM coordinate, the plasma temper-
 219 ature (T_e), the proton density (n_p), and the earthward solar wind velocity (V_x). The
 220 Z-component of the interplanetary magnetic field (IMF- B_z) contributes largely to the
 221 amount of momentum and energy transport from the solar wind to the Earth's magne-
 222 tosphere by magnetic reconnection at the dayside magnetopause (Dungey, 1961). Thus,
 223 the knowledge of (IMF- B_z) fields is key for monitoring and forecasting the energy in-
 224 put into the magnetosphere-ionosphere system. Therefore, to guide the modeling of the
 225 non-linear system, the machine was to learn from the solar wind parameters with the
 226 Pc5 waves as the target.

227 The input datasets were wrangled to remove missing data and transformed into in-
 228 telligible data suitable for machine learning, finally, synchronized with the Pc5 pulsa-
 229 tions to have the same data frames. The data were partitioned into two categories, the
 230 training set spanning 17 years and shuffled 8 years of data from two solar cycles, 23 and
 231 24 for testing or deployment purposes. In the training phase, we partition data 70% train-
 232 ing, 15% internal testing, and 15% validation. The training dataset was randomly ex-
 233 tracted from the 17 years of simulation time series distributed over two solar cycles, 23
 234 and 24. The validation was done using Kp and F-10.7 indices, 27 days averaged with the
 235 model evaluation results from the test data. The Kp and F10.7 indices data set of 25
 236 years from 1996 synchronized with 8 years of test data from two solar cycles. The train-
 237 ing algorithm was based on the error back-propagation algorithm. The Levenberg-Marquardt
 238 backpropagation which uses trainml to learn was utilized because it is faster to train (Omondi
 239 et al., 2023). For every epoch, the loss function (cost function) is calculated by Eqn. 3.

$$E = \frac{1}{2} \sum_{j=1}^M (T_j - O_j)^2 \quad (3)$$

240 where T_j and O_j are the true output and prediction output, where M is the number of
 241 the training samples (Cai et al., 2009). The prediction performance was obtained using
 242 the mean square error (MSE):

$$MSE(O, \hat{O}) = \frac{1}{m} \sum_{j=1}^m (O_j - \hat{O}_j)^2 \quad (4)$$

243 where the O_j is the j^{th} of m output of the initial open net network with T_e , IMF- B_z , n_p
 244 and V_x as its input, and \hat{O}_j is corresponding output as predicted by NARX. The root
 245 mean square error was calculated from the square root of MSE in equation 4. The cross-
 246 correlation coefficient, R, is given by equation 5.

$$R(O, \hat{O}) = \frac{1}{m} \sum_{j=1}^m \left(\frac{O_j - \mu(O)}{\sigma(O)} \right) \times \left(\frac{\hat{O}_j - \mu(\hat{O})}{\sigma(\hat{O})} \right) \quad (5)$$

247 The R values are used to determine the prediction accuracy of the neural network. where
 248 $\mu(\hat{O})$ and $\mu(O)$ represent the mean values of the predictions results and observations,
 249 respectively. $\sigma(\hat{O})$ and $\sigma(O)$ are the standard deviations.

250 Time series comprising nonstationary power at many distinct frequencies can be
 251 analyzed by wavelet transform (Daubechies 1990). Supposing that one has a time series
 252 observation, y_m , with equal time spacing δt and $m=0 \dots M-1$. If one also has wavelet functions, $\psi(\xi)$,
 253 which is dependent on a non-dimensional ‘time’ parameter ξ . To be permitted as a wavelet,
 254 this function must be localized in both frequency and time space and also have zero mean
 255 (Farge 1992). Consider the Morlet wavelet, consisting of a plane wave modulated by a
 256 Gaussian:

$$\psi_0(\xi) = \pi^{-\frac{1}{4}} \cdot e^{i\omega_0\xi} \cdot e^{-\frac{\xi^2}{2}} \quad (6)$$

257 where nondimensional frequency is given by ω_0 and taken to be 6 to satisfy the admis-
 258 sibility condition (Farge 1992). The continuous wavelet transform of y_m discrete signal
 259 is defined as the convolution of y_m with a translated and scaled version of $\psi_0(\xi)$:

$$W_m(s) = \sum_{m'=0}^{M-1} y_{m'} \psi^* \left[\frac{(m' - m)\delta t}{s} \right] \quad (7)$$

260 where the complex conjugate is indicated by (*).

$$\hat{\psi}(s\omega_k) = \left\{ \frac{2\pi s}{\delta t} \right\}^2 \psi_0(s\omega_k) \quad (8)$$

261 For morlet wavelet, the function $\hat{\psi}_0(s\omega_k) = \pi^{-\frac{1}{4}} \cdot H(\omega) \cdot e^{-\frac{(s\omega - \omega_0)^2}{2}}$ and each of the un-
 262 scaled $\hat{\psi}_0$ is defined to have $\int_{-\infty}^{+\infty} |\psi_0(\omega')|^2 d\omega' = 1$, i.e they have to be normalized to a
 263 unit energy. Utilizing Normalizations at every scale s one has

$$\sum_{k=0}^{J-1} |\hat{\psi}(s\omega_k)|^2 = J \quad (9)$$

264 where the number of points is given by J . Using the convolution formula in equation 7,
 265 the normalization of the wavelet function is given by:

$$\psi \left[\frac{(m' - m)\delta t}{s} \right] = \left(\frac{\delta t}{s} \right) \psi_0 \left[\frac{(m' - m)\delta t}{s} \right] \quad (10)$$

266 where energy of $\psi_0(\xi)$ is normalized to unity. If the wavelet function $\psi(\xi)$ is complex,
 267 then its transform will also be complex, $W_m(s)$. Therefore, the real and complex com-
 268 ponents of wavelet transform are expressed as $\Re\{W_m(s)\}$ and $\Im\{W_m(s)\}$ respectively.
 269 The amplitude and phase of the wavelet transform are obtained as $|W_m(s)|$ and $\tan^{-1} \left[\frac{\Im\{W_m(s)\}}{\Re\{W_m(s)\}} \right]$
 270 correspondingly. Consequently, the wavelet power spectrum is defined by $|W_m(s)|^2$. Af-
 271 ter the successful selection of the wavelet function, the immediate task is to choose scales, s ,
 272 to use in the wavelet transform. Therefore, wavelet scales are written as a set of frac-
 273 tional powers of 2 shown in equations 11 and 12.

$$s_n = s_0 2^{n\delta n}, \quad n=0,1,2,\dots,N \quad (11)$$

274

$$N = \frac{\delta}{n} \log_2(J\delta t/s_0) \quad (12)$$

275 Where N and s_0 are the largest and smallest scales. In the Morlet wavelet, $\delta n = 0.5$
 276 is the largest permitted value that gives enough sampling in scales. Given that wavelet
 277 transform is essentially a bandpass filter with a known wavelet function (response func-
 278 tion). The original time series can be reconstructed after wavelet transformation using
 279 either an inverse or deconvolution filter. In our case, the original signal was reconstructed
 280 by taking the sum of the real part of the wavelet transform over all scales.

$$y_m = \frac{\delta_n \delta_t^{\frac{1}{2}}}{C_\delta \psi_0(0)} \sum_{n=0}^N \frac{\Re[W_m(s_n)]}{s_n^{\frac{1}{2}}} \quad (13)$$

281 The energy scaling is removed by $\psi_0(0)$ and the conversion of wavelet transform to en-
 282 ergy density is performed by $s_n^{\frac{1}{2}}$. The C_δ is the reconstruction factor of δ from its wavelet
 283 transformation using $\psi_0(\xi)$. Given a new wavelet function, C_δ can be derived by tak-
 284 ing time series of a δ function at times $m = 0$ provided $y_m = \delta_{m_0}$. Therefore, the wavelet
 285 transform becomes:

$$W_\delta(b) = \frac{1}{M} \sum_{k'=0}^{M-1} y_{m'} \psi^*(s\omega_k) \quad (14)$$

286 The reconstruction of equation 14 is:

$$C_\delta = \frac{\delta_n \delta_t^{\frac{1}{2}}}{\psi_0(0)} \sum_{n=0}^N \frac{\Re\{W_\delta(s_n)\}}{s_n^{\frac{1}{2}}} \quad (15)$$

287 where, the C_δ is constant and scale dependent for every wavelet function. Following the
 288 energy conservation principle the total energy is conserved and Parseval's theorem for
 289 wavelet analytics is:

$$\sigma^2 = \frac{\delta_n \delta_t^{\frac{1}{2}}}{C_\delta M} \sum_{m=0}^{M-1} \sum_{n=0}^N \frac{|W_m(s_n)|^2}{s_n^{\frac{1}{2}}} \quad (16)$$

290 where δ is for the reconstruction and σ^2 is the variance.

$$\overline{W_m^2} = \frac{\delta_n \delta_t^{\frac{1}{2}}}{C_\delta} \sum_{n=n_1}^{n_2} \frac{|W_m(s_n)|^2}{s_n^{\frac{1}{2}}} \quad (17)$$

291 Equation 17 and 16 illustrates wavelet scaled power averaging of a wavelet transform in
 292 the signal transformation and reconstruction formulations. After training the ML model,
 293 its performance was evaluated by wavelet power spectrum analysis. Thresholds for dis-
 294 tinguishing predicted events and non-events were set guided by wavelet power transform
 295 techniques. This technique was performed by passing the machine learning output sig-
 296 nal through a filter-like algorithm (wavelet power transform) to define the predicted Pc5
 297 events from background noise. This concept is visualized in the schematic diagram shown
 in Figure 4.

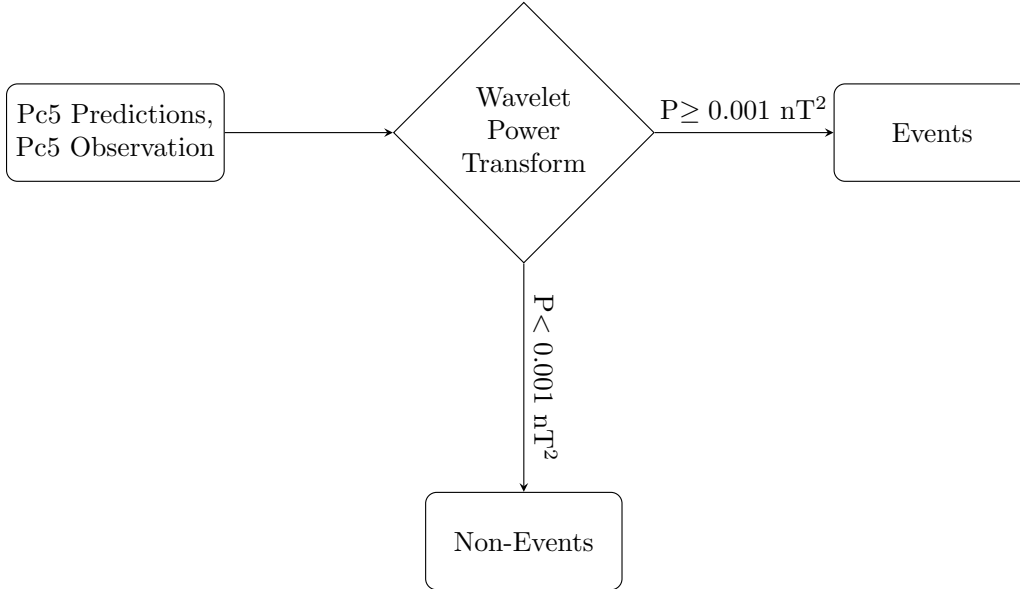


Figure 4. Illustration of Pc5 Event definition from forecast results

4 Results and Discussion

4.1 Network Performance

In the current study, we present the NARX neural network as a machine learning (ML) tool in predicting Pc5 pulsations. The network took 142 out of 1000 epochs to train the model with a performance of $MSE=11.90 \text{ nT}^2$. The overall training time of about 00:18:25 hours was observed. The number of epochs and time taken to train the model was fair enough to qualify good learning indicating that there were no overfitting and underfitting. Therefore, it was arguably convincing to state that the model indeed found it easy to learn from the data and regularize with the target data to yield a good performance. The resultant model's intelligible weights and biases were pictorially presented using the Hinton diagram shown in Figure 5. The color coding of the squares represents the weight and bias signs values, whereby red and green colors correspond to negative and positive values respectively. The scale size of each square is equivalent to the weight and bias magnitude values in each layer having a maximum magnitude equal to 1. The Hinton diagram demonstrates neuron connections of the learned model between inputs, hidden layer, and output giving more insight into trained weights distribution. To unravel the black box of the artificial network or network intelligence of the trained model, Figure 5 gives the intuition. In layer 1 of Figure 5 there are 8 parallel inputs in input 1 comprising of connection from 4 external inputs and 4 context inputs (feedback) to the 11 hidden nodes in the hidden layer forming an 8 by 11 network matrix. Hence, the overall distribution of weights in layer 1, input 1, is 88 connections and 88 weights. In the input 2, layer 1, there are 11 biases and 22 weights. In Layer 2 (the connection between the hidden layer and output) there are 11 weights and 1 bias. Contrary to Figure 1, the same arrangement as in Figure 5 was expected but there are only 4 inputs defined by input attributes looped with feedback. At the initial condition, the extra 4 context input does not exist as there is no output. These context inputs are automatically created during the machine-learning process. Therefore Hinton diagram comes in handy to give the resultant picture of the trained model weights and network distributions with more details. Overall, the ML model demonstrated a strong node connection.

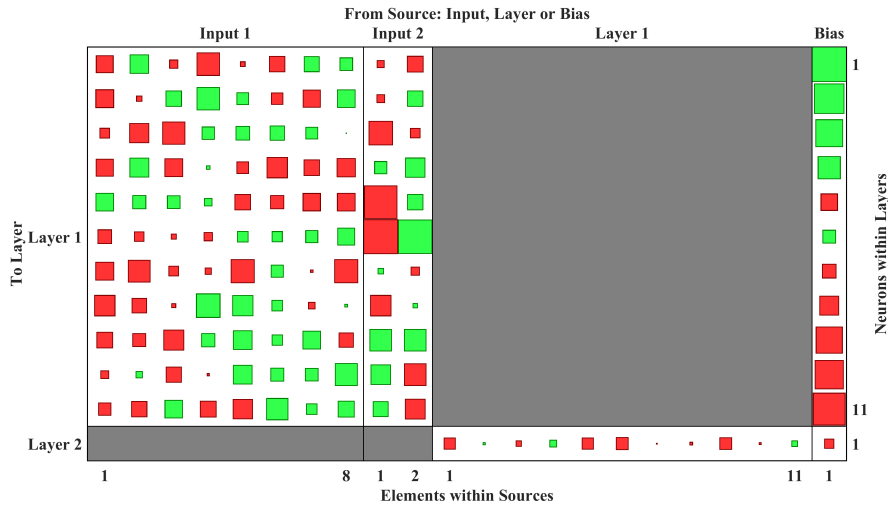


Figure 5. Hinton diagram of ML model showing trained weights and biases with their corresponding values and magnitudes. The diagram demonstrates strongly connected neurons presenting good learning. Where green and red colors are positive and negative values respectively. The size of the square represents the element magnitude.

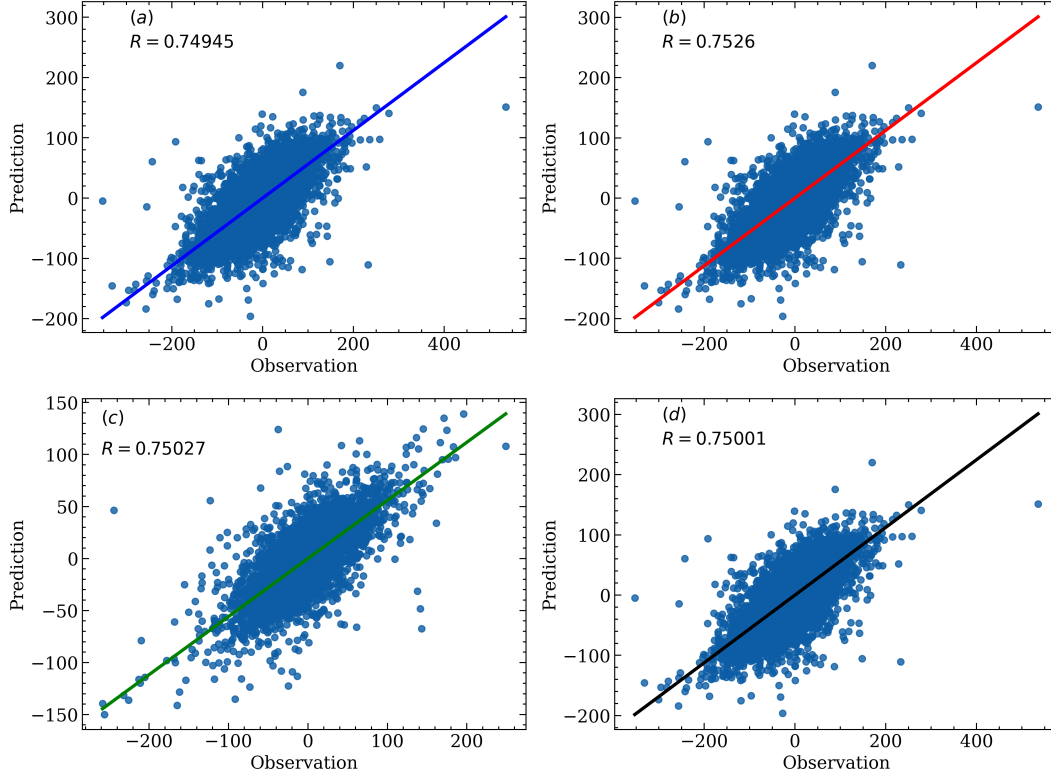


Figure 6. Machine Learning training results for 17 years of the two cycles, 23 and 24. Where (a)-(d) are scatter plots for training, testing, validation, and finally the overall performance.

327

328 Figure 6 shows the internal network evaluation in the training phase. Hence, the
 329 regression coefficient of the training, testing, validation, and general performances yielded
 330 an overall of 0.75. Hence, scaling well with big data. Despite high amplitude spikes and
 331 outliers in the data, the model responded with a good performance in the training phase.
 332 The model generalizes well with R values of 0.7495 indicating good learning. Validation
 333 and internal testing showed a good consistency between prediction and observation having
 334 R values of 0.75 overall. The metric measurement of the model training realizes an
 335 RMSE of 3.44 nT and MSE of 11.90 nT².

336

4.2 Model Performance on test data

337 After the training phase, the resultant simulation model was deployed on test data
 338 to evaluate its performance and robustness. Figure 7 shows the regression between ob-
 339 servation (target) and the prediction for both high and low solar activities from some
 340 selected years in the ascending and descending phases of solar cycles 23 and 24. Figure
 341 7 (a-c) illustrates the network model performances for the years 1999, 2002, and 2010
 342 with an averaged R-value of 0.76 while Figure 7 (d) shows the yield for the year 2020
 343 having R-value of 0.57. The metric evaluation on MSE also yielded 9.15 nT², 8.23 nT²,
 344 3.70 nT², and 24.52 nT² for 1999, 2002, 2010, and 2020 respectively. The performance
 345 in the year 2020 was unusual compared with other years in the test case, possibly due
 346 to the complexity of the dataset. Comparing 2020 performance generally with other years'
 347 test data as shown in Figure 15, the number of prediction events was also anomalous con-
 348 trary to the expectation as observed in the year 2009. This points out the dynamic re-
 349 sponse of the model to different dataset complexities. Overall, there was a good corre-

350
351

lation between prediction and observation with a performance of $\text{MSE} = 11.40 \text{ nT}^2$ despite uncertainties in the datasets.

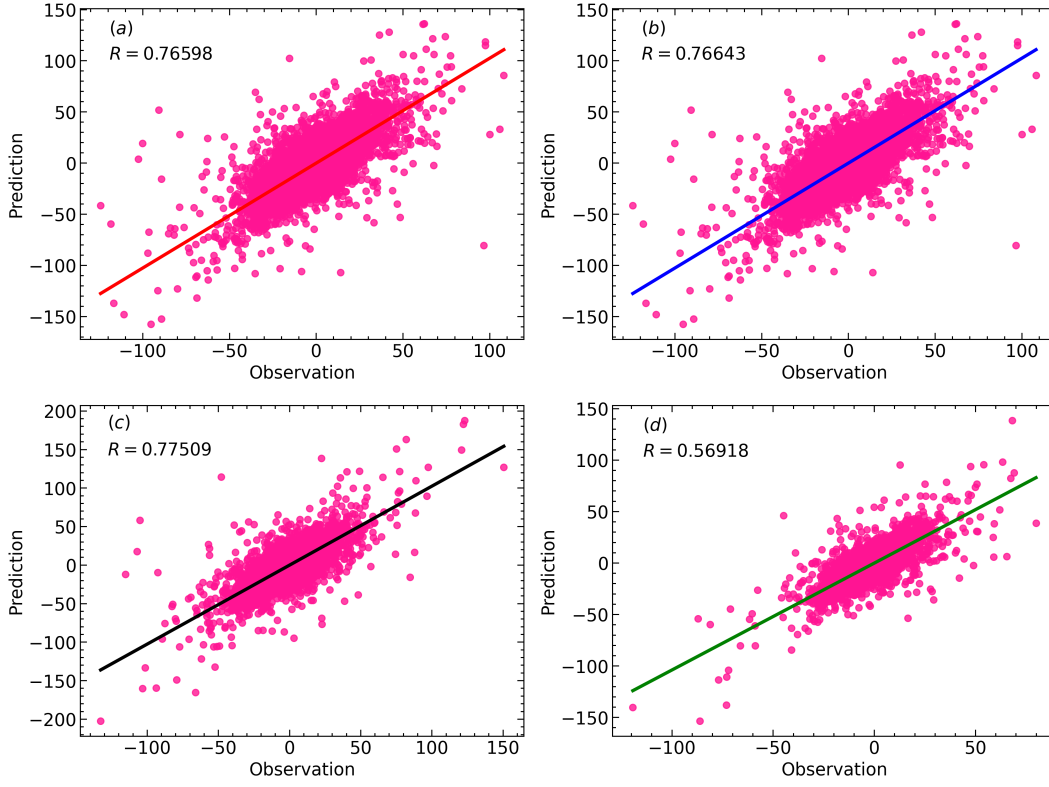


Figure 7. Machine learning test performance on a fresh data set of both active and high solar wind activities spanning both phases of solar cycle 23 and 24. Where (a),(b), (c), and (d) are test responses of the years 1999, 2002, 2010, and 2020 response from the NAL observatory respectively.

352
353
354
355
356
357
358
359
360
361
362
363
364
365
366
367
368
369

The model was also deployed to study the response to a strong geomagnetic storm. Therefore, the geomagnetic storm of St. Patrick's Day of March 17th, 2015 with maximum Ap and Kp indices of 108 and 8- ($7\frac{2}{3}$) respectively was picked as an illustrious case study. This storm was strong and caused disturbances in the magnetospheric current system and energy injection into the magnetosphere cavity. As a consequence, the injected energy resulted in the generation of plasma waves. These waves contribute to the transportation of momentum, mass, and energy in the entire geospace. Given that Pc5 waves are giant plasma waves of ultra-low frequency with wider bands generated from field line resonances. Thus, this became the first step of the model deployment of the Pc5 prediction in the nonlinear conditions of the magnetospheric system. Figure 8 shows the spectral analysis of the machine learning prediction outcome and Pc5 observation on the St.patrick day. The zoomed plot of Figure 8 highlights a clear visualization of the relationship between ML output and the observations. There exists a strong match between the observation and ML outcome throughout the day with some small amount of outlier spikes. Overall, the predicted Pc5 wave patterns were excellently reproduced and had a good correlation with observation. Time-frequency and spectral characteristics of the prediction against the observation were studied in Figures (9 and 10) using the time window of intense Pc5 pulsation highlighted in teal color in Figure 8.

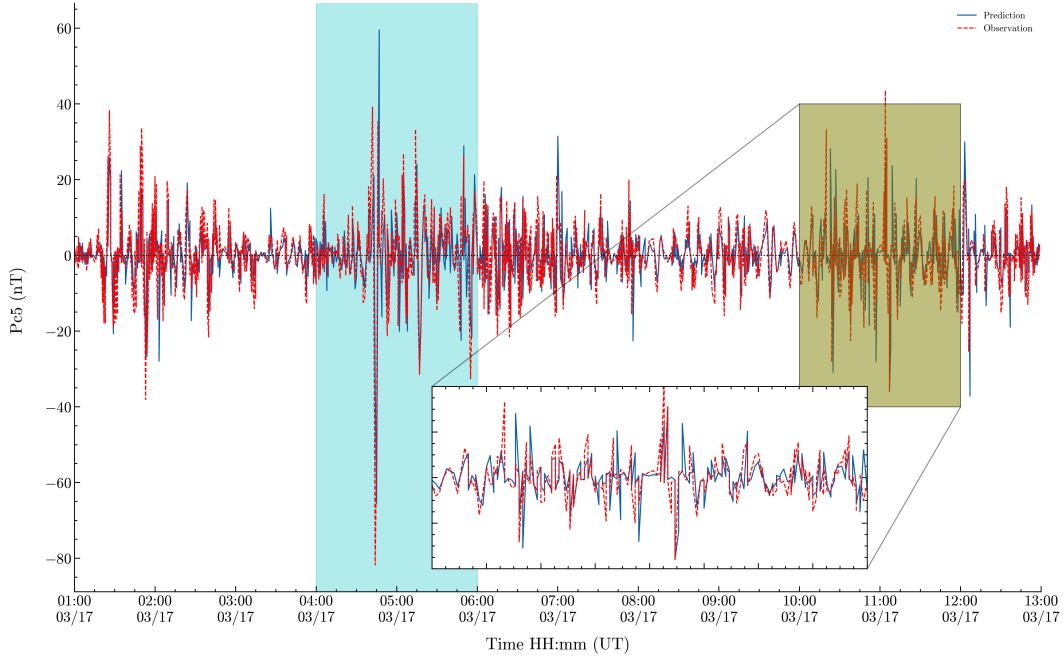


Figure 8. Time series prediction and observation plot on the geomagnetic storm of March 17, 2015 at NAL observatory. The zoomed graph shows the correlation between observation and prediction highlighted in light olive color.

370 Figure 9 shows wavelet analytics of the Pc5 prediction and observations correspond-
 371 ingly. Whereby, Figure 9 (a) & (b) are the scalograms of the actual observations and pre-
 372 dictions of Pc5 pulsations of the Morlet wavelet continuous transformation. The scalo-
 373 grams were of the signals highlighted in teal color in Figure 8. The signature of high am-
 374 plitudes seen in Figure 8 both for observation and predicted Pc5 dominated as well in
 375 the scalogram presenting high energy pulsations. Surprisingly, the prediction scalogram
 376 is more filtered than the observation one with clear patches, this is because of the wavelet
 377 time-frequency duality property. Fundamentally, the wavelet transformation works on
 378 the identification of real signals from noise-infested signals on the principle of time-frequency
 379 features. Figure 9 (a) and (b) show Pc5 signals corresponding to their frequencies and
 380 the approximation in green color. On the other hand, the Pc5 prediction event defini-
 381 tion was based on the analyses of Figure 9, 10 and 11. Therefore, carrying out the scale-
 382 averaged wavelet power spectrum analyses, the wavelet filter banks and signal in the in-
 383 put of the scaled-averaged wavelet function return the scales-averaged signals with their
 384 frequency and period coefficients. Figure 10 (c) & (d) are the scaled-averaged wavelet
 385 power spectra of Pc5 pulsations and predictions respectively. The results in 9 (a) & (b)
 386 and Figure 10 (c) & (d) showed that the detected Pc5 signals in the scalograms corre-
 387 spond to the energized power wavelet coefficients of the same signals having a good match.
 388 These report that the predicted signal was indeed Pc5 pulsations piloting further anal-
 389 yses to define the pure waves based on wavelet power analysis. To identify clean Pc5 pul-
 390 sations predictions against actual observation, the forecasted data were threshold at 0.001
 391 nT² against observations schematically demonstrated in Figure 4.

392 On the other hand, the event definition using the wavelet power spectrum technique
 393 was employed on a minor geomagnetic storm of January, 5th 2015 as a bare minimum
 394 of geomagnetic conditions. This was to account for Pc5 pulsations occurring due to magnetosphere-
 395 solar wind coupling dynamics other than the coronal mass ejections. Figure 11 (a) and
 396 (b) shows the Wavelet scale-average wavelet power spectrum of Pc5 pulsations of Jan-

397 uary, 5th 2015 minor geomagnetic storm. In comparison to Figure 10 (a) and (b), it was
 398 observed that the magnitude of normalized Pc5 pulsations was ten times as to the re-
 399 sponse in Figure 11 (a) and (b). This demonstrates the strength of St. Patrick's strong
 400 geomagnetic storm to minor storm. For this reason, the Pc5 events were defined using
 401 the observation in Figure 11 (a) and (b). In the previous study, Omondi et al. (2023)
 402 defined their Pc5 prediction events on the threshold above 20 nT. Historically in the auroral
 403 zone, it is well known to record large Pc5 pulsations. Therefore their threshold was
 404 to exclude ULF waves contributed by background noise as well as maintaining pulsations
 405 recorded in the quiet days. In the current study, ULF waves were detected using mor-
 406 let wavelet transform to observe time-frequency response and invite further diagnosis.
 407 Observing that these signals within the Pc5 band for both, there was a need to exclude
 408 those that mimic Pc5 waves by using wavelet power spectrum as they represent the back-
 ground noise.

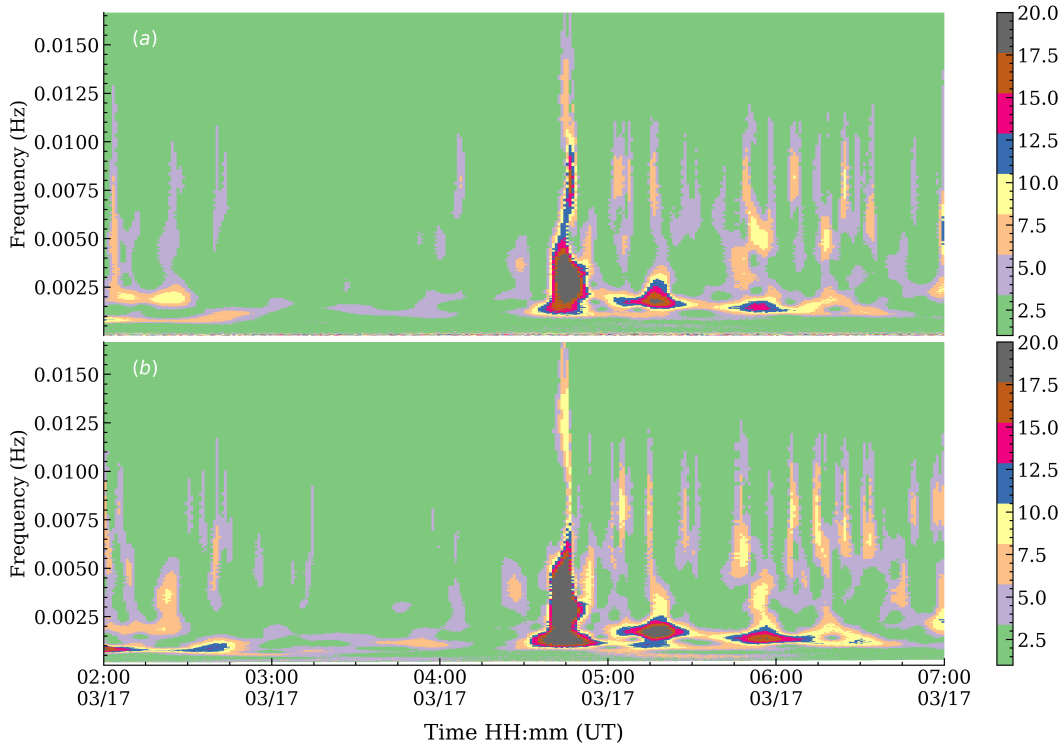


Figure 9. Wavelet analyses of Pc5 pulsations. Panels (a) and (b) are scalograms of actual Pc5 and Predicted. The measurement recorded on the geomagnetic storm occurred on St. Patrick day of March 17, 2015. The analysis presented corresponds to the highlighted section in cyan color in Figure 8.

409

410 Figure 12 (a) & (b) demonstrates the Pc5 events and non-events of the predictions
 411 and actual measurements respectively. These observations give more insights into Fig-
 412 ure 9 as hot colors corresponding to Pc5 events with a higher power as in Figure 12 (a).
 413 Consequently, the cool colors in the scalograms are background noise which is consid-
 414 ered non-events. Whereby, the hot colors are those greater than 5 while the cool ones
 415 are those within or less than 5 as indicated in the color bar. Therefore, wavelet power
 416 spectra and continuous wavelet transformation of the Pc5 pulsations analyses were im-
 417 portant in the determination of the number of Pc5 pulsations predicted in each station
 418 in the Svalbard network. Figure 12 (a) shows that there are more actual Pc5 events com-

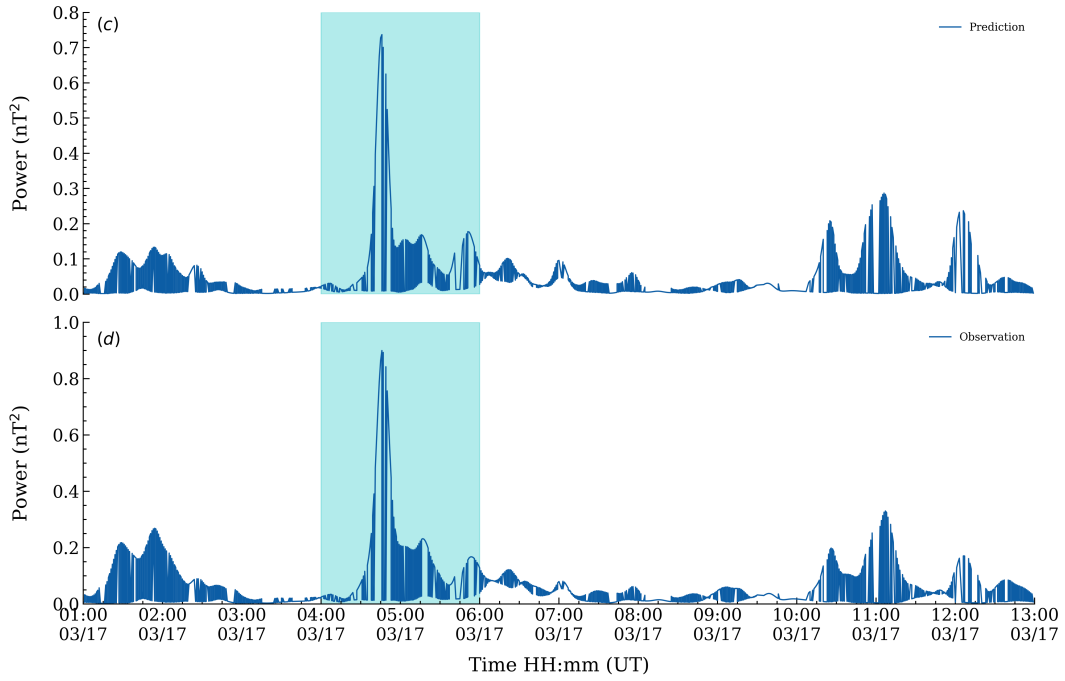


Figure 10. Wavelet scale-average wavelet power spectrum of Pc5 pulsations. Panels (c) and (d) are scaled-averaged wavelet power spectra. of prediction and observation. The highlighted area with cyan color corresponds to the study presented in Figure 9 and 8

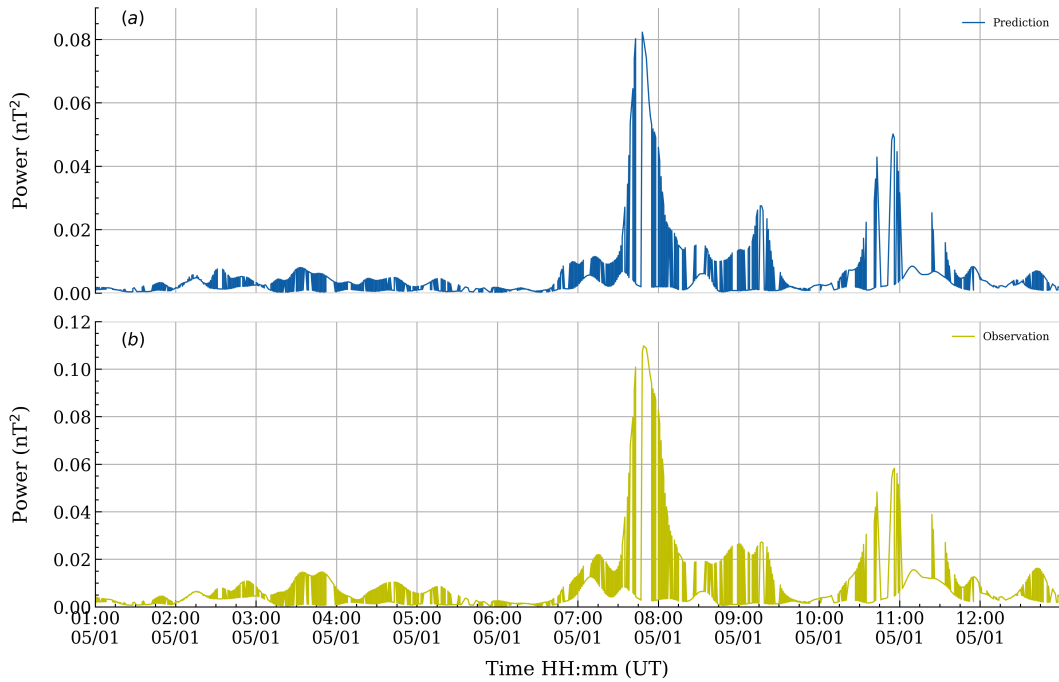


Figure 11. Wavelet scale-average wavelet power spectrum of Pc5 pulsations. Panels (a) and (b) are scaled-averaged wavelet power spectra of prediction and observation recorded on January, 1st 2015.

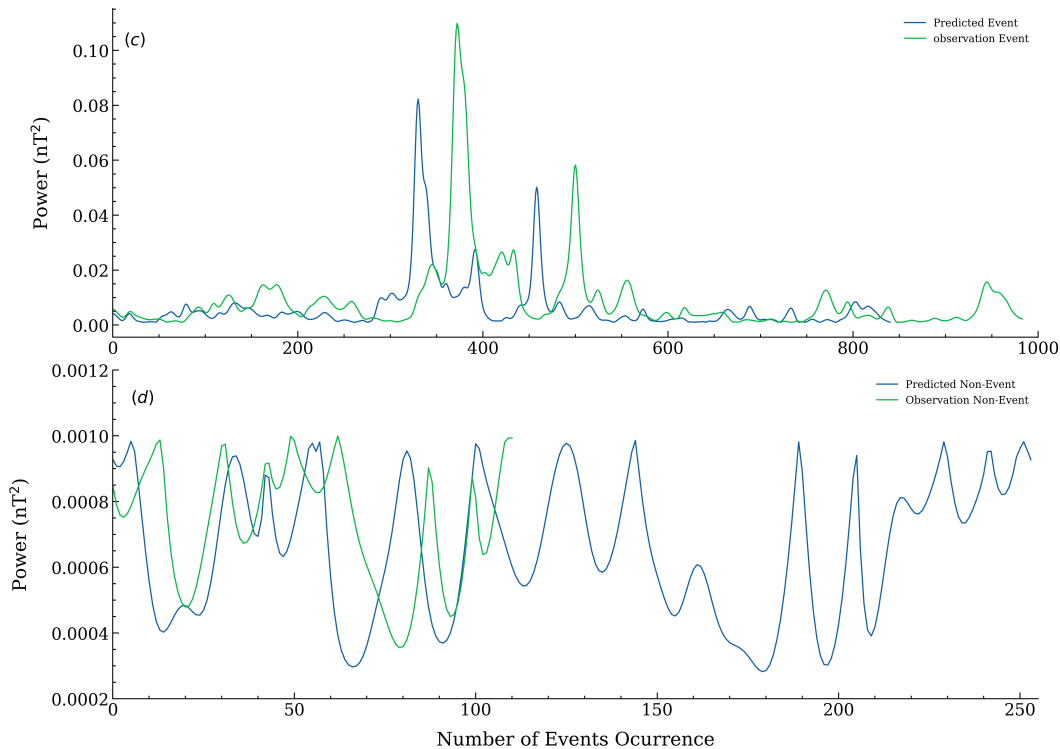


Figure 12. Pc5 event definition by wavelet power transform. Panels (c) and (d) are the predicted scaled-averaged Pc5 events and non-events respectively. These measurements are extracted from the response illustrated in Figure 11

419 compared to the number of predictions. This is accounted for by the loss function, given that
 420 we had a regression of 0.75 on average, implying that 0.25 of the original signals were
 421 lost. Nevertheless, the model was within an acceptable level and the prediction results
 422 showed similar results seen in Figure 12 (a). Table 4.2 illustrates the number of Pc5 pre-
 423 diction outcomes from the Svalbard network with NAL recording the least and HOP the
 424 highest in the year 1996. These unique results correspond to the latitudinal distributions
 425 of stations in the auroral strip and the geomagnetic activity in the region. Field line res-
 426 onance theory dictates that these ULF waves are produced by remote Alfvén oscillations
 427 in the magnetospheric Alfvénic resonator excited by MHD fluctuations from the local
 428 part of the magnetosphere. Hence, Pc5 waves peak at the latitude where the external
 429 disturbance frequency resonates with the local Alfvén frequency. Pilipenko et al. (2001)
 430 reported a possible relationship between AEJ current and Pc5 waves in the auroral lat-
 431 itude of maximum peak and intensity of the events, 73°. They argued that the Pc5 re-
 432 sponse is stimulated by the intensification of eastward AEJ with a noticeably lower mag-
 433 nitude compared to the westward AEJ. Given that the HOP station lies on the latitude
 434 of field line resonance, consequently had to record the highest corresponding to the pre-
 435 diction results.

436 The model was tested in a quiet geomagnetic condition of a weak auroral geomag-
 437 netic activity of October 23rd, 1996. This was a minor geomagnetic storm with a max-
 438 imum kp index of +7 and Ap=37. Generally, 1996 was a quiet geomagnetic year in the
 439 minimum phase of solar cycle 23. Deploying the model in other Svalbard stations ex-
 440 cept for the NAL station on the storm of October 23rd, 1996 provided astonishing re-
 441 sults. Thus, the time series prediction against actual measurements in the Svalbard net-

Table 1. Number of Pc5 pulsations predicted in the Svalbard network for the year 1996. Where Mlat is the magnetic latitude.

Station code	Mlat	Station Name	Number of Pc5 Predictions
NAL	75.25	NyAlesund	2091
LYR	75.12	Longyearbyen	3584
HOR	74.13	Hornsund	6181
HOP	73.06	HopenIsland	6949
BJN	71.09	BearIsland	6625

work was illustrated by Figure 13 and 14. Whereby, the time series observations and predictions are shown by red dotted and blue solid lines respectively.

Figure 13 (a)-(b) and Figure 13 (c)-(d) shows the model test results predicted from LYR & HOR, and HOP & BJN correspondingly. It was observed that each ground observatory observation showed a good match with the predictions illustrating the stability and integrity of the model in terms of performance. In the Four observatories, it was also noted that the HOP station' prediction response to pulsations observations recorded maximum amplitudes with more than 100 nT than other stations. The BJN & HOR recorded second and third highest, and finally, LYR recorded the lowest. The finding supports the previous studies on the auroral Pc5 pulsation characteristics (Pahud et al., 2009). This was possibly contributed by the electrodynamic convection processes resulting from ionosphere-magnetosphere current systems in the auroral strip (Rostoker & Lam, 1978). The spatial and temporal variation of Pc5 ULF waves is co-related to the location of the auroral electrojet, therefore, the maximum Pc5 wave responses are observed at the latitude of the maximum AEJ peak. Overall, the fundamental feature of auroral Pc5 pulsation such as frequency component and amplitude was predicted with higher accuracy. At last, despite complexities in the data, the model deployed in those observatories performed well with a high degree of accuracy. The spikes and inherent features of each signal in the Svalbard network were reproduced with a good consistency to the original signal. Demonstrating the power of the NARX model in nonlinear system modeling (Billings, 2013).

ULF wave power has shown dependence on L-shell and solar wind activity. There exists a strong consistency between ULF wave power and solar activity (Kessel et al., 2004), especially in the declining phase of the solar cycle having the highest correlation when the radiation belts are active (Li et al., 2011; Mann et al., 2004). Most studies have demonstrated that solar wind is the key external source and control of the geomagnetic pulsations (Mathie & Mann, 2001). Mathie and Mann (2001) pointed out that Pc5 waves decay exponentially with a declining L shell, and the decay rate increases with solar wind speed, showing a stronger dependence of ULF wave power on solar wind speed at higher L shells of the band L=3.75–6.79. The decreasing Pc5 amplitude from HOP to BJN and LYR observatories on either side of the auroral magnitude latitude (73°) as illustrated in Figure 13 and 14 are in agreement with the Rae et al. (2012) findings. Rae et al. (2012) broadened the range of L-shells in the study of Mathie and Mann (2001) to both higher and lower values and found that the ULF wave power decreases toward the higher L-shells (L=8) as well as toward lower L shells.

Ozeke et al. (2014) used statistical THEMIS and GOES observations to come up with the analytic expression for L against power for different geomagnetic activity lev-

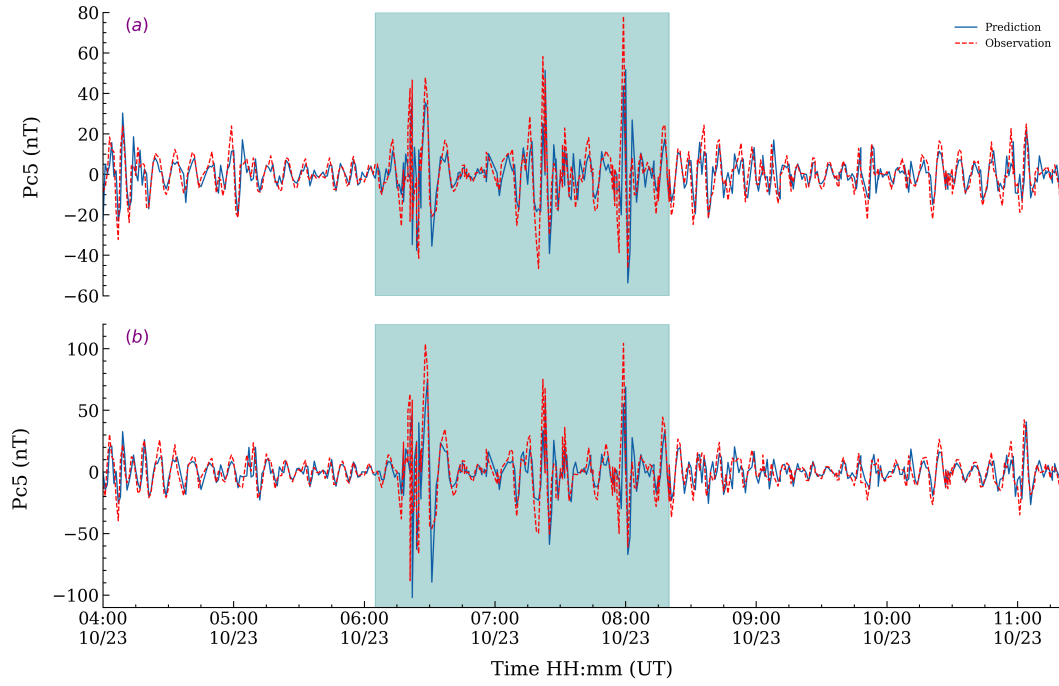


Figure 13. The prediction and Observation of Pc5 pulsations in the Svalbard network. Where panels (a), and (b) are model test results from LYR and HOR observatories in 1996.

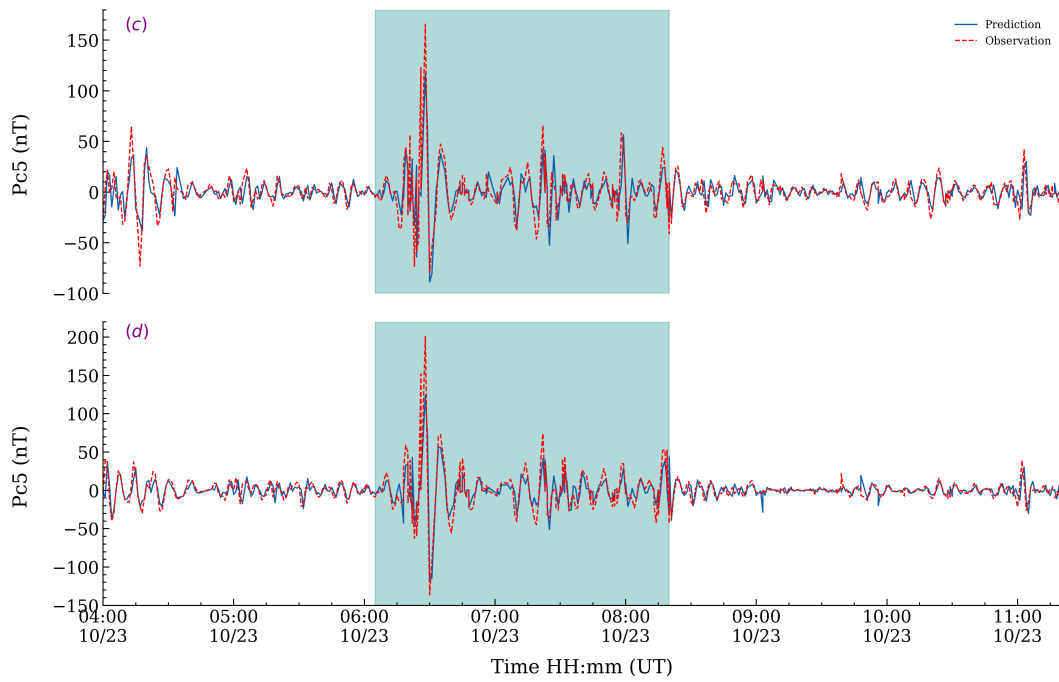


Figure 14. The prediction and Observation of Pc5 pulsations in the Svalbard network. Where panels (c), and (d) are model test results from HOP, and BJN observatories in 1996.

479 els, which can easily be used in the global radiation belt models. Recently, Dimitrakoudis
 480 et al. (2015) reported that the Kp-index is the single best parameter to investigate the

481 statistical ULF wave power driving radial diffusion. Therefore, we utilized the same con-
 482 cept in choosing Kp-index as the qualifying validation model for our model outcome. Fig-
 483 ure 15 illustrates the validation results of Pc5 prediction outcomes on testing deployment
 484 with Kp indices for two solar cycles, 23 and 24. Amongst the 8-year test datasets, 1996
 485 emerged as the most active year while 2009 was the least. There was a good correlation
 486 between Kp-index and model predictions. This implies that the ML model had good per-
 formance. It was observed that the number of occurrences of Pc5 pulsation was high in

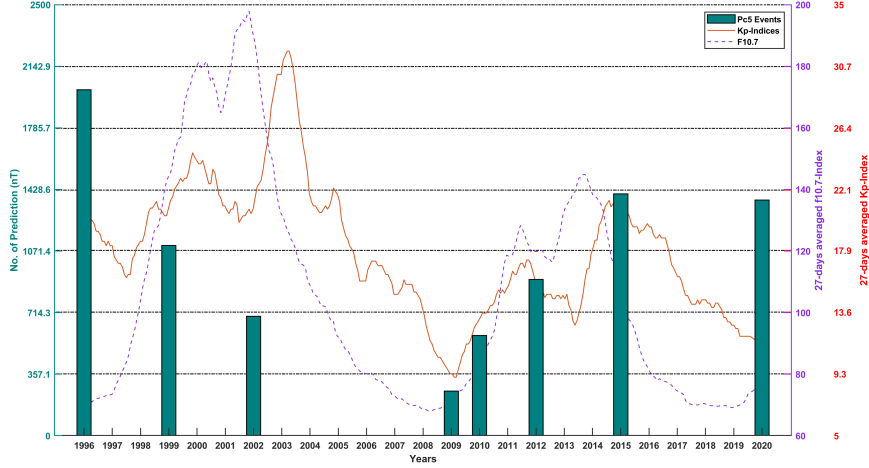


Figure 15. Kp profile index with the selected number year number of Pc5 prediction events correlation for two solar cycles. The bar graphs indicate the number of predicted Pc5 events for 8 different years of model testing while the line plot is 27days averaged Kp indices for 25 years

487 the low solar activity. The same results are reflected in the prediction of Pc5 undulations.
 488 In the ascending phase of solar cycle 23 indicated by the F10.7 index in Figure 15 shows
 489 a decreasing trend in the number of Pc5 predictions. In contrast, solar cycle 24 provided
 490 an interesting observation contrary to that of solar cycle 23. Whereby the minimum phase
 491 for solar cycle 23 recorded 264 and ascending phase 2022 Pc5 prediction events while solar
 492 cycle 24 was 1382 events in 2020. It can be noted that in both cycles there was a high
 493 geomagnetic activity in solar cycle 23 ascending phase indicated by Kp-index and low
 494 solar activity. On the other hand, the solar cycle 23 and 24 minimum phase had both
 495 minimum solar and geomagnetic activities. In relevance to machine model performance
 496 on the test set. Overall, there was good coherence between the solar activity models (F10.7),
 497 Pc5 predictions, and geomagnetic activity models (Kp).
 498

499 5 Conclusion

500 In the current study, we have developed a machine learning model based on the NARX
 501 recurrent neural network to predict time series ground Pc5 pulsations in the Svalbard
 502 network using solar wind parameters. The model was trained with 17 years of datasets
 503 and tested on 8 years of data shuffled from solar cycles 23 and 24. After the training phase,
 504 the model’s internal evaluation yielded $R=0.75$ and $MSE=11.90 \text{ nT}^2$. It was also deployed
 505 in various geomagnetic conditions, solar activities, and finally in different locations in
 506 the Svalbard network. Studies on the St.patrick storm day on March 17, 2015, demon-
 507 strated good coherence between the observation and the prediction. Consequently, the
 508 ML model showed also good performance in the four other ground observatories on the

509 minor storm of October 23rd, 1996. Therefore, these were in agreement with the other
 510 studies on this region, given that Pc5 waves recorded in one observatory are simultane-
 511 ously observed in other stations (Omondi et al., 2023). On the contrary, given that the
 512 geomagnetic Pulsations monitored in the auroral oval are the same in terms of frequency
 513 information but unique in terms of amplitude and phase. Therefore, presenting complex-
 514 ities in data. Provided the model was trained with different data from one observatory
 515 and deployed in different observatories and still able to give excellent performance de-
 516 spite uncertainties in data. This demonstrates the power of machine learning in pattern
 517 recognition from complex and large volumes of data. For example, the HOP station pro-
 518 duced a higher number of predictions compared to other stations. It also had maximum
 519 amplitude predicted Pc5 pulsations with a decaying amplitude in other stations in high
 520 and low magnetic latitudes from HOP. Given that, there were good results despite data
 521 complexity in the year 2020 and 1996. Comparing the observation in Figure 15 with Fig-
 522 ure 17 in Omondi et al. (2023) studies, there is a common trend in solar 23 and 24 pre-
 523 dictions except in 2020. Thus, in the current study, 2020 became an outlier performing
 524 average with $R=0.57$. On the contrary, more predictions were observed deviating from
 525 the trend with other observations. We conclude that the model performance was robust
 526 and fit for deployment in space weather forecasting. This was the first ground-based Pc5
 527 prediction in the auroral zone using a machine-learning technique using solar wind pa-
 528 rameters. Overall, the ML model yielded good results and useful tool in the magneto-
 529 spheric community. Therefore, to improve the model's performance, future work would
 530 focus on probabilistic prediction and forecasting.

531 Data Accessibility Statement

532 The magnetic field observations used in this study were obtained from the Sval-
 533 bard network in the International Monitor for Auroral Geomagnetic Effects (IMAGE)
 534 was accessed through (<https://space.fmi.fi/image/www/index.php>). The Solar wind
 535 parameters data utilized for prediction were retrieved from Omniweb, through ([https://](https://omniweb.gsfc.nasa.gov/)
 536 omniweb.gsfc.nasa.gov/). The Kp and F10.7 data were also obtained from the NASA
 537 data center via OmniWeb.

538 Acknowledgement

539 The corresponding Author extends his sincere gratitude to Egypt Japan Univer-
 540 sity of Science and Technology (E-JUST) and JICA cooperation for supporting the E-
 541 JUST International Alumni program which facilitated his visit and conducted the cur-
 542 rent study with the magnetospheric group of SERL-Lab. We give much appreciation to
 543 NASA for openly providing data through Omniweb (<http://cdaweb.gsfc.nasa.gov>). We
 544 give special appreciation to the institutions maintaining the IMAGE Magnetometer Ar-
 545 ray and providing data for science: Tromsø Geophysical Observatory of UiT the Arc-
 546 tic University of Norway(Norway), Finnish Meteorological Institute (Finland), GFZ Ger-
 547 man Research Centre for Geosciences (Germany), Institute of Geophysics Polish Academy
 548 of Sciences (Poland), Swedish Institute of Space Physics (Sweden), Geological Survey
 549 of Sweden(Sweden), Polar Geophysical Institute (Russia) and Sodankyla Geophysical
 550 Observatory of the University of Oulu (Finland).

551 References

- 552 Ayala Solares, J. R., Wei, H.-L., Boynton, R. J., Walker, S. N., & Billings, S. A.
 553 (2016). Modeling and prediction of global magnetic disturbance in near-earth
 554 space: A case study for kp index using narx models. *Space Weather*, 14(10),
 555 899–916.
 556 Baddeley, L., Yeoman, T., McWilliams, K., & Wright, D. (2007). Global pc5
 557 wave activity observed using superdarn radars and ground magnetometers

- 558 during an extended period of northward imf. *Planetary and Space Science*,
 559 55(6), 792-808. (Ultra-Low Frequency Waves in the Magnetosphere) doi:
 560 <https://doi.org/10.1016/j.pss.2006.01.009>
- 561 Balikhin, M. A., Boynton, R. J., Walker, S. N., Borovsky, J. E., Billings, S. A., &
 562 Wei, H. L. (2011). Using the narmax approach to model the evolution of en-
 563 ergetic electrons fluxes at geostationary orbit. *Geophysical Research Letters*,
 564 38(18). doi: <https://doi.org/10.1029/2011GL048980>
- 565 Bhaskar, A., & Vichare, G. (2019). Forecasting of symh and asyh indices for geo-
 566 magnetic storms of solar cycle 24 including st. patrick's day, 2015 storm using
 567 narx neural network. *Journal of Space Weather and Space Climate*, 9, A12.
- 568 Billings, S. A. (2013). *Nonlinear system identification: Narmax methods in the time,*
 569 *frequency, and spatio-temporal domains.* John Wiley & Sons. doi: [https://doi](https://doi.org/10.1002/9781118535561)
 570 [.org/10.1002/9781118535561](https://doi.org/10.1002/9781118535561)
- 571 Boynton, R. J., Balikhin, M. A., Billings, S. A., Wei, H. L., & Ganushkina, N.
 572 (2011). Using the narmax ols-err algorithm to obtain the most influential
 573 coupling functions that affect the evolution of the magnetosphere. *Journal of*
 574 *Geophysical Research: Space Physics*, 116(A5). doi: [https://doi.org/10.1029/](https://doi.org/10.1029/2010JA015505)
 575 [2010JA015505](https://doi.org/10.1029/2010JA015505)
- 576 Cai, L., Ma, S., Cai, H., Zhou, Y., & Liu, R. (2009). Prediction of sym-h index by
 577 narx neural network from imf and solar wind data. *Science in China Series E:*
 578 *Technological Sciences*, 52, 2877–2885.
- 579 Chandorkar, M., Camporeale, E., & Wing, S. (2017). Probabilistic forecasting of the
 580 disturbance storm time index: An autoregressive gaussian process approach.
 581 *Space Weather*, 15(8), 1004–1019.
- 582 Chen, L., & Hasegawa, A. (1974). A theory of long-period magnetic pulsations:
 583 1. steady state excitation of field line resonance. *Journal of Geophysical*
 584 *Research (1896-1977)*, 79(7), 1024-1032. doi: [https://doi.org/10.1029/](https://doi.org/10.1029/JA079i007p01024)
 585 [JA079i007p01024](https://doi.org/10.1029/JA079i007p01024)
- 586 Dimitrakoudis, S., Mann, I. R., Balasis, G., Papadimitriou, C., Anastasiadis, A.,
 587 & Daglis, I. A. (2015). Accurately specifying storm-time ulf wave radial
 588 diffusion in the radiation belts. *Geophysical Research Letters*, 42(14), 5711-
 589 5718. Retrieved from [https://agupubs.onlinelibrary.wiley.com/doi/abs/](https://agupubs.onlinelibrary.wiley.com/doi/abs/10.1002/2015GL064707)
 590 [10.1002/2015GL064707](https://doi.org/10.1002/2015GL064707) doi: <https://doi.org/10.1002/2015GL064707>
- 591 Dungey, J. W. (1961). Interplanetary magnetic field and the auroral zones. *Physical*
 592 *Review Letters*, 6(2), 47.
- 593 Eastwood, J., Nakamura, R., Turc, L., Mejnertsen, L., & Hesse, M. (2017). The sci-
 594 entific foundations of forecasting magnetospheric space weather. *Space Science*
 595 *Reviews*, 212, 1221–1252.
- 596 Gholipour, A., Lucas, C., & Araabi, B. N. (2004). Black box modeling of magneto-
 597 spheric dynamics to forecast geomagnetic activity. *Space Weather*, 2(7).
- 598 Gu, Y., Wei, H.-L., Boynton, R. J., Walker, S. N., & Balikhin, M. A. (2019). Sys-
 599 tem identification and data-driven forecasting of ae index and prediction un-
 600 certainty analysis using a new cloud-narx model. *Journal of Geophysical*
 601 *Research: Space Physics*, 124(1), 248-263. doi: [https://doi.org/10.1029/](https://doi.org/10.1029/2018JA025957)
 602 [2018JA025957](https://doi.org/10.1029/2018JA025957)
- 603 Harrold, B. G., & Samson, J. C. (1992). Standing ulf modes of the magnetosphere:
 604 A theory. *Geophysical Research Letters*, 19(18), 1811-1814. doi: [https://doi](https://doi.org/10.1029/92GL01802)
 605 [.org/10.1029/92GL01802](https://doi.org/10.1029/92GL01802)
- 606 Kamide, Y., Baumjohann, W., Daglis, I. A., Gonzalez, W. D., Grande, M., Jose-
 607 lyn, J. A., ... Vasyliunas, V. M. (1998). Current understanding of magnetic
 608 storms: Storm-substorm relationships. *Journal of Geophysical Research: Space*
 609 *Physics*, 103(A8), 17705-17728. doi: <https://doi.org/10.1029/98JA01426>
- 610 Kessel, R., Mann, I., Fung, S., Milling, D., & O'Connell, N. (2004). Correlation
 611 of pc5 wave power inside and outside the magnetosphere during high speed
 612 streams. In *Annales geophysicae* (Vol. 22, pp. 629–641).

- 613 Kivelson, M. G., Etcheto, J., & Trotignon, J. G. (1984). Global compressional os-
 614 cillations of the terrestrial magnetosphere: The evidence and a model. *Journal*
 615 *of Geophysical Research: Space Physics*, 89(A11), 9851-9856. doi: [https://doi](https://doi.org/10.1029/JA089iA11p09851)
 616 [.org/10.1029/JA089iA11p09851](https://doi.org/10.1029/JA089iA11p09851)
- 617 Kleimenova, N., Kozyreva, O., Vlasov, A., Uspensky, M., & Kauristie, K. (2010).
 618 Afternoon pc5 geomagnetic pulsations on the earth's surface and in the iono-
 619 sphere (stare radars). *Geomagnetism and Aeronomy*, 50, 329-338. doi:
 620 <https://doi.org/10.1134/S0016793210030072>
- 621 Lee, E. A., Mann, I. R., Loto'aniu, T. M., & Dent, Z. C. (2007). Global pc5 pul-
 622 sations observed at unusually low l during the great magnetic storm of 24
 623 march 1991. *Journal of Geophysical Research: Space Physics*, 112(A5). doi:
 624 <https://doi.org/10.1029/2006JA011872>
- 625 Li, X., Temerin, M., Baker, D. N., & Reeves, G. D. (2011). Behavior of mev elec-
 626 trons at geosynchronous orbit during last two solar cycles. *Journal of Geo-*
 627 *physical Research: Space Physics*, 116(A11). doi: [https://doi.org/10.1029/](https://doi.org/10.1029/2011JA016934)
 628 [2011JA016934](https://doi.org/10.1029/2011JA016934)
- 629 Mann, I., O'Brien, T., & Milling, D. (2004). Correlations between ulf wave power,
 630 solar wind speed, and relativistic electron flux in the magnetosphere: solar
 631 cycle dependence. *Journal of Atmospheric and Solar-Terrestrial Physics*,
 632 66(2), 187-198. (Space Weather in the Declining Phase of the Solar Cycle) doi:
 633 <https://doi.org/10.1016/j.jastp.2003.10.002>
- 634 Mathie, R., & Mann, I. (2001). On the solar wind control of pc5 ulf pulsation
 635 power at mid-latitudes: Implications for mev electron acceleration in the outer
 636 radiation belt. *Journal of Geophysical Research: Space Physics*, 106(A12),
 637 29783-29796.
- 638 McCulloch, W. S., & Pitts, W. (1943). A logical calculus of the ideas immanent in
 639 nervous activity. *The bulletin of mathematical biophysics*, 5, 115-133. doi:
 640 <https://doi.org/10.1007/BF02478259>
- 641 Omondi, S., Yoshikawa, A., Zahra, W. K., Fathy, I., & Mahrous, A. (2023). Auto-
 642 matic detection of auroral pc5 geomagnetic pulsation using machine learning
 643 approach guided with discrete wavelet transform. *Advances in Space Research*,
 644 72(3), 866-883. doi: <https://doi.org/10.1016/j.asr.2022.06.063>.
- 645 Ozeke, L. G., Mann, I. R., Murphy, K. R., Jonathan Rae, I., & Milling, D. K.
 646 (2014). Analytic expressions for ulf wave radiation belt radial diffusion co-
 647 efficients. *Journal of Geophysical Research: Space Physics*, 119(3), 1587-1605.
 648 doi: <https://doi.org/10.1002/2013JA019204>
- 649 Pahud, D., Rae, I., Mann, I., Murphy, K., & Amalraj, V. (2009). Ground-based pc5
 650 ulf wave power: Solar wind speed and mlt dependence. *Journal of Atmospheric*
 651 *and Solar-Terrestrial Physics*, 71(10-11), 1082-1092.
- 652 Pilipenko, V., Watermann, J., Popov, V., & Papitashvili, V. (2001). Relationship
 653 between auroral electrojet and pc5 ulf waves. *Journal of Atmospheric and*
 654 *Solar-Terrestrial Physics*, 63(14), 1545-1557. doi: [https://doi.org/10.1016/](https://doi.org/10.1016/S1364-6826(01)00031-1)
 655 [S1364-6826\(01\)00031-1](https://doi.org/10.1016/S1364-6826(01)00031-1)
- 656 Poulton, M. M. (2002). Neural networks as an intelligence amplification tool: A
 657 review of applications. *Geophysics*, 67(3), 979-993. doi: [https://doi.org/10](https://doi.org/10.1190/1.1484539)
 658 [.1190/1.1484539](https://doi.org/10.1190/1.1484539).
- 659 Rae, I. J., Mann, I. R., Murphy, K. R., Ozeke, L. G., Milling, D. K., Chan, A. A.,
 660 ... Honary, F. (2012). Ground-based magnetometer determination of
 661 in situ pc4-5 ulf electric field wave spectra as a function of solar wind
 662 speed. *Journal of Geophysical Research: Space Physics*, 117(A4). doi:
 663 <https://doi.org/10.1029/2011JA017335>
- 664 Rostoker, G., & Lam, H.-L. (1978). A generation mechanism for pc 5 micropulsa-
 665 tions in the morning sector. *Planetary and Space Science*, 26(5), 493-505.
- 666 Samson, J., Cogger, L., & Pao, Q. (1996). Observations of field line resonances,
 667 auroral arcs, and auroral vortex structures. *Journal of Geophysical Research:*

- 668 *Space Physics*, 101(A8), 17373–17383.
- 669 Samson, J., Jacobs, J. A., & Rostoker, G. (1971). Latitude-dependent character-
 670 istics of long-period geomagnetic micropulsations. *Journal of Geophysical Re-*
 671 *search (1896-1977)*, 76(16), 3675–3683.
- 672 Southwood, D. (1974). Some features of field line resonances in the magne-
 673 tosphere. *Planetary and Space Science*, 22(3), 483–491. Retrieved from
 674 <https://www.sciencedirect.com/science/article/pii/0032063374900786>
 675 doi: [https://doi.org/10.1016/0032-0633\(74\)90078-6](https://doi.org/10.1016/0032-0633(74)90078-6)
- 676 Uwamahoro, J., & Habarulema, J. B. (2014). Empirical modeling of the storm time
 677 geomagnetic indices: a comparison between the local k and global kp indices.
 678 *Earth, Planets and Space*, 66, 1–8.
- 679 Waters, C., Samson, J., & Donovan, E. (1995). The temporal variation of the fre-
 680 quency of high latitude field line resonances. *Journal of Geophysical Research:*
 681 *Space Physics*, 100(A5), 7987–7996.
- 682 Wei, H. L., Billings, S. A., & Balikhin, M. (2004). Prediction of the dst index us-
 683 ing multiresolution wavelet models. *Journal of Geophysical Research: Space*
 684 *Physics*, 109(A7). doi: <https://doi.org/10.1029/2003JA010332>
- 685 Weigel, R., Horton, W., Tajima, T., & Detman, T. (1999). Forecasting auroral
 686 electrojet activity from solar wind input with neural networks. *Geophysical re-*
 687 *search letters*, 26(10), 1353–1356.
- 688 Willisroft, L.-A., & Poole, A. W. (1996). Neural networks, fof2, sunspot number
 689 and magnetic activity. *Geophysical research letters*, 23(24), 3659–3662.
- 690 Wintoft, P., Wik, M., Matzka, J., & Shprits, Y. (2017). Forecasting kp from solar
 691 wind data: input parameter study using 3-hour averages and 3-hour range
 692 values. *Journal of Space Weather and Space Climate*, 7, A29.
- 693 Wu, J.-G., & Lundstedt, H. (1996). Prediction of geomagnetic storms from solar
 694 wind data using elman recurrent neural networks. *Geophysical research letters*,
 695 23(4), 319–322.
- 696 Wu, J.-G., Lundstedt, H., Wintoft, P., & Detman, T. (1998). Neural network models
 697 predicting the magnetospheric response to the 1997 january halo-cme event.
 698 *Geophysical research letters*, 25(15), 3031–3034.
- 699 Ziesolleck, C. W. S., & McDiarmid, D. R. (1994). Auroral latitude pc 5 field line
 700 resonances: Quantized frequencies, spatial characteristics, and diurnal varia-
 701 tion. *Journal of Geophysical Research: Space Physics*, 99(A4), 5817–5830. doi:
 702 <https://doi.org/10.1029/93JA02903>